Passive Control of Shock-Wave/ Turbulent Boundary-Layer Interaction

Effects of Spanwise Heterogeneous Roughness

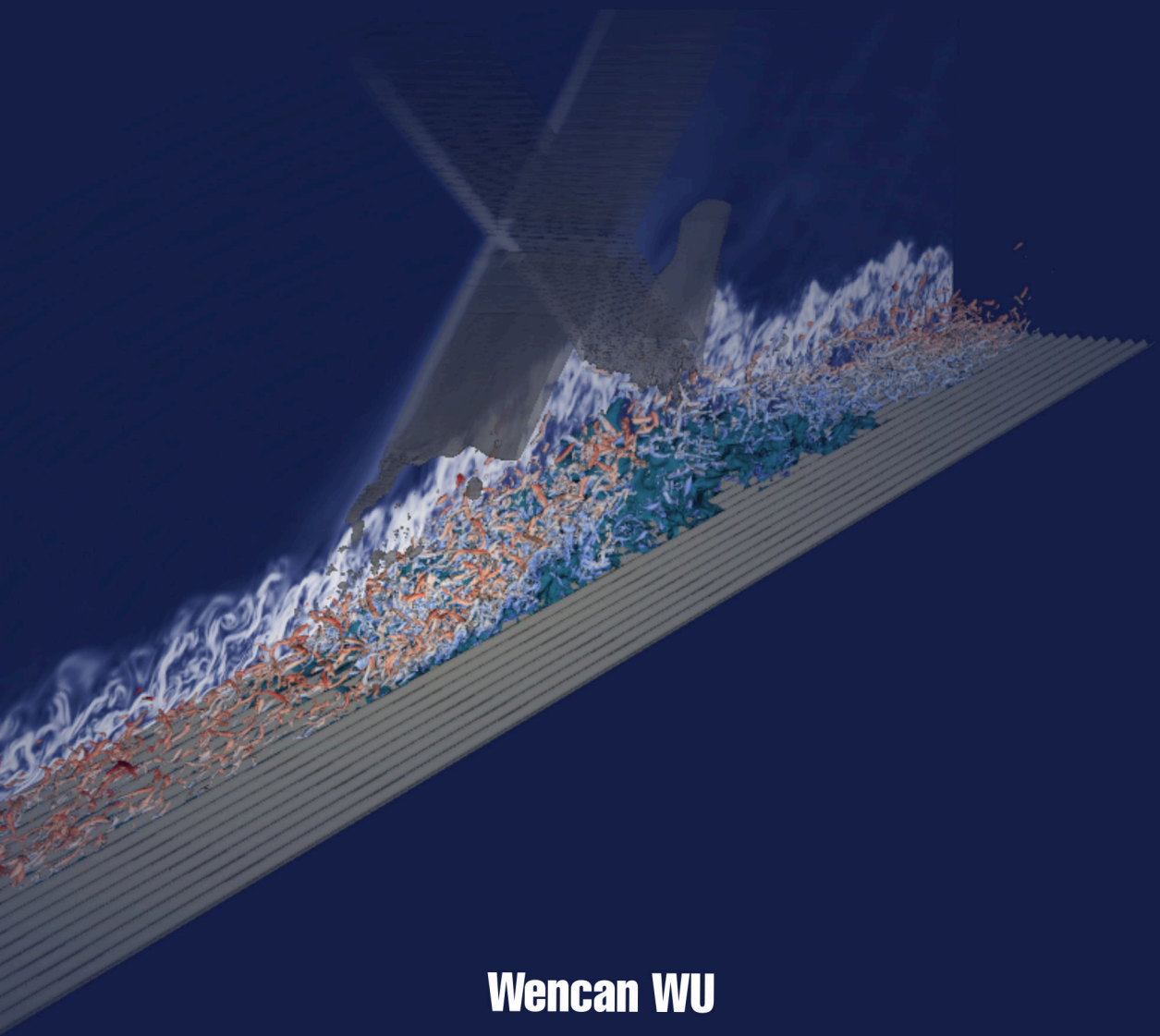

Wencan WU

吴文灿

PASSIVE CONTROL OF SHOCK-WAVE/TURBULENT BOUNDARY-LAYER INTERACTION

EFFECTS OF SPANWISE HETEROGENEOUS ROUGHNESS

PASSIVE CONTROL OF SHOCK-WAVE/TURBULENT BOUNDARY-LAYER INTERACTION

EFFECTS OF SPANWISE HETEROGENEOUS ROUGHNESS

Dissertation

For the purpose of obtaining the degree of doctor
at Delft University of Technology,
by the authority of the Rector Magnificus Prof.dr.ir. H.Bijl,
Chair of the Board for Doctorates,
to be defended publicly on
Thursday, 25 June 2026, at 17:30

by

Wencan WU

This dissertation has been approved by the (co)promotors.

Composition of the doctoral committee:

Rector Magnificus,	Chairperson
Prof.Dr.-Ing.habil S. Hickel,	Delft University of Technology, promotor
Dr. D. Modesti,	Delft University of Technology/ Gran Sasso Science Institute, Italy, copromotor
Independent members:	
Prof.Dr.-Ing G. Eitelberg,	Delft University of Technology
Prof.dr. N. Sandham,	University of Southampton
Prof.dr. F. Picano,	University of Padova
Prof.dr. J. Fang,	University of Chinese Academy of Sciences
Dr.ir. F.F.J. Schrijer,	Delft University of Technology
Prof.Dr. R. Pecnik,	Delft University of Technology, *reserve member*

This research was conducted within the Flow Physics and Technology Department at Delft University of Technology, and was sponsored by the Chinese Scholarship Council (CSC No. 202106020054).

Keywords: STBLI, Passive control, Roughness, Large eddy simulation

Printed by: Proefschriftspecialist

Front & Back: Design by the author.

ISBN 978-94-6518-354-1

An electronic version of this dissertation is available at
http://repository.tudelft.nl/.

To my family and friends.

CONTENTS

NOMENCLATURE

Acronyms

ALDM	Adaptive Local Deconvolution Method
C-D	Convergent-Divergent
CFD	Computational Fluid Dynamics
CL	Convergent Line
DF	Digital Filter
DL	Divergent Line
DMD	Dynamic Mode Decomposition
DNS	Direct Numerical Simulation
FFT	Fast Fourier Transform
IB	Immersed Boundary
ILES	Implicit Large-Eddy Simulation
LES	Large-Eddy Simulation
MDE	Modified Differential Equation
MVG	Micro-Vortex Generator
NACA	National Advisory Committee for Aeronautics
PIV	Particle Image Velocimetry
PSD	Power Spectral Density
SGS	Subgrid Scale
SPDMD	Sparsity-Promoting Dynamic Decomposition Method
STBLI	Shock-wave/Turbulent Boundary-Layer Interaction
SVD	Singular Value Decomposition
TBL	Turbulent Boundary-Layer
TKE	Turbulent Kinetic Energy

VG Vortex Generator

WENO Weighted Essentially Non-Oscillatory

Greek Symbols

α fluid volume fraction

β smoothness or growth rate

χ reverse-flow probability

δ_v viscous length scale

δ_{ij} Kronecker delta function

Γ interface element

γ specific heat ratio or regularization parameters or yaw angle of riblet

Λ spanwise width of riblet

λ ridge width

μ dynamic viscosity or eigen value

Ω fluid/solid domain

ω weight or angular frequency

ϕ generic variable

ψ mode amplitude

ρ density

τ stress or time delay

θ angle

ϑ flow angle

b base width of riblet

Latin Symbols

$\boldsymbol{A}$ linear mapping

$\boldsymbol{C}$ convective flux

$\boldsymbol{D}$ diffusive flux

$\boldsymbol{n}$ normal vector

$\boldsymbol{P}$ pressure flux

$\boldsymbol{S}$	non-conservative source term
$\boldsymbol{U}$	state vector
$\boldsymbol{x}$	snapshot data
δ_0	boundary layer thickness at inlet
A	area
b_k	discrete filter coefficient
c	grid-dependent coefficient
C_f	skin-friction coefficient
c_p	specific heat
D	ridge distance
E	total energy
e	inner energy
f	frequency
g	reconstruction value
H	height of roughness or shape factor
h	grid spacing or distance from wall or riblet height
H_{md}	meltdown height of ridge
I	intensity of secondary flow
I_L	prescribed integral length scale
k	thermal conductivity
L_x	domain size in streamwise direction
L_y	domain size in wall-normal direction
L_z	domain size in spanwise direction
P	total power
p	pressure
Pr	Prandtl number
q	heat flux
R	correlation value or specific gas constant

Re	Reynolds number
s	riblet spacing
St	Strouhal number
T	temperature
t	time or top width of riblet
u	streamwise velocity or velocity component
V	volume
v	wall-normal velocity
w	spanwise velocity
x	streamwise coordinate
y	wall-normal coordinate
y_s	shifted wall-normal coordinate
z	spanwise coordinate

Other Symbols

$*$	convolution
$\boldsymbol{\chi}$	interface exchange term
$\cdot'$	fluctuation
$\breve{\cdot}$	approximation solution
$\langle\cdot\rangle$	time-averaged value
$\langle\cdot\rangle_z$	spanwise-averaged
$\mathcal{F}$	total flux
$\mathcal{G}$	general error or residual
$\mathcal{P}$	power spectral density
$\mathcal{S}_i$	Gaussian random numbers
$\mathfrak{R}$	real part
∇	Nabla symbol
$\bar{\cdot}$	spatially filtered quantity
$\sum$	summation

Subscripts/Superscripts

0	stagnation parameter or value at inlet
∞	free stream parameters
v	related to viscosity
τ	based on wall friction velocity
avg	averaged value
BI	related to boundary intercept
ele	property of interface element
GP	related to ghost point
ht	related to heat transfer
i	streamwise index
imp	value at nominal impingement point
IP	related to image intercept
j	wall-normal index
k	order of accuracy or spanwise index
l	index within stencil
m	number of snapshots
max	maximum value
p	related to pressure
r	stencil shift
sep	related to separation bubble
sw	related to shock wave
vD	van-Driest transformed
w	value at wall
+	based on inner scaling

SUMMARY

Shock-wave/turbulent boundary-layer interaction (STBLI) is a ubiquitous phenomenon in high-speed aerodynamic applications, such as rocket nozzles, engine inlets, airplane wings and control surfaces. The interaction between a shock wave and a turbulent boundary layer often leads to flow separation, severe wall-pressure fluctuations, and unsteady thermal loads, which can significantly degrade aerodynamic performance and structural integrity. Mitigating these adverse effects remains a long-standing challenge in compressible flow research. While numerous active and passive control strategies have been proposed, many of them suffer from practical limitations, including high energy consumption, geometric complexity, or strong sensitivity to installation location.

This dissertation investigates the potential of spanwise-heterogeneous roughness as a purely passive control strategy for STBLI, with a particular focus on convergent–divergent riblets and streamwise-homogeneous ridge-type roughness. Using wall-resolved large-eddy simulations combined with an immersed boundary method, a Mach 2.0 impinging shock-wave/turbulent boundary-layer interaction is systematically studied over smooth and rough walls. The numerical framework enables a detailed analysis of both the mean flow and unsteady characteristics of the interaction, as well as the underlying physical mechanisms governing roughness-induced flow modification.

The first part of the study examines the control effects of convergent-divergent riblet patches. It is shown that the riblets induce organized secondary flows in the form of counter-rotating streamwise vortices, which significantly modify the incoming turbulent boundary layer prior to the interaction. These secondary flows lead to a spanwise redistribution of momentum, resulting in a corrugated separation topology and an attenuation of wall-pressure fluctuations near the separation shock foot, while simultaneously causing an upstream shift of the interaction onset and an enlargement of the interaction and separation regions. Owing to the localized nature of the induced vortices, whose influence is expected to decay in the streamwise direction, the overall control authority remains inherently limited, while an additional pressure-drag penalty is inevitably introduced.

Motivated by these limitations, the second part of the dissertation focuses on streamwise-homogeneous ridge-type roughness, which offers greater robustness and reduced sensitivity to installation location. The results demonstrate that ridge-type roughness induces Prandtl's secondary flows of the second kind, leading to systematic modifications of the upstream turbulent boundary layer. When the ridge spacing is comparable to the boundary-layer thickness, strong downwash motions locally energize the turbulent boundary layer, thereby suppressing flow separation while simultaneously increasing wall-pressure fluctuations. For smaller ridge spacings, a pronounced subsonic region forms within the incoming boundary layer, resulting in a less-full velocity profile. This modification weakens the streamwise wall-pressure gradient and smears the separation shock foot, leading to a substantial attenuation of wall-pressure fluctuations over a broad frequency range, albeit at the cost of an enlarged separation region. Parametric

studies further reveal that increasing the ridge height amplifies the attenuation of wall-pressure fluctuations by enhancing the roughness-induced modification of the upstream boundary layer.

Finally, the influence of Reynolds number on the control performance is examined. The results show that wall-pressure fluctuations near the separation shock foot comprise a low-frequency component associated with shock motion and a high-frequency component associated with shear-layer turbulence, with their relative contributions strongly dependent on the Reynolds number. At low Reynolds numbers, the high-frequency component dominates, whereas at higher Reynolds numbers the low-frequency component becomes prevalent. In this high-Reynolds-number regime, where low-frequency shock unsteadiness governs the interaction dynamics, ridge-type roughness remains effective and yields an even stronger attenuation, with peak wall-pressure fluctuations reduced by up to 27%. Spectral analysis and cross-correlation studies support a downstream-influence mechanism for the low-frequency unsteadiness, while dynamic mode decomposition reveals the presence of large-scale Görtler-like vortices downstream of the interaction region.

Overall, this dissertation demonstrates that spanwise-heterogeneous roughness, if properly designed, can serve as a robust and practical passive control strategy for mitigating STBLI unsteadiness in high-speed flows, albeit at the cost of a moderate increase in skin-friction drag. The findings provide new physical insights into the interplay between roughness-induced secondary flows, Reynolds number effects, and low-frequency STBLI dynamics, and offer guidance for the design of roughness-based flow control concepts in future high-speed aerodynamic applications.

SAMENVATTING

Schokgolf-turbulente grenslaaginteractie (STBLI) is een wijdverbreid fenomeen in hogesnelheidsaerodynamische toepassingen, zoals raketnozzles, motorinlaten, vliegtuigvleugels en stuurvlakken. De interactie tussen een schokgolf en een turbulente grenslaag leidt vaak tot stromingsafscheiding, sterke wanddrukfluctuaties en onstationaire thermische belastingen, die de aerodynamische prestaties en structurele integriteit aanzienlijk kunnen aantasten. Het verminderen van deze nadelige effecten vormt al lange tijd een uitdaging binnen het onderzoek naar samendrukbare stromingen. Hoewel talrijke actieve en passieve regelstrategieën zijn voorgesteld, kampen veel daarvan met praktische beperkingen, zoals een hoog energieverbruik, geometrische complexiteit of een sterke gevoeligheid voor de installatielocatie.

In dit proefschrift wordt het potentieel van spanwijdte-heterogene ruwheid onderzocht als een zuiver passieve regelstrategie voor STBLI, met bijzondere aandacht voor convergent–divergent riblets en streamwise-homogene ridge-type ruwheid. Met behulp van wand-opgeloste large-eddy-simulaties, gecombineerd met een immersed-boundary-methode, wordt een Mach 2.0 impingende schokgolf–turbulente grenslaaginteractie systematisch bestudeerd boven zowel gladde als ruwe wanden. Dit numerieke raamwerk maakt een gedetailleerde analyse mogelijk van zowel de gemiddelde stroming als de onstationaire interactiekenmerken, evenals van de onderliggende fysische mechanismen die door ruwheid geïnduceerde stromingsmodificaties bepalen.

Het eerste deel van de studie richt zich op de regelwerking van convergent-divergent-ribletpatches. Aangetoond wordt dat deze riblets georganiseerde secundaire stromingen opwekken in de vorm van tegenroterende wervels in stroomrichting, die de inkomende turbulente grenslaag aanzienlijk modificeren vóór de interactie. Deze secundaire stromingen leiden tot een spanwijdteherverdeling van impuls, wat resulteert in een gegolfde afscheidingstopologie en een afname van de wanddrukfluctuaties nabij de voet van de afscheidingsschok. Tegelijkertijd gaat deze modificatie van de grenslaag gepaard met een stroomopwaartse verschuiving van het begin van de interactie en een vergroting van zowel het interactie- als het afscheidingsgebied. Vanwege het lokale karakter van de geïnduceerde wervels, waarvan de invloed naar verwachting snel in stroomrichting afneemt, blijft de algehele regelcapaciteit inherent beperkt, terwijl onvermijdelijk een extra drukweerstandsbijdrage wordt geïntroduceerd.

Gemotiveerd door deze beperkingen richt het tweede deel van het proefschrift zich op stroomrichting-homogene ruwheid van het ridge-type, die een grotere robuustheid en een verminderde gevoeligheid voor de installatielocatie biedt. De resultaten tonen aan dat ridge-type ruwheid Prandtls secundaire stromingen van de tweede soort induceert, wat leidt tot systematische modificaties van de inkomende turbulente grenslaag. Wanneer de afstand tussen de ribbels vergelijkbaar is met de dikte van de grenslaag, zorgen sterke neerwaartse stromingsbewegingen lokaal voor energisering van de turbulente grenslaag, waardoor stromingsafscheiding wordt onderdrukt, maar tegelijkertijd de wanddrukfluc-

tuaties toenemen. Bij kleinere ribbelafstanden vormt zich daarentegen een uitgesproken subsonisch gebied binnen de inkomende grenslaag, wat resulteert in een minder volle snelheidsprofielvorm. Deze modificatie verzwakt de stromingsrichting-gebonden wanddrukgradiënt en vervaagt de voet van de afscheidingsschok, wat leidt tot een aanzienlijke afname van wanddrukfluctuaties over een breed frequentiebereik, zij het ten koste van een vergroot afscheidingsgebied. Parametrische studies tonen bovendien aan dat een grotere ribbelhoogte deze dempingswerking van de wanddrukfluctuaties versterkt door de door ruwheid geïnduceerde modificatie van de inkomende grenslaag te intensiveren.

Ten slotte wordt de invloed van het Reynoldsgetal op de regelprestatie onderzocht. De resultaten laten zien dat wanddrukfluctuaties nabij de voet van de afscheidingsschok bestaan uit een laagfrequente component die samenhangt met schokbewegingen en een hoogfrequente component die wordt geassocieerd met turbulentie in de schuiflaag, waarbij hun relatieve bijdragen sterk afhankelijk zijn van het Reynoldsgetal. Bij lage Reynoldsgetallen domineert de hoogfrequente component, terwijl bij hogere Reynoldsgetallen de laagfrequente component overheersend wordt. In dit hoge-Reynoldsgetalregime, waarin laagfrequente schokonstabiliteit de interactiedynamica bepaalt, blijft ridge-type ruwheid effectief en resulteert zij in een nog sterkere demping, met een reductie van de maximale wanddrukfluctuaties tot 27%. Spectrale analyses en kruis-correlatiestudies ondersteunen een stroomafwaarts-invloedmechanisme voor de laagfrequente onstandvastigheid, terwijl dynamische-modedecompositie de aanwezigheid onthult van grootschalige, Görtler-achtige wervels stroomafwaarts van het interactiegebied.

Samenvattend toont dit proefschrift aan dat spanwijdte-heterogene ruwheid, mits zorgvuldig ontworpen, kan dienen als een robuuste en praktisch toepasbare passieve regelstrategie om STBLI-onstandvastigheid in hogesnelheidsstromingen te verminderen, zij het tegen de prijs van een matige toename van de wrijvingsweerstand. De bevindingen verschaffen nieuwe fysische inzichten in de wisselwerking tussen door ruwheid geïnduceerde secundaire stromingen, Reynoldsgetaleffecten en laagfrequente STBLI-dynamica, en bieden richtlijnen voor het ontwerp van ruwheidsgebaseerde stromingsregelconcepten in toekomstige hogesnelheidsaerodynamische toepassingen.

1

INTRODUCTION

欲穷千里目，更上一层楼。
You will enjoy a grander sight, if you climb to a greater height.
王之涣/ *Wang Zhihuan*

1

1.1. HISTORICAL BACKGROUND

On October 5 (1947), I made my sixth powered flight and experienced shock-wave buffeting for the first time when I reached 0.86 Mach. It felt like I was driving on bad shock absorbers over uneven paving stones. The right wing suddenly got heavy and began to drop, and when I tried to correct it, my controls were sluggish.

These reflections were later captured in the autobiography of Yeager, the first pilot to successfully break the sound barrier (Yeager and Janos, 1985), see Figure 1.1(a). The test aircraft he piloted was the Bell X-1, as shown in Figure 1.1(b), a rocket engine-powered aircraft with a distinctive bullet-shaped fuselage and unswept thin wings tailored for the challenges of high-speed flight. Although the X-1 itself did not employ swept wings, earlier aircraft such as the Messerschmitt Me 163 and Me 262 had already incorporated swept-wing configurations that were better suited to transonic flight.

The problems Yeager described in that test flight — buffeting, wing rock, and wing drop — were all fundamentally linked to separation induced by shock–wave/turbulent boundary-layer interactions (STBLI). As the aircraft approaches the speed of sound, portions of the flow over the airfoil become locally supersonic and are terminated by a normal shock wave, as illustrated in Figure 1.2. The strong adverse pressure gradient at the shock foot causes the incoming boundary layer to separate from the airfoil surface. If a control surface, such as the elevator, was immersed in this separated region, its effectiveness would be greatly diminished or entirely lost.

NACA addressed this problem by mounting the elevator on an all-moving horizontal tail, which provided reliable pitch control throughout the transonic regime. With this configuration, Yeager successfully reached a speed of approximately Mach 1.06 in level flight—the first controlled, sustained supersonic flight in history. After engine burnout, the aircraft glided to a safe landing on a dry lakebed in the Mojave Desert of California. Most subsequent supersonic aircraft adopted either an all-moving tailplane or tailless delta-wing configuration to avoid the severe adverse effects associated with STBLI (Pisano et al., 2006).

(*a*) (*b*)

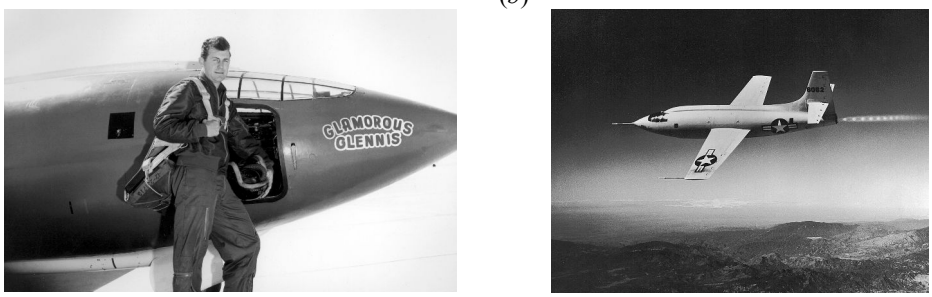

Figure 1.1: (a) Chuck Yeager stands in front of the Bell X-1, named (after his wife) Glamorous Glennis. Courtesy of U.S. Air Force. (b) Bell X-1, the first aircraft that broke the sound barrier in level flight in 1947. Courtesy of NASA.

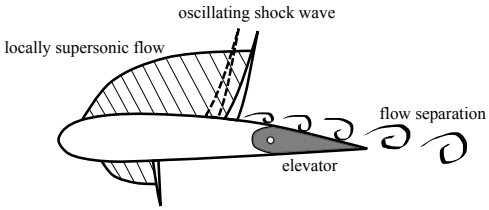

Figure 1.2: A schematic of the flow field over a transonic airfoil.

Today, supersonic flight appears almost routine. Half a century ago, the Concorde regularly carried passengers across the Atlantic at Mach 2, while aircraft such as the SR-71 Blackbird routinely cruised at speeds exceeding Mach 3. Yet these modern achievements do not imply that STBLI has become a solved problem.

Although we have long surpassed the “sound barrier”, the fundamental physics that governs high-speed flows remains profoundly challenging. In particular, the interaction between shock-waves and turbulent boundary-layers represents one of the most complicated and influential phenomena in this regime (Clemens and Narayanaswamy, 2014). These interactions are not merely academic curiosities but arise ubiquitously in practical high-speed configurations. In supersonic and hypersonic inlets, for example, impinging shocks and compression ramps are deliberately employed to decelerate and compress the incoming flow, inevitably generating strong shock wave/turbulent boundary-layer interactions. The resulting shock-induced separation, high-amplitude pressure fluctuation, and intense localized heating continue to dictate the performance, stability, and thermal protection requirements of supersonic and hypersonic vehicles. A representative example is the NASA X-43A scramjet-powered vehicle, in which multiple compression ramps ahead of the inlet generate a train of strong shocks that interact with the turbulent boundary layer on the forebody and inside the inlet, as shown in Figure 1.3. Despite extensive experimental and numerical efforts, managing these interactions remains a critical design challenge for hypersonic vehicles. Predicting—or even controlling—those detrimental effects is still one of the central problems in high-speed aerodynamics.

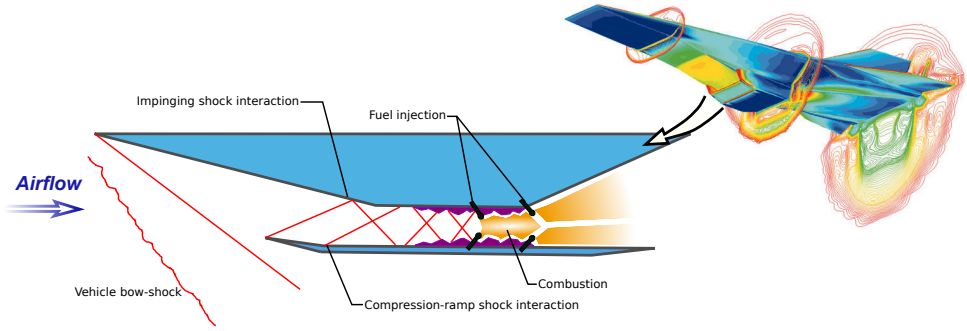

Figure 1.3: Schematic of the shock system related to the scramjet engine of NASA X-43A. The upper right image is adapted from NASA.

1

1.2. SHOCK-WAVE/TURBULENT BOUNDARY-LAYER INTERACTION

Before discussing the complexity of shock-wave/turbulent boundary-layer interaction, it is useful to first review the two fundamental components involved: shock wave and turbulent boundary layer (TBL). A clear understanding of these elements provides the necessary basis for examining the coupled phenomena observed in high-speed flows.

A shock wave is a discontinuity in a medium, marked by abrupt and irreversible changes in its state properties (Anderson, 2003). Shock waves arise fundamentally because pressure disturbances propagate at a finite speed—the local speed of sound. When a body moves subsonically, these disturbances travel upstream and allow the fluid to adjust smoothly. But if the body exceeds the speed of sound, the disturbances cannot outrun it and fail to inform the upstream flow. As a result, the compression generated by the body accumulates and collapses into a thin surface across which pressure, density, and velocity change abruptly. This accumulated discontinuity is the shock wave.

Shock waves occur frequently in both natural and engineering environments. Naturally, they are generated by phenomena such as lightning, earthquakes, volcanic eruptions, and meteorite impacts. On an even larger scale, a planetary bow shock also forms when Earth's magnetic field obstructs the supersonic flow of solar wind plasma (Ben-Dor et al., 2000). Human activity generates shock waves in many ways as well: through nuclear and chemical explosions, the sonic boom produced by supersonic aircraft and fast-moving projectiles, and bow shock structures enveloping reentry vehicles. Shock waves are characterized by an extremely small thickness, typically on the order of a few molecular mean free paths. Across this narrow region, the pressure, density, temperature, and entropy increase sharply, whereas the Mach number, flow velocity, and total pressure decrease. The process is adiabatic in the sense that no heat is exchanged with the surroundings; however, it is highly dissipative, leading to an irreversible rise in entropy. The total enthalpy remains constant across the shock. The upstream and downstream states are linked through the conservation laws of mass, momentum, and energy, commonly expressed by the Rankine–Hugoniot relations (Anderson, 2017). Shock waves arise in aerospace flows whenever the local Mach number exceeds unity and the flow must undergo a sudden adjustment in pressure, direction, or area. In practice, they may appear throughout high-speed vehicles in a wide variety of configurations in external and internal aerodynamics:

- External aerodynamics, such as the leading edges/nose tips, backward/forward facing steps, expansion/compression over transonic airfoil, and the surface of reentry vehicles.

- Internal aerodynamics, such as engine inlets, nozzles, and the flow passage of compressors/turbines.

The concept of boundary layer originates from Ludwig Prandtl's seminal work in 1904. He proposed that, in high Reynolds number flows, viscous effects are confined to a thin region adjacent to the wall surface, while the outer flow can be treated as inviscid (Schlichting and Gersten, 2016). The flow within this region may be either laminar or turbulent. However, in most aerospace applications, the boundary layer is turbulent, making shock-wave/turbulent boundary-layer interaction (STBLI) the primary focus in both research and engineering practice. The structure of the incoming turbulent boundary

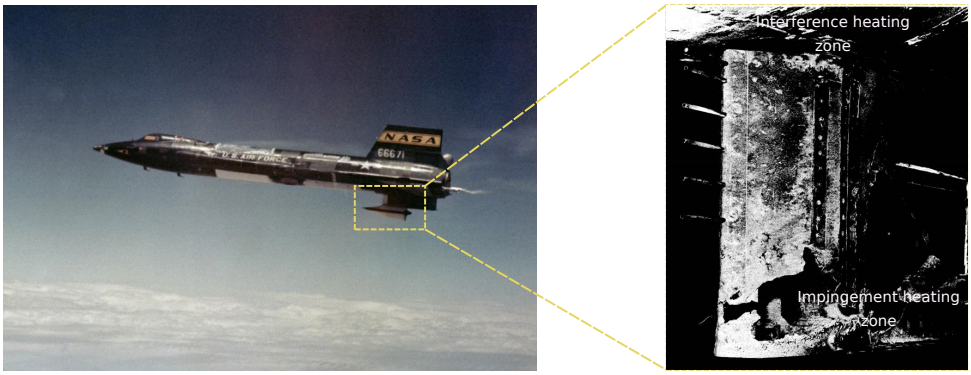

Figure 1.4: X-15 in flight (courtesy of NASA) and the ventral stabilizer after Flight 2-53-97. The pylon sustained severe damage due to the excessively high impingement and interference heating during the test (Watts, 1968).

layer—including its coherent motions and subsonic layer thickness—has a profound influence on the dynamics and characteristics of STBLI (Delery, 1985; Ganapathisubramani et al., 2009).

When a shock wave interacts with an incoming turbulent boundary layer—whether the shock is externally imposed, such as an impinging shock, or generated by surface curvature or flow turning—the strong adverse pressure gradient at the shock foot can readily separate the attached boundary layer, giving rise to a range of detrimental effects (Delery, 1985; Dolling, 2001). The primary physical consequences include increased wave drag (Babinsky and Ogawa, 2008; Nagamatsu and Ficarra, 1985), substantial total-pressure losses (Smith et al., 2002; Smith et al., 2003), and amplified unsteady pressure (Dolling and Murphy, 1983; Pasquariello et al., 2017) and heat loads (Schülein, 2006; Gaitonde, 2015; Fu et al., 2021) on the surface. These physical mechanisms, in turn, lead to several critical engineering challenges, such as reduced aerodynamic efficiency, failure of structural integrity, loss of control authority, inlet instability or unstart in air-breathing propulsion systems, and significant side loads in over-expanded rocket engines.

A striking historical example of the severe engineering consequences that can arise when STBLI is not properly accounted for occurred during the X-15 hypersonic research program in the early 1960s (Watts, 1968; Jenkins, 2007). The X-15, powered by a rocket engine, was designed to explore the feasibility and challenges of piloted hypersonic flight. For a series of tests at Mach numbers between 4 and 7, a dummy ramjet engine was mounted beneath the aircraft to evaluate high-speed carriage loads. During one of the first high-Mach flights, the ramjet detached during landing. Post-flight investigations (Watts, 1968) revealed that the leading edge and side surfaces of the pylon connecting the fuselage and the dummy ramjet engine were severely burned and structurally damaged, ultimately resulting in the loss of the ramjet assembly, as shown in Figure 1.4. In addition, in the vicinity of the pylon–fuselage junction, the ablative material was completely eroded, exposing the underlying skin, which became significantly deformed and approached structural failure.

The burn-through of the pylon is primarily attributed to a shock–shock interaction occurring ahead of the pylon. Specifically, the bow shock generated by the pylon intersected

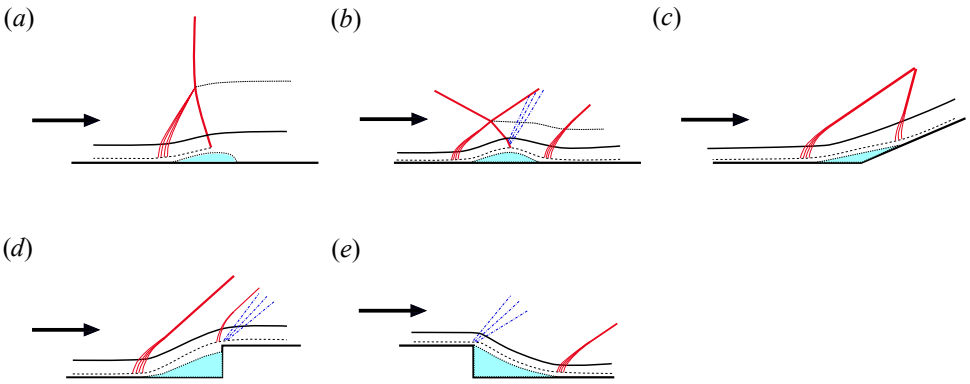

Figure 1.5: Schematic of canonical two-dimensional STBLI configurations. Adapted from Sabnis and Babinsky (2023) and Hu (2020).

with an incident shock originating from the leading edge of the ramjet cowling, forming an Edney Type IV interaction (Edney, 1967; Carl et al., 1998). This type of interaction is characterized by the formation of a supersonic jet that impinges on the surface, leading to an extreme local amplification of heat flux—with an order of magnitude higher than the undisturbed level—which ultimately caused the thermal failure and burn-through of the pylon.

STBLI also played a non-negligible role in the overall flow physics. The compression corner at the ramjet cowling generates a separation shock, which interacts with the upstream shock system. The inherent unsteadiness of STBLI introduces unsteadiness into the entire shock system, leading to significant fluctuations in the aerodynamic loading at the pylon leading edge. Such load fluctuations may contribute to structural high-temperature fatigue and exacerbate material degradation (Clemens, 2022). Furthermore, severe damage was observed near the pylon–fuselage junction, where the ablative layer was completely removed. This is attributed to interference heating caused by the interaction between the shock associated with the pylon leading edge and the fuselage boundary layer (Watts, 1968). In this interference region, the local heat-transfer rate increased by approximately a factor of 7 compared to the undisturbed boundary layer (Burbank, 1962), posing a significant threat to the structural integrity of the vehicle.

This incident highlights a critical lesson: in supersonic and hypersonic vehicles, STBLI must be carefully considered in design, as they often dictate the limiting thermal, structural, and aerodynamic constraints of the entire system.

Although many STBLI encountered in practical engineering applications are intrinsically three-dimensional, such as (double-) sharp fins, swept compression ramp, blunt fin, and (semi-) cone (Gaitonde and Adler, 2023; Sabnis and Babinsky, 2023). Canonical two-dimensional STBLI configurations remain the most widely studied in terms of their flow structures, unsteady dynamics, because they provide the fundamental understanding and reference data that guide guide flow control strategies in more complex three-dimensional STBLI cases. The most canonical two-dimensional configurations can be abstracted into the following simplified cases, see Figure 1.5: (1) normal shock,

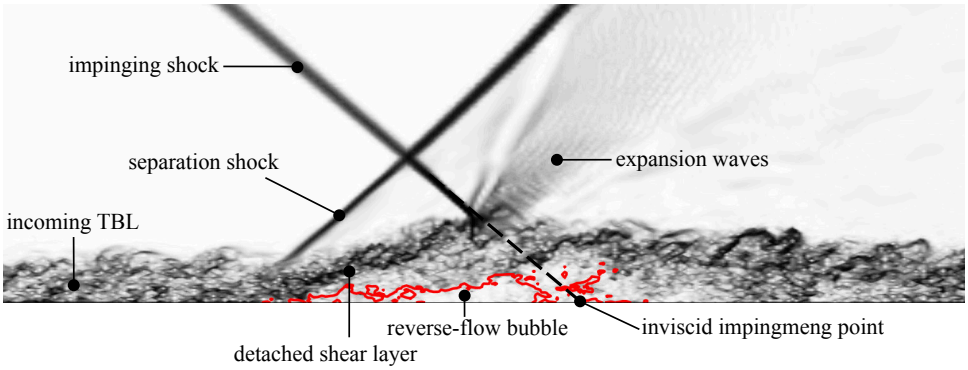

Figure 1.6: Numerical schlieren image of impinging shock interaction at Mach 2.0 and $Re_\tau \approx 355$ at the inviscid impingement point.

(2) oblique impinging shock, (3) compression ramp, (4) forward and backward facing steps (Sabnis and Babinsky, 2023; Hu, 2020). Among these canonical configurations, the impinging-shock interaction is one of the most common flow arrangements and is of particular interest in the present study. All passive control strategies investigated here are based on this type of interaction.

The general topology of a strong impinging shock interaction is shown in Figure 1.6. When the incident shock impinges on the wall, it imposes a strong adverse pressure gradient on the turbulent boundary layer (TBL). The low-momentum fluid near the wall lacks sufficient kinetic energy to overcome this gradient and therefore separates. Pressure disturbances generated by the impinging shock propagate upstream through the subsonic portion of the TBL. The resulting reverse-flow blocks the oncoming boundary-layer fluid and deflects it away from the wall, forming a "viscous bump". Compression waves generated ahead of this deflection coalesce into the so-called separation, or reflected, shock (Delery, 1985). This shock intersects the incident shock, which is itself reflected from the separation bubble as an expansion fan. Downstream of the bubble apex, the flow turns back toward the wall and reattaches, producing additional compression waves that may merge into a reattachment shock if they are sufficiently strong. Throughout the interaction, the TBL downstream of the interaction region becomes significantly thickened, and its turbulence is markedly amplified before progressively returning toward an equilibrium state (Pasquariello, 2018; Pirozzoli and Grasso, 2006).

1.3. LOW-FREQUENCY UNSTEADINESS

The unsteadiness associated with STBLI spans a broad range of frequencies, from the high-frequency turbulent fluctuations of the incoming boundary layer down to low-frequency shock motions that are one to two orders of magnitude lower (Delery, 1985). The low-frequency, large-scale motions have received particular attention over the past several decades, owing both to their significant implications for engineering applications and to the absence of a definitive physical explanation for their origin (Dolling and Murphy, 1983; Pirozzoli and Grasso, 2006; Dupont et al., 2006; Wu and Martin, 2008; Touber and

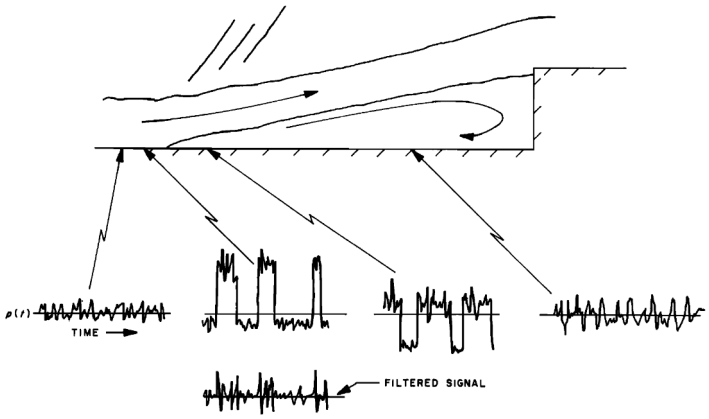

Figure 1.7: Sketch of the time variation of the pressure at different streamwise locations of the separated region in a Mach 3 forward-facing step flow (Adapted from Kistler (1964)).

Sandham, 2009; Pasquariello et al., 2017).

The low-frequency, large-scale motions primarily correspond to the expansion and contraction of the reverse-flow bubble, as well as the back-and-forth oscillation of the separation shock. Kistler (1964) was the first to report the pressure fluctuations near the shock foot in a supersonic forward-facing-step flow, where he identified a distinct low-frequency intermittent behavior in the pressure signal, see Figure 1.7. This behavior was explained by noting that, at any given instant, the wall-pressure distribution resembles a step function: a lower pressure upstream of the separation point and a higher pressure within the separated region. If this pressure jump is not stationary but instead wanders within a finite streamwise range, then the pressure recorded at any fixed location in this range naturally exhibits the intermittent features observed in the measurements. Dolling and Murphy (1983) also observed similar low-frequency intermittent pressure fluctuations near the shock foot in a Mach 3 compression ramp interaction case. Gonsalez and Dolling (1993) have found the mean velocity of the shock foot is essentially the same for upstream or downstream sweeps, and the velocity magnitude is usually around 2% to 4% of u_∞ regardless of the geometry or flow separation scale.

Considerable research effort has been put into the mechanism that drives this low-frequency motion. Generally speaking, previous interpretations of its origin can be grouped into two categories: upstream-driven mechanisms and downstream-driven mechanisms, although several new perspectives have emerged in recent years. An extensive summary was provided in a review paper from Clemens and Narayanaswamy (2014).

Upstream mechanism

Upstream mechnism relates the shock foot unsteadiness to the fluctuation within the upstream boundary layer. Plotkin (1975) proposed a mathematical model that shows that low-frequency motion can result from high-frequency forcing in analogy to a random-walk process. Touber and Sandham (2011) showed that the low-frequency motions in reflected STBLI arise intrinsically from the shock-boundary-layer coupling, which

behaves as a first-order low-pass filter. Their stochastic model, validated against LES, reproduces the observed broadband low-frequency response even under white-noise forcing, indicating that no specific upstream structures are needed.

Andreopoulos and Muck (1987) related the bursting events inside the incoming TBL with the shock unsteadiness by measuring wall-pressure under a Mach 3 compression ramp interaction. Furthermore, Erengil (1993) investigated a Mach 5 compression-ramp interaction and measured wall-pressure beneath the intermittent region. They found a clear correlation between the shock-foot velocity and upstream boundary-layer pressure fluctuations, as well as between the pressure beneath the separated flow and that beneath the intermittent region in swept-ramp configurations. These observations led them to conclude that the high-frequency, small-scale jitter of the shock is driven by upstream boundary-layer turbulence, whereas the low-frequency, large-scale shock motions are induced by the pulsations of the separation bubble. Uenalmis and Dolling (1994) proposed that a low-frequency thickening/thinning of the TBL may be linked to upstream/downstream motions of the shock. This proposition was later confirmed by Beresh et al. (2002) and Hou (2003), who used particle image velocimetry (PIV) to measure the upstream turbulent boundary layer while simultaneously acquiring wall-pressure data beneath the intermittent region. Their results showed that an instantaneously fuller velocity profile corresponds to a downstream shock motion, and vice versa.

Ganapathisubramani et al. (2006) used wide-field PIV measurements at wall-normal locations of 0.16 and 0.45 boundary layer thickness to identify elongated low- and high-speed regions (superstructures) in the upstream turbulent boundary layer of a Mach 2 compression-ramp interaction. They attributed the observed low-frequency unsteadiness to a combination of local effects associated with these *superstructures* and a global influence linked to the very-low-frequency motion of the spanwise-averaged surrogate separation line (Ganapathisubramani et al., 2009). Three-dimensional tomographic PIV measurements by Humble et al. (2009) further confirmed the presence of these streaky low- and high-speed structures. Their results also revealed a correlation between upstream velocity fluctuations and the surrogate separation location, aligned with Ganapathisubramani et al. (2007) and Wu and Martin (2008). Based on these observations, they proposed that the spanwise wrinkling of the separated flow is driven by the spanwise organization of the incoming structures, whereas the streamwise shock motion is governed by the bulk momentum of the incoming flow.

Downstream mechanism

Downstream mechanism attributes the low-frequency unsteadiness to the intrinsic dynamics of the separation bubble itself. Erengil and Dolling (1991) were the first to show that the shock motion is strongly correlated with the ensemble-averaged pressure histories under the separated shear layer, from the results of a Mach 5 compression ramp experiment; however, they did not establish a definitive temporal sequence between the two. Brusniak and Dolling (1994) showed that the unsteady shock motion in blunt-fin interactions is governed by a global, time-varying pressure distribution generated by the separated flow. In particular, they demonstrated that low-frequency pressure variations within the separation bubble precede and thereby drive changes in the direction of the separation shock foot, rather than responding to the shock motion. Thomas et al. (1994) demonstrated that the large-scale, low-frequency unsteadiness of a compression-ramp

shock is dominated not by upstream burst–sweep events but by the intrinsic "breathing" motion of the downstream separation bubble. Their phase-resolved pressure measurements show that fluctuations near the reattachment point lead—and thus drive—the opposite-direction motion of the shock foot, establishing the separation bubble as the first-order source of shock oscillation. Dupont et al. (2006) used high-frequency wall-pressure measurements to characterize the space-time organization of a Mach 2.3 shock-induced separated boundary layer. They showed that the reflected shock undergoes very-low frequency motions ($St \approx 0.03$), and that equally low-frequency fluctuations arise within the downstream separated bubble, demonstrating that the shock unsteadiness is tightly coupled to the large-scale dynamics of the separation bubble.

Pirozzoli and Grasso (2006), based on DNS of a Mach 2.25 impinging-shock interaction, proposed an acoustic-feedback mechanism in which acoustic waves generated by the interaction between coherent structures within the separation bubble and the incident shock propagate upstream and drive oscillations of the separation point. Later, Touber and Sandham (2009) confirmed this feedback-loop mechanism in a LES study of impinging shock interaction. They also demonstrated that upstream superstructures cannot be the driving mechanism for low-frequency shock unsteadiness, as the characteristic low-frequency motion persists even in LES where such structures are explicitly excluded by using a digital filter to generate inflow that prevents the development of large-scale upstream motions. Piponniau et al. (2009), as well as Wu and Martin (2008), proposed an entrainment/recharge mechanism, which assumed that the shear layer entrains the low-momentum fluid inside the separation bubble and hence depletes its mass, and that large-scale transverse motion of the shear layer near the mean attachment point recharges the bubble.

Morgan et al. (2013) show that while upstream superstructures can influence the instantaneous separation behavior, the dominant low-frequency unsteadiness arises primarily from the dynamics of the separated flow itself rather than being imposed by upstream structures. Grilli et al. (2012) and Pasquariello et al. (2017) applied dynamic mode decomposition (DMD) to investigate the dynamics of shock-induced separation bubbles in strong STBLI over a compression-expansion ramp and a planar wall, respectively, at Mach 3. In both studies, the low-frequency modes associated with the streamwise motion of the separation shock simultaneously captured the full breathing of the separation bubble, while showing little to no activity in the incoming boundary layer. They conclude that these results strongly support the intrinsic entrainment/recharge mechanism from Piponniau et al. (2009). Pasquariello et al. (2017) reported a clear coupling between separation-bubble dynamics and unsteady Görtler-like vortices. They argued that these vortices drive entrainment and may provide a persistent source of coherent forcing for the separation-shock system, originating near the reattachment line. Laguarda and Hickel (2024b) observed a clear suppression of low-frequency characteristics in a simulation where a shock-induced turbulent recirculation bubble forms over a backward-facing step designed to intercept the dynamic feedback, thereby providing strong support for the downstream feedback mechanism.

Recent views

As pointed out by Souverein et al. (2010), a growing consensus is that both upstream and downstream mechanisms contribute to the low-frequency unsteadiness in STBLI.

Which mechanism dominates depends on the interaction intensity: strong interactions are primarily driven by downstream instabilities, whereas weaker interactions are more strongly influenced by fluctuations in the incoming boundary layer (Clemens and Narayanaswamy, 2014). Some researchers have observed streamwise-elongated Görtler vortices undergoing slow motions with frequencies similar to that of the separation shock, particularly near the reattachment point and farther downstream; however, no strong proof for a causal relationship between the two phenomena has been established (Priebe et al., 2016; Pasquariello et al., 2017; Laguarda et al., 2024b).

1.4. CONTROL METHODS FOR STBLI

Given the severe unsteadiness and performance penalties associated with STBLI, considerable effort has been devoted to developing strategies to mitigate or control these interactions. In the following, we briefly review the main control approaches that have been proposed and their underlying mechanisms.

Control approaches for STBLI can be classified from different perspectives, depending on the practical objective or the associated properties of the control strategy.

For instance, control methods may be categorized according to the primary control target, depending on whether the strategy is intended to directly manipulate the shock system (shock control) or to modify the incoming turbulent boundary layer (boundary-layer control) (Babinsky and Ogawa, 2008). Shock-control approaches are more commonly associated with transonic airfoil applications and aim to reduce the additional wave drag induced by shock waves, for example, by weakening or smearing a strong shock into a series of weaker compression waves. Typical examples include surface-modification techniques such as bumps, humps, or steps, as well as bleed and porous surfaces (Liu et al., 2022; Li and Liu, 2019; Raghunathan, 1988; Tam et al., 2005; Roy et al., 2021). In contrast, boundary-layer control techniques focus on energizing the turbulent boundary layer to mitigate shock-induced flow separation. Representative methods include micro-vortex generators (Babinsky et al., 2007; Budich et al., 2013; Sun et al., 2019), pulsed jets (Amitay et al., 2001), plasma actuators (Webb et al., 2013), and suction (Pearcey, 1961).

Despite the above classification into two general categories, the inherent nonlinearity of STBLI implies that any control strategy will inevitably influence both the boundary layer and the shock system, with the resulting effects sometimes competing with each other. For example, energizing the boundary layer using vortex generators introduces additional compression waves, which subsequently interact with the main shock (Holden and Babinsky, 2007). Another noteworthy observation is that the boundary-layer shape factor has little influence on whether flow separation occurs (Délery et al., 1986), a behavior that can be explained by the presence of two competing effects. On the one hand, boundary-layer energization reduces the shape factor and brings the sonic line closer to the wall, thereby shortening the interaction length. The resulting pressure rise becomes more concentrated, leading to a sharper shock and a stronger adverse pressure gradient acting on the boundary layer. Such a sharper pressure rise may also amplify unsteady loads within the interaction. On the other hand, the increased near-wall momentum associated with a more energetic boundary layer enhances its resistance to separation. As a result of these competing mechanisms, the onset of separation is relatively insensitive to the boundary-layer shape factor.

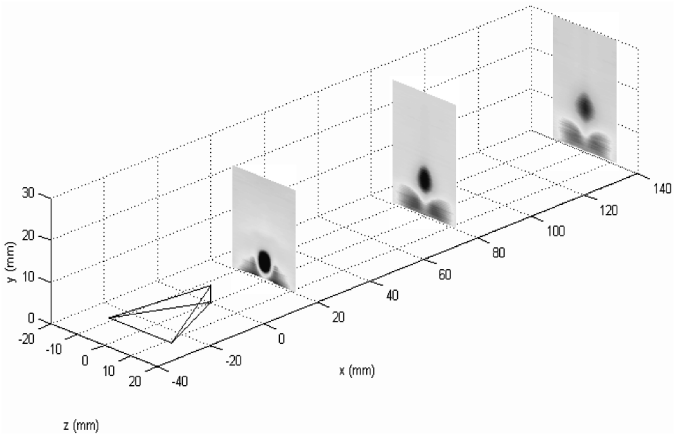

Figure 1.8: Induced counter-rotating vortices by MVG and redistribution of momentum. (Adapted from the work of Babinsky et al. (2009).

Another classification is based on whether external energy input is required during the control process, that is, whether the method is active or passive (Delery, 1985). Active control methods require external energy source—examples include suction, blowing, and pulsed jets (Vadillo et al., 2006; Verma and Manisankar, 2019). Although such techniques can be highly effective, they introduce additional system complexity, mass, and power requirements (Babinsky and Ogawa, 2008). Passive control methods, on the other hand, rely solely on geometric or flow-redirecting devices, such as shock-control bumps (Ogawa et al., 2008), pressure-feedback ducts or secondary recirculation jets (Pasquariello et al., 2014; Wu et al., 2022), and vortex generators (VG) (Lin, 2002; Panaras and Lu, 2015; Budich et al., 2013; Della Posta et al., 2023). These solutions are easier to implement, which explains their widespread adoption in engineering applications.

Among passive control methods, micro-vortex generators (MVG) with a height of approximately 40% of the boundary layer thickness are highly successful in the suppression of shock-induced flow separation by introducing a pair of counter-rotating streamwise vortices that energize the boundary layer and thereby delay flow separation (Babinsky and Ogawa, 2008; Babinsky et al., 2009), as shown in Figure 1.8. MVGs can also be combined with other control methods to achieve stronger control effects, such as bleeding and recirculation jet (Titchener and Babinsky, 2013; Wu et al., 2022).

A common drawback of many active and passive flow control methods is that their control performance is very sensitive to the installation location (Gaitonde and Adler, 2023). For example, Budich et al. (2013) placed MVGs at different upstream streamwise locations and showed that the structure of the separation region is substantially modified, as shown in Figure 1.9. In real application scenarios, the streamwise location of the incident shock impingement point may vary under different operating conditions; consequently, the control efficacy of an MVG placed at a fixed location can vary significantly. Furthermore, MVGs reduce parasitic drag compared to traditional VGs, they still lead to a substantial increase in drag when there is no flow separation (Rybalko et al., 2012),

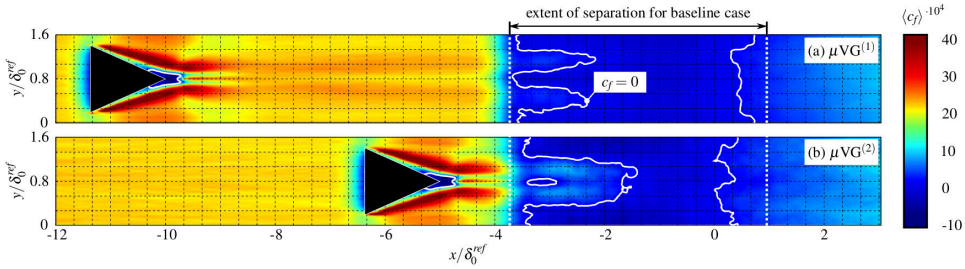

Figure 1.9: Skin friction coefficient distribution of MVG at different streamwise locations (Adapted from Budich et al. (2013)).

especially at high Reynolds number (Guo et al., 2022a). A further decrease of MVG height may help ease the increase of the pressure drag, but the control efficacy could be lost when the height is less than $0.1 - 0.3\,\delta_0$ (Panaras and Lu, 2015). This is also the case for other passive methods such as local suction and injection through pressure feedback ducts (Pasquariello et al., 2014) and shock control bumps (Ogawa et al., 2008). Therefore, in high-speed applications, there is always a compelling need for novel flow control methods that are insensitive to their installation location and have a low drag penalty.

Among the various passive strategies, surface-based approaches that modify the boundary layer structure without introducing large geometric protrusions are particularly attractive. For these reasons, we consider the utilization of surface roughness—particularly roughness with spanwise heterogeneity—a promising research direction, as it can induce secondary flows similar to those generated by micro-vortex generators, but with much smaller surface protrusions.

1.5. SPANWISE HETEROGENEOUS ROUGHNESS

Prandtl (1931) classified secondary flows into two categories and they can both be induced by the spanwise heterogeneous roughness.

The first kind is driven by pressure gradients induced by streamwise geometry variations. Notable examples include the streamwise vortices generated over micro-vortex generators (MVGs) or in convergent-divergent (C-D) riblets (Guo et al., 2022c), as well as the classic case of flow through a curved pipe, where a pair of counter-rotating Dean vortices develops in the cross-sectional plane. The intensity of such secondary flows can reach up to several tens of percent of the mainstream velocity (Nikitin et al., 2021). More recently, attention has been drawn to surface-based configurations, such as convergent–divergent and herringbone riblets, which can induce qualitatively similar streamwise-oriented secondary motions while introducing geometric perturbations that are one order of magnitude smaller than those of conventional MVGs. Nugroho et al. (2013) experimentally demonstrated that convergent–divergent riblets, despite having heights of only about 1% of the boundary-layer thickness, can induce strong large-scale spanwise periodicity in a turbulent boundary layer, consistent with the formation of counter-rotating streamwise roll modes.

It should be noted that a strict and universally accepted definition distinguishing her-

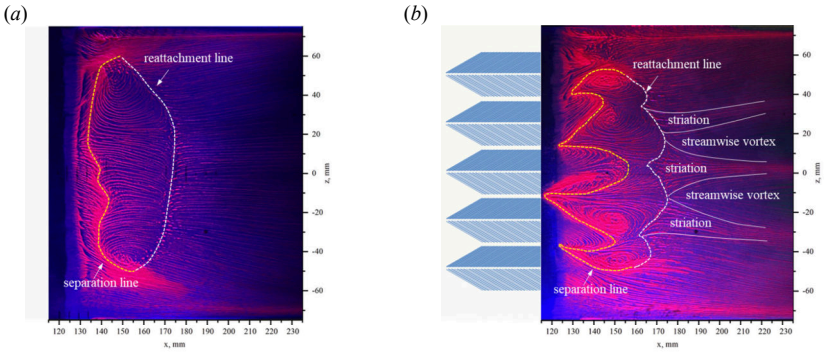

Figure 1.10: Oil flow images of the interaction zone of Mach 1.85 impinging shock interaction (a) baseline case, (b) herringbone riblets control (Adapted from Wen et al. (2024)).

ringbone and convergent–divergent riblets does not currently exist in the literature, and the geometric differences between the two configurations are relatively subtle. In practice, the two terms are often used to describe closely related chevron-like riblet arrangements. In the present context, the distinction is made primarily based on geometric connectivity: although both geometries share a similar chevron-like planform, herringbone riblets are characterized by a continuous streamwise-oriented central spine connecting individual riblet branches (Wen et al., 2024; Ye et al., 2025), whereas convergent–divergent riblets consist of locally converging and diverging riblet segments without a continuous backbone (Xu et al., 2018; Guo et al., 2022c; Mohammadikarachi et al., 2024).

Guo et al. (2022a) recently applied C-D riblets with a height less than 5% of the boundary layer thickness to control a Mach 2.9 compression-ramp STBLI flow. They found that C-D riblets are able to shrink the mean flow separation area by 56%, thus demonstrating that roughness-induced streamwise vortices are an effective way to control STBLI. Wen et al. (2024) experimentally investigated herringbone riblets with a height less than 2% of the boundary-layer thickness in a Mach 1.85 impinging shock wave/turbulent boundary-layer interaction. They reported that the relatively smooth separation line observed in the baseline case was replaced by a corrugated separation line, accompanied by a noticeable reduction in the overall size of the separation bubble, as shown in Figure 1.10. More recently, Ye et al. (2025) examined the effects of both sunken and protruding herringbone riblets on a Mach 3.4 compression-ramp STBLI and similarly found that the separation line became wavy in the presence of riblets, with the protruding configuration exhibiting a more pronounced separation-reduction effect. However, C-D riblets also generate pressure drag and should therefore be applied only in a narrow region. The positioning of the riblets patch relative to the shock impingement point is arguably crucial for the control performance.

Secondary flow of the second kind, was first experimentally reported by Nikuradse (1926), who observed eight counter-rotating vortices transporting high-momentum fluid from the duct core towards the corners, thereby distorting the streamwise velocity contours. In contrast to the secondary low of the first kind, the second kind is generated by the imbalance between local production and viscous dissipation of turbulent kinetic

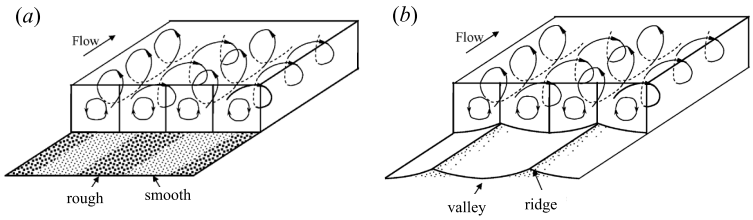

Figure 1.11: Schematic flow patterns of secondary flows over (a) strip type, and (b) ridge type roughness. Figure adapted from Wang and Cheng (2006).

energy and occurs only in turbulent flows. That is, turbulence-weak fluid is transported toward regions of high production, while turbulence-rich fluid is transported outward (Hwang and Lee, 2018). This type occurs exclusively in turbulent flows.

In a turbulent boundary layer, Prandtl's secondary flow of the second kind can be induced by both strip-type and ridge-type roughness (Kadivar et al., 2021), as illustrated in Fig. 1.11. Strip-type roughness consists of alternating smooth and rough strips, for which the resulting spanwise variation in wall shear stress plays the dominant role. In contrast, ridge-type roughness is formed by contouring an otherwise smooth wall, where wall elevation and the associated increase in wetted area are the primary contributors.

Stroh et al. (2020) performed direct numerical simulations of turbulent channel flow over surfaces with spanwise-varying drag and demonstrated that the topology of Prandtl's secondary motions strongly depends on the spanwise length scale of the drag heterogeneity. Frohnapfel et al. (2024) reported that spanwise-alternating roughness generates turbulent secondary motions that significantly modulate the local flow, while the global drag cannot be mapped onto classical homogeneous roughness correlations. Ridge-type rough surfaces that are homogeneous along the streamwise direction do not suffer from increased pressure drag, unlike strip-type roughness and C-D riblets. Streamwise homogeneous ridge-type roughness can therefore be applied over large areas, such that the control effectiveness is less sensitive to the installation location. These advantages make the ridge-type roughness a promising method to study. Zampiron et al. (2020) experimentally demonstrate that ridge-type roughness can induce secondary currents, such as upwash over the ridges and downwash in the valleys, resulting in the formation of low-momentum and high-momentum pathways within the turbulent boundary layer. The same conclusions are confirmed numerically by Zhdanov et al. (2024). Wangsawijaya et al. (2020) point out that the spacing between ridges, and the width and height of the ridge are the main contributing factors to the size of the secondary flows induced by the ridge-type roughness. Deyn et al. (2022b) have shown that the secondary motions exhibit a weak dependence on Reynolds number.

1.6. OBJECTIVES OF THIS DISSERTATION

Extensive research has been devoted to spanwise heterogeneous roughness, demonstrating its capability to induce secondary flows with significantly smaller protrusion into the flow compared with traditional vortex generators. With the development of high-fidelity numerical methods, including the immersed boundary method, together with the

rapid growth of available computational resources, a robust numerical framework is now available to facilitate systematic investigation of the effects of spanwise-heterogeneous roughness on impinging shock-wave/turbulent boundary-layer interactions.

The main objective of this dissertation is to explore the potential of spanwise heterogeneous roughness—specifically convergent-divergent (C-D) riblets and ridge-type roughness—as a novel passive control strategy for a Mach 2.0 impinging shock-wave/turbulent boundary-layer interaction. In this work, we answer the following research questions:

- How do the secondary flows induced by spanwise-heterogeneous roughness affect the upstream turbulent boundary layer prior to the interaction?
- How does spanwise-heterogeneous roughness modify the mean flow structure and the dynamics of the interaction region?
- How do geometric parameters, such as ridge spacing and ridge height, influence the control performance of ridge-type roughness on STBLI?
- How does the Reynolds number affect the control effectiveness of ridge-type roughness?
- Does spanwise-heterogeneous roughness alter the unsteadiness of the STBLI, and if so, through which underlying mechanisms?

1.7. LAYOUT OF THIS DISSERTATION

This dissertation is organized into six chapters. The present chapter provides an introduction to the historical and research background of the topic. A brief overview of the remaining chapters is given below.

Chapter 2 introduces the numerical methodologies employed in this work, including the governing equations, the adaptive local deconvolution method (ALDM) for large-eddy simulation, the immersed boundary method, and the turbulent inflow generation technique. In addition, methods used for the analysis of the results are introduced, including the intrinsic averaging, spectral analysis and dynamic mode decomposition.

Chapter 3 presents the investigation of C-D riblets. Results from two designed riblet configurations are compared with those of a baseline smooth-wall case, highlighting the effects of riblet-induced secondary flows on the upstream turbulent boundary layer and the interaction region, including significant modifications to the separation characteristics and wall-pressure fluctuations.

Chapter 4 presents and discusses the effects of ridge-type roughness on a low-Reynolds-number STBLI. The influences of geometric parameters, such as ridge spacing and ridge height, on the mean flow and interaction unsteadiness are examined in detail.

Chapter 5 extends the analysis to high-Reynolds-number STBLIs, considering identical flow conditions and rough-wall geometries under both inner and outer scaling. The influence of the Reynolds number on the control effectiveness with respect to the mean flow, interaction unsteadiness, and the underlying physical mechanisms is discussed.

Chapter 6 summarizes the main conclusions of this dissertation and outlines perspectives for future work.

2

METHODOLOGY

他山之石，可以攻玉。
The other mountain's stone can polish my jade.
诗经/ *The Book of Songs*

This chapter outlines the methodology adopted in this study. The overall workflow consists of two major components: the computational fluid dynamics (CFD) methods used to compute the flow field, and the analysis techniques applied to extract the underlying physics.

The first methods section introduces the governing equations for compressible turbulent flows, the discretization strategies, and the associated solution procedures implemented in the simulations. The Section 2.2 focuses on the flow analysis techniques. Intrinsic averaging used in the statistical post-processing for rough wall is introduced. To interrogate the large amount of unsteady data generated by the simulations, we employ several diagnostic tools, including spectral analysis and dynamic mode decomposition (DMD). These methods enable us to quantify the dominant frequencies, characterize the energetic flow structures, and identify the key dynamical features associated with both the baseline interaction and the modified cases with spanwise heterogeneous roughness.

Together, these methodological components form the foundation upon which the subsequent results and physical interpretations are built.

2.1. NUMERICAL METHODS

2.1.1. GOVERNING EQUATIONS

The physical problem is determined by the three-dimensional compressible Navier–Stokes equations with appropriate boundary and initial conditions, as well as the constitutive relations for the fluid properties. The conservation equations in Cartesian coordinates in integral form are:

$$\frac{\partial \overline{\boldsymbol{U}}}{\partial t} = -\frac{1}{V_N}\oint_{\partial\Omega_N} (\boldsymbol{C}(\boldsymbol{U}) + \boldsymbol{P}(\boldsymbol{U}) + \boldsymbol{D}(\boldsymbol{U}))\cdot \mathrm{d}A + \frac{1}{V_N}\oint_{\Omega_N} \boldsymbol{S}(\boldsymbol{U})\mathrm{d}V \tag{2.1}$$

where the state vector $\boldsymbol{U} = [\rho, \rho u_1, \rho u_2, \rho u_3, \rho E]$ represents the fluid density ρ, linear momentum ρu_i, and total energy $\rho E = \rho e + \rho u_k u_k/2$. The overbar indicates the volume average for an arbitrary control volume Ω_N. The total flux appears in Eq. (2.1) includes advection $\boldsymbol{C}$, and surface stresses, $\boldsymbol{P}$ and $\boldsymbol{D}$,

$$\boldsymbol{C}_i = u_i\boldsymbol{U},\ \boldsymbol{P}_i = \begin{bmatrix} 0 \\ \delta_{i1}p \\ \delta_{i2}p \\ \delta_{i3}p \\ u_k\delta_{ik}p \end{bmatrix},\ \boldsymbol{D}_i = -\begin{bmatrix} 0 \\ \tau_{i1} \\ \tau_{i2} \\ \tau_{i3} \\ u_k\tau_{ik} + q_i \end{bmatrix}, \tag{2.2}$$

where p is the pressure, u_i the velocity vector. The viscous stress tensor τ_{ij} follows the constitutive relation for an isotropic Newtonian fluid

$$\tau_{ij} = \mu\left(\frac{\partial u_i}{\partial x_j} + \frac{\partial u_j}{\partial x_i} - \frac{2}{3}\delta_{ij}\frac{\partial u_k}{\partial x_k}\right), \tag{2.3}$$

and the heat flux q_i is given by Fourier's law

$$q_i = -k\frac{\partial T}{\partial x_i}, \tag{2.4}$$

The fluid is air and modeled as a perfect gas with a specific heat ratio $\gamma = c_p/c_v = 1.4$ and a specific gas constant of $R = 287.05\ \mathrm{J(kg\cdot K)^{-1}}$. The volumetric and caloric equations of state are

$$p = \rho R T, \tag{2.5}$$

$$E = \frac{p}{\gamma - 1} + \frac{1}{2}\rho u_i u_i. \tag{2.6}$$

The dynamic viscosity μ depends on the static temperature T and is modeled as a power-law,

$$\mu = \mu_\infty \left(\frac{T}{T_\infty}\right)^{0.7}, \tag{2.7}$$

where μ_∞ and T_∞ represent the viscosity and temperature in the free stream. Finally, the thermal conductivity k is modeled with a constant Prandtl number $Pr = 0.72$

$$k = \frac{\gamma R}{(\gamma - 1)Pr}\mu. \tag{2.8}$$

2.1.2. DISCRETIZATION METHODS

The aforementioned three-dimensional Navier–Stokes Eq. (2.1) are solved using our in-house finite-volume solver INCA[1], which employs the adaptive local deconvolution method (ALDM) for implicit large-eddy simulation (ILES).

Large-eddy simulation (LES) is based on the separation of resolved and unresolved flow scales through a spatial filtering operation. For a generic variable ϕ, the filtered field is defined as

$$\overline{\phi}(x) = \int G(x - x')\,\phi(x')\,\mathrm{d}x' = G * \phi, \tag{2.9}$$

where G denotes a low-pass filter kernel. Applying this operation and subsequent discretization to a nonlinear transport equation,

$$\partial_t \phi + \partial_x F(\phi) = 0, \tag{2.10}$$

yields the discretized filtered equation

$$\partial_t \overline{\phi}_N + G * \partial_x F_N(\phi_N) = -G * \partial_x \mathcal{G}_{SGS} \tag{2.11}$$

where the overbar denotes the filtering, and the subscript N indicates the grid functions. Because the subgrid scales (SGS) cannot be recovered by reconstruction (i.e., $\phi_N \neq \phi$), the subgrid-stress residual is

$$\mathcal{G}_{SGS} = F(\phi) - F_N(\phi_N) \tag{2.12}$$

In explicit LES, $\mathcal{G}_{SGS}$ is approximated by an explicit closure model to achieve $M_{SGS} \approx \mathcal{G}_{SGS}$, such as Smagorinsky's eddy-viscosity model (Smagorinsky, 1963).

When solved numerically, the discrete solution $\overline{\phi}_N$ is inevitably influenced by the truncation error associated with the underlying discretization scheme. As a consequence,

[1] For additional information about the solver, please visit https://inca.cfd.

the governing equation effectively solved by the numerical method is not Eq. (2.11), but its corresponding modified differential equation (MDE):

$$\partial_t \overline{\phi}_N + G * \partial_x F_N(\phi_N) = -G * \partial_x \mathcal{G}_{SGS} + \mathcal{G}_M + \mathcal{G}_N \tag{2.13}$$

where $\mathcal{G}_M$ is the modeling error and $\mathcal{G}_N$ is the truncation error.

Standard explicit LES relies on the assumptions $\|\mathcal{G}_M\| \ll \|G * \partial_x \mathcal{G}_{SGS}\|$, $\|\mathcal{G}_N\| \ll \|G * \partial_x \mathcal{G}_{SGS}\|$, and $\breve{M}_{SGS} \doteq M_{SGS}$. Under these assumptions, the numerical discretization is expected to introduce only negligible errors compared with the modeled subgrid-scale (SGS) contribution.

However, as pointed out by Vreman et al. (1994), Ghosal (1996), Kravchenko and Moin (1997), among many others, high-order centered discretizations may generate truncation errors that are comparable in magnitude to the SGS term, i.e. $\|\mathcal{G}_N\| \approx \|G * \partial_x \mathcal{G}_{SGS}\|$. In such cases, the numerical errors can outweigh or distort the effect of physically sound SGS models, leading to unpredictable interactions between modeling and discretization. This limitation motivates the adoption of an implicit LES strategy in which modeling and discretization are treated in a unified manner.

By comparing Eq. (2.11) and (2.13), it becomes apparent that numerical truncation errors may effectively act as an implicit subgrid-scale (SGS) model, provided that

$$\mathcal{G}_N \approx -G * \partial_x \mathcal{G}_{SGS}, \tag{2.14}$$

at finite grid resolution h. Under this condition, the explicit SGS term M_{SGS} is no longer required, as the SGS effects are implicitly represented by the numerical discretization.

Based on this underlying philosophy, many implicit SGS approaches have been developed using nonlinearly stable discretization schemes (Grinstein et al., 2007), in which numerical regularization is primarily introduced to satisfy mathematical stability requirements. In such methods, the physical consistency of the resulting numerical dissipation with subgrid-scale turbulence dynamics is not explicitly enforced. In contrast, ALDM explicitly designs the truncation error to act as a physically consistent implicit SGS model through a regularized deconvolution–flux framework, thereby achieving controlled dissipation, low-Mach-number consistency, and robust handling of shock–turbulence interaction. It was initially designed by Hickel et al. (2006) for incompressible turbulence, then subsequently extended to compressible turbulent flows with shock waves (Hickel et al., 2014). With ALDM, numerical discretization and SGS modeling are fully integrated into a unified framework. In the following, a brief overview of the key elements of ALDM is provided, while readers are referred to the original publications for detailed formulation, implementation, and validation.

Finite-volume discretization

In ALDM, the finite-volume discretization of the governing equations Eq. (2.1) can be regarded as a filtering/convolution operation with a top-hat filter:

$$G(\mathbf{x}, V_j) = \begin{cases} \dfrac{1}{V_j}, & \mathbf{x} \in \Omega_j, \\ 0, & \text{else}, \end{cases} \tag{2.15}$$

where V_j represents the volume of the computational cell Ω_j. For a generic variable, the cell-averaged solution is given by

$$\overline{\phi}_j = G * \phi = \frac{1}{V_j} \int_{\Omega_j} \phi \, \mathrm{d}\, V \tag{2.16}$$

Reconstuction

To evaluate fluxes at cell interfaces, ALDM reconstructs left and right interface states from the cell-averaged variables. This reconstruction is interpreted as a regularized deconvolution of the finite-volume filter, which involves a non-linear combination of Lagrange interpolation polynomials.

First, at a cell interface $x_{j\pm1/2}$, a set of local polynomial reconstructions is defined as

$$\breve{g}^{\mp}_{k,r}\left(x_{j\pm1/2}\right) = \sum_{l=0}^{k-1} c^{\mp}_{k,r,l}(x_N)\,\overline{\phi}_N\left(x_{j-r+l}\right) \tag{2.17}$$

where k denotes the formal order of accuracy, r the stencil shift ($r \in \{0,\ldots,k\}$), and l the index within the stencil from x_{i-r} to $x_{i-r+k-1}$.

The grid-dependent coefficients $c^{\mp}_{k,r,l}(x_N)$, which are independent of ϕ, satisfy

$$\breve{g}^{\mp}_{k,r}(x_{j\pm1/2}) = \phi(x_{j\pm1/2}) + \mathcal{O}(h^k). \tag{2.18}$$

Their computation follows the procedures described by Shu (2006) or Hickel et al. (2006).

Next, ALDM adopts the idea of the weighted essentially non-oscillatory (WENO) scheme of Shu (2006) where a hierarchy of reconstructions with increasing order of accuracy is conducted at the cell interfaces.

$$\breve{\phi}^{\mp}_{k}(x_{j\pm1/2}) = \sum_{r=0}^{k-1} \omega^{\mp}_{k,r}(\gamma_{k,r},\overline{\phi}_N)\,\breve{g}^{\mp}_{k,r}(x_{j\pm1/2}), \tag{2.19}$$

where the adaptivity of the deconvolution operator is achieved by dynamically weighting the respective contributions by

$$\omega^{\mp}_{k,r}(\gamma_{k,r},\overline{\phi}_N) = \frac{\gamma_{k,r}\beta_{k,r}(\overline{\phi}_N)}{\sum_{s=0}^{k-1}\gamma_{k,s}\beta_{k,s}(\overline{\phi}_N)}. \tag{2.20}$$

$\gamma_{k,r}$ are free model parameters that are exploited to control error cancellations, and $\beta_{k,r}$ measures the smoothness of the grid function within the respective stencil and provides a non-linear adaptation of the deconvolution. The functional expression of $\beta_{k,r}$ is defined as (Hickel et al., 2014)

$$\beta_{k,r}(\overline{\phi}_N) = \left(\epsilon_\beta + \sum_{l=-r}^{k-r-2}\left(\overline{\phi}(x_{i+m+1}) - \overline{\phi}(x_{i+m})\right)^2\right)^{-2}, \tag{2.21}$$

where $\epsilon_\beta = 10^{-99}$ to prevent division by zero.

These reconstructions are eventually combined into the final reconstruction:

$$\breve{\phi}^{\mp}(x_{j\pm1/2}) = \sum_{k=1}^{K} \alpha_k \breve{\phi}_k^{\mp}(x_{j\pm1/2}), \text{ with } K = 3. \tag{2.22}$$

Note that the weights α_k are chosen to form a normalized convex combination of the reconstructions of different orders. In the present work, $\alpha_k = 1/3$ has been chosen.

Numerical flux function

The numerical flux in ALDM is formulated as

$$\breve{\boldsymbol{F}}_{j\pm1/2} = \boldsymbol{F}\left(\frac{\breve{\boldsymbol{\phi}}^{+} + \breve{\boldsymbol{\phi}}^{-}}{2}\right) - \boldsymbol{R}\cdot\left(\breve{\boldsymbol{\phi}}^{+} - \breve{\boldsymbol{\phi}}^{-}\right), \tag{2.23}$$

where the first term is the physical Navier-Stokes flux, and it is computed from the mean of both reconstructions of the unfiltered solution at the considered cell face to achieve maximum order of consistency. The mismatch between left and right reconstructed states at a cell face, which appears in the second term, represents the irreducible deconvolution residual associated with unresolved scales. The second term provides controlled numerical regularization, where the dissipation matrix $\boldsymbol{R}$ scales with local velocity differences.

Following this framework, the approximation of the numerical convective flux for the mass, momentum, and energy conservation equations at an arbitrary cell face is, respectively

$$\breve{C}_i^{\rho} = \breve{u}_i^{*}\frac{\breve{\rho}^{+} + \breve{\rho}^{-}}{2} - R_i^{\rho}\left(\breve{\rho}^{+} - \breve{\rho}^{-}\right) \tag{2.24a}$$

$$\breve{C}_i^{\rho u_k} = C_i^{\rho}\frac{\breve{u}_k^{+} + \breve{u}_k^{-}}{2} - R_i^{\rho u}\frac{\breve{\rho}^{+} + \breve{\rho}^{-}}{2}\left(\breve{u}^{+} - \breve{u}^{-}\right) \tag{2.24b}$$

$$\breve{C}_i^{\rho e} = \breve{u}_i^{*}\frac{\widetilde{\rho e}^{+} + \widetilde{\rho e}^{-}}{2} + \frac{\breve{u}_k^{+} + \breve{u}_k^{-}}{2}\left(\breve{C}_i^{\rho u_k} - \frac{\breve{u}_k^{+} + \breve{u}_k^{-}}{4}\breve{C}_i^{\rho}\right) - R_i^{\rho e}\left(\widetilde{\rho e}^{+} - \widetilde{\rho e}^{-}\right). \tag{2.24c}$$

where the transport velocity $\breve{u}_i^{*}$ is defined as the following to ensure pressure-velocity coupling

$$\breve{u}_i^{*} = \frac{\breve{u}_i^{+} + \breve{u}_i^{-}}{2} - \frac{\alpha_3}{\breve{c}}\frac{\breve{p}_3^{+} - \breve{p}_3^{-}}{\breve{\rho}^{+} - \breve{\rho}^{-}}. \tag{2.25}$$

The definition of the pressure flux is direct

$$\breve{\boldsymbol{P}}_i = \begin{bmatrix} 0 \\ \delta_{i1}(\breve{p}^{+} + \breve{p}^{-})/2 \\ \delta_{i2}(\breve{p}^{+} + \breve{p}^{-})/2 \\ \delta_{i3}(\breve{p}^{+} + \breve{p}^{-})/2 \\ \breve{u}_i^{*}(\breve{p}^{+} + \breve{p}^{-})/2 \end{bmatrix}. \tag{2.26}$$

The dissipation matrix $\boldsymbol{R}$ is constructed such that numerical dissipation scales with local velocity differences rather than acoustic signal speeds, ensuring asymptotic consis-

tency in the low-Mach-number limit.

$$\boldsymbol{R}_i = \begin{bmatrix} R_i^{\rho} \\ R_i^{\rho u} \\ R_i^{\rho u} \\ R_i^{\rho u} \\ R_i^{\rho e} \end{bmatrix} = \begin{bmatrix} \sigma^{\rho} \, |\breve{u}_i^{+} - \breve{u}_i^{-}| \\ \sigma^{\rho u} |\breve{u}_1^{+} - \breve{u}_1^{-}| \\ \sigma^{\rho u} |\breve{u}_2^{+} - \breve{u}_2^{-}| \\ \sigma^{\rho u} |\breve{u}_3^{+} - \breve{u}_3^{-}| \\ \sigma^{\rho e} |\breve{u}_i^{+} - \breve{u}_i^{-}| \end{bmatrix} + f_s \frac{|\breve{u}_i^{*}| + |\breve{u}_i^{+} - \breve{u}_i^{-}|}{2} \begin{bmatrix} 1 \\ 1 \\ 1 \\ 1 \\ 1 \\ 1 \end{bmatrix}, \tag{2.27}$$

where σ^{ρ}, $\sigma^{\rho u}$, and $\sigma^{\rho e}$ are case-independent model parameters of order 1.

The free parameters $\{\alpha, \gamma, \sigma\}$ are calibrated to reproduce the spectral dissipation characteristics of canonical turbulent flows. As a result, the truncation error introduced by the numerical flux acts as a physically motivated implicit SGS model. Additional shock-related dissipation is activated selectively through a modified flow-dependent Ducros sensor (Laguarda, 2024; Ducros et al., 1999)

$$f_s = \begin{cases} 1, & \frac{|\nabla \cdot \overline{\boldsymbol{u}}|}{0.01 \|\nabla \times \overline{\boldsymbol{u}}\|_1 + \|\mathbf{I} \odot \nabla \overline{\boldsymbol{u}}\| + \varepsilon_s} \geq 0.98 \text{ and } \nabla \cdot \overline{u} < 0, \\ 0, & \text{else} \end{cases} \tag{2.28}$$

where $\varepsilon_s = 10^{-15}$, allowing stable and non-oscillatory capturing of discontinuities without compromising the resolution of smooth turbulence (Hickel et al., 2014).

Additionally, gradients appearing in the viscous flux tensor are discretized using linear second-order central differences. Time integration is performed using an explicit third-order Runge–Kutta scheme.

In summary, ALDM provides a unified numerical framework in which spatial discretization, implicit SGS modeling, and shock capturing are intrinsically coupled. Compared with traditional ILES approaches that rely on incidental numerical dissipation, ALDM offers controlled spectral dissipation and asymptotic consistency in the low-Mach-number limit by scaling numerical dissipation with local velocity differences rather than acoustic signal speeds. At the same time, solution-adaptive reconstruction and selective flux regularization enable robust and non-oscillatory shock capturing, while preserving the high spectral resolution of smooth turbulent structures, which is comparable to that achieved by a sixth-order central difference scheme. These properties make ALDM particularly well-suited for the simulation of STBLI, in which broadband turbulent fluctuations coexist with strong compression waves and both phenomena influence the near-wall dynamics and separation behavior.

The INCA solver has been extensively validated and successfully applied to a wide range of shock–turbulent boundary layer interaction (STBLI) configurations, including compression ramps (Grilli et al., 2012), shock impingement (Pasquariello et al., 2017; Laguarda et al., 2024b; Laguarda et al., 2024a), and forward- and backward-facing steps (Hu et al., 2021; Hu et al., 2022).

2.1.3. IMMERSED BOUNDARY METHOD

In numerical simulations of turbulent flows in practical engineering, such as rough surfaces, the accurate representation of complex wall geometries is a non-trivial and

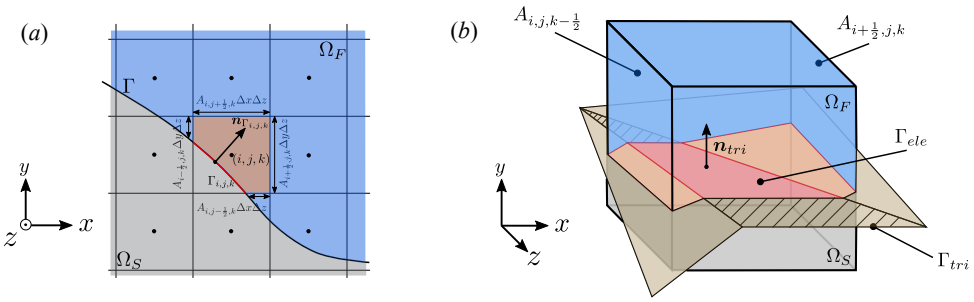

Figure 2.1: (a) Two-dimensional schematic of a cut-cell. (b) Schematic of a three-dimensional cut-cell intersected by the triangulated surface.

challenging task. For complex geometries, traditional body-fitted meshes struggle to accommodate the highly irregular and skewed surface features. Enforcing grid conformity to such geometries often leads to poor mesh quality, for instance, in terms of reduced orthogonality, and requires substantial manual effort and time-consuming mesh optimization.

Immersed boundary (IB) methods have emerged as an effective strategy to alleviate the difficulties associated with complex, and possibly moving, geometries by embedding the solid boundaries within a Cartesian mesh and treating the fluid–solid interface using dedicated numerical techniques. This approach significantly simplifies mesh generation and facilitates the application of CFD to practical problems. The concept of the *immersed boundary method* was first introduced by Peskin (1972) for the simulation of cardiac mechanics. After several decades of development, the method has become increasingly popular in the field of fluid mechanics. Comprehensive reviews and methodological overviews can be found in Mittal and Iaccarino (2005), Griffith and Patankar (2020), Verzicco (2023), Başkaya et al. (2024) and Verzicco et al. (2025).

The main procedures of IB methods consist of first identifying and classifying grid points as fluid, solid, or interfacial, and then defining a strategy to enforce the boundary conditions at the fluid–solid interface, as illustrated in a two-dimensional sketch in Figure 2.1(a). The first step can be automated using efficient algorithms such as ray tracing (O'Rourke, 1998) and needs to be performed only once at the beginning of the simulation for fixed bodies. Most IB methods accomplish the second step by explicitly or implicitly introducing a continuous or discrete volumetric forcing term (Verzicco, 2023).

In the current thesis, in order to resolve the rough wall geometry, a second-order cut-cell-based IB method of Meyer et al. (2010) and Örley et al. (2015) is utilized. Unlike traditional IB methods that impose boundary conditions by simple extrapolation or as a non-conservative source term that is smeared over several cells at the interface, the cut-cell-based IB method modifies the finite-volume flux balance to consider the exact geometry of the fluid part of cells (Seo and Mittal, 2011). In essence, cells intersected by the wall geometry are geometrically modified, and are therefore referred to as *cut cells*. The cut-cell-based IB method is fully conservative by construction (finite-volume flux balance) and represents the fluid-solid interface as sharply as a body-fitted mesh method. The accuracy and convergence have been thoroughly verified through direct comparison

with results obtained using body-fitted grids in several previous studies (Meyer et al., 2010; Başkaya et al., 2024).

In our IB method, the surface of the immersed body is triangulated into a set of triangles Γ_{tri}. A Cartesian computational cell $\Omega_{i,j,k}$ might be intersected by one or several triangles and results in a collection of interface elements $\Gamma_{ele} = \Gamma_{tri} \cap \Omega_{i,j,k}$, as illustrated in Figure 2.1(b). The integral form of Eq. (2.1) applied on the fluid part of cell $\Omega_{i,j,k}$ over a sigle time step $\Delta t = t^{n+1} - t^n$ reads

$$\int_{t^n}^{t^{n+1}} \int_{\Omega_{i,j,k} \cap \Omega_F} \partial_t \boldsymbol{U} \, \mathrm{d}V \, \mathrm{d}t + \int_{t^n}^{t^{n+1}} \int_{\partial(\Omega_{i,j,k} \cap \Omega_F)} \boldsymbol{\mathcal{F}}(\boldsymbol{U}) \cdot \boldsymbol{n} \, \mathrm{d}S \, \mathrm{d}t = 0, \tag{2.29}$$

where $\partial(\Omega_{i,j,k} \cap \Omega_F)$ denotes the wetted surface of the cut-cell $\Omega_{i,j,k}$ and $\boldsymbol{\mathcal{F}}$ is the total flux. Considering a volume average of the conserved variables,

$$\overline{\boldsymbol{U}}_{i,j,k} = \frac{1}{\alpha_{i,j,k} V_{i,j,k}} \int_{\Omega_{i,j,k} \cap \Omega_F} \boldsymbol{U} \mathrm{d}x \mathrm{d}y \mathrm{d}z, \tag{2.30}$$

and assuming a forward Euler time integration scheme results in the discrete form of Eq. 2.29

$$\begin{aligned} \alpha^{n+1}_{i,j,k} \overline{\boldsymbol{U}}^{n+1}_{i,j,k} = \alpha^{n}_{i,j,k} \overline{\boldsymbol{U}}^{n}_{i,j,k} \\ + \frac{\Delta t}{\Delta x_i} \left[A^n_{i-\frac{1}{2},j,k} \boldsymbol{\mathcal{F}}^{(1,n)}_{i-\frac{1}{2},j,k} - A^n_{i+\frac{1}{2},j,k} \boldsymbol{\mathcal{F}}^{(1,n)}_{i+\frac{1}{2},j,k} \right] \\ + \frac{\Delta t}{\Delta y_j} \left[A^n_{i,j-\frac{1}{2},k} \boldsymbol{\mathcal{F}}^{(2,n)}_{i,j-\frac{1}{2},k} - A^n_{i,j+\frac{1}{2},k} \boldsymbol{\mathcal{F}}^{(2,n)}_{i,j+\frac{1}{2},k} \right] \\ + \frac{\Delta t}{\Delta z_k} \left[A^n_{i,j,k-\frac{1}{2}} \boldsymbol{\mathcal{F}}^{(3,n)}_{i,j,k-\frac{1}{2}} - A^n_{i,j,k+\frac{1}{2}} \boldsymbol{\mathcal{F}}^{(3,n)}_{i,j,k+\frac{1}{2}} \right] \\ + \frac{\Delta t}{V_{i,j,k}} \boldsymbol{\chi}_{i,j,k}, \end{aligned} \tag{2.31}$$

where $V_{i,j,k} = \Delta x_i \Delta y_j \Delta z_k$ is the total volume of the cut-cell, and $\alpha_{i,j,k}$ is the fluid volume fraction of the cut-cell, and A is the effective fluid wetted cell-face aperture, which satisfy $0 \leq \alpha_{i,j,k}, A \leq 1$. $\boldsymbol{\mathcal{F}}^{(1)}$, $\boldsymbol{\mathcal{F}}^{(2)}$, $\boldsymbol{\mathcal{F}}^{(3)}$ denote the face-averaged numerical fluxes across the regular cell faces in the x, y, and z directions, and the interface exchange term $\boldsymbol{\chi}_{i,j,k} = \sum_{ele} \boldsymbol{\chi}_{ele}$ accounts for the forces acting on $\Gamma_{i,j,k}$ and flux passing through $\Gamma_{i,j,k}$ by summing up the contribution of cut-elements associated with $\Omega_{i,j,k}$. $\boldsymbol{\chi}$ includes terms for pressure, viscous effects and heat transfer at the element interface

$$\boldsymbol{\chi}_{ele} = \boldsymbol{\chi}^p_{ele} + \boldsymbol{\chi}^v_{ele} + \boldsymbol{\chi}^{ht}_{ele}. \tag{2.32}$$

$\boldsymbol{\chi}^p_{ele}$ requires the interface pressure p^Γ_{ele} at the cut-element face centroid $\boldsymbol{x}_{ele}$, which can be calculated by solving a one-sided face-normal Riemann problem with an approximate or exact Riemann solver. Both the viscous $\boldsymbol{\chi}^v_{ele}$ and heat transfer $\boldsymbol{\chi}^{ht}_{ele}$ contribution require the evaluation of flow gradients at $\boldsymbol{x}_{ele}$. The reader is referred to Örley et al. (2015) and Pasquariello et al. (2016) for further details.

A drawback of the cut-cell method is that the fluid volume fraction in some cut cells can become very small, which may lead to numerical instability when explicit time-integration schemes are employed. To address this issue, several stabilization techniques

have been proposed, including cell merging and cell linking. In the cell-merging approach, the fluid portion of cut cells whose centers lie within the solid domain is merged with adjacent fluid cells (Ye et al., 1999). In contrast, cell linking stabilizes the scheme by redistributing numerical fluxes to neighboring cells while preserving local conservation (Kirkpatrick et al., 2003). Örley et al. (2015) originally used the conservative mixing of conserved quantities with several neighbour cells, as proposed by Meyer et al. (2010). For the present work, however, a conservative cell-merging procedure is applied for stabilization.

2.1.4. BOUNDARY CONDITIONS

For STBLI problems, the proper treatment of boundary conditions plays a critical role in ensuring both numerical stability and physical fidelity. Beyond the conventional requirement of non-reflecting inflow and outflow conditions to prevent spurious wave reflections (Poinsot and Lele, 1992), additional care must be taken in specifying physically realistic boundary conditions tailored to the underlying flow physics. In the following, the generation of turbulent inflow, the wall boundary treatment employed in the immersed boundary framework are highlighted.

Turbulent inflow condition

The incoming TBL strongly influences the development of STBLI and must be prescribed as realistically as possible in order to avoid introducing artificial effects that could contaminate the low-frequency dynamics of STBLI. Previously, researchers obtained the realistic incoming TBL by triggering the transition of a laminar boundary layer to the turbulent state with perturbations such as wall-normal blowing and suction (Pirozzoli et al., 2004; Zhu et al., 2017). But this method requires a very long computation domain upstream of the interaction region to allow for the full development of the TBL, usually hundreds of boundary layer thicknesses, in which much computation cost is wasted, especially for LES and DNS. Turbulence can also be introduced directly at the inlet of the computational domain, this kind of turbulence generation techniques are classified into recycling methods and synthetic methods. The former extracts the required inflow state from an auxiliary simulation or directly from a downstream plane with appropriate rescaling (Lund et al., 1998). Recycling may introduce spurious low-frequency or long-wavelength structures, which will modulate the downstream interaction dynamics. The synthetic method, on the other hand, constrains random fluctuations to meet the prescribed statistics and recover a target coherence or energy spectrum (Klein et al., 2003; Xie and Castro, 2008). The digital filter (DF) method belongs to synthetic methods, which essentially imposes target spatial and temporal correlations on random fields via an explicit filter. This method does not bring undesired low-frequency content and has a relatively short acceptable induction length, which extends only approximately 10 boundary layer thicknesses.

A digital filter with improved accuracy and computational performance, introduced by Laguarda and Hickel (2024a), is adopted. The main procedures are as follows:

1. At every time step, three slices of uncorrelated Gaussian random numbers $\mathcal{S}_i$, with $i = \{1,2,3\}$, are generated. Each slice has zero mean and unit variance, and is uncorrelated from the others.

2. A two-dimensional spatial filter is then applied to each random slice in order to impose spatial coherence for the three velocity components. The two-dimensional filter kernel is defined as the tensor product of two one-dimensional kernels. The target longitudinal two-point correlations are assumed to be of exponential form,

$$R(r) = \exp\left(-\frac{\pi r}{2I_L}\right) \tag{2.33}$$

where I_L is the prescribed integral length scale, which may vary for different random fields, directions, and wall-normal distances. For a uniform grid with spacing h with $I_L = nh$ and $r = kh$, the following relation was proposed by Xie *et al.* to approximate the discrete filter coefficients b_k

$$b_k = \frac{\tilde{b}_k}{\sqrt{\sum_{j=-N}^{N} \tilde{b}_j^2}}, \text{ and } \tilde{b}_k \approx \exp\left(-\frac{\pi|k|}{n}\right) \tag{2.34}$$

where N is the filter support, typically chosen as $N \geq 2n$. The filtered fields are denoted as $\tilde{\mathcal{S}}_i$.

For the transversal correlations, the exponential correlation in Eq. 2.33 has been shown to provide a poor approximation of turbulent correlations (Pirozzoli and Bernardini, 2011). Laguarda and Hickel (2024a) therefore proposed an alternative target correlation function,

$$R(r) = \left(1 - \frac{r}{I_L}\right)\exp\left(-\frac{r}{I_L}\right). \tag{2.35}$$

Eq. 2.35 allows for negative correlations and more closely resembles transversal velocity correlation observed in DNS. The corresponding discrete filter coefficients in the transversal directions are approximated as

$$\tilde{b}_k = \left(1 - \left(\frac{|k|}{n}\right)^{0.3}\right)\exp\left(-\frac{|k|}{n}\right). \tag{2.36}$$

3. Temporal coherence is also assumed to follow an exponential decay and is imposed via a recursive digital filter,

$$\mathcal{G}_i(t) = \mathcal{G}_i(t-\Delta t)\exp\left(-\frac{\pi\Delta t}{2I_T}\right) + \tilde{\mathcal{S}}_i(t)\left[1 - \exp\left(-\frac{\pi\Delta t}{I_T}\right)\right]^{1/2} \tag{2.37}$$

where I_T is the target time scale. The resulting fields $\mathcal{G}_i$ are correlated in both space and time.

4. The inflow velocity is constructed as $\tilde{u}_i(t) = \tilde{U}_i + u_i''(t)$ where $\tilde{U}_i$ denotes target mean velocity profile. The instantaneous fluctuations are obtained through $u_i''(t) = a_{ij}\,\mathcal{G}_j(t)$, with a_{ij} obtained from the Cholesky decomposition of the target Reynolds stress tensor. This transformation, originally proposed by Lund et al. (1998), rescales the unit-variance random fields to reproduce the prescribed second-order statistics.

5. For compressible simulations, thermodynamic fluctuations are generated using the strong Reynolds analogy (SRA):

$$T'' = -\frac{\tilde{U}_1}{c_p} u_1'', \text{ and } \rho' = -\frac{\overline{\rho}}{\overline{T}} T''. \tag{2.38}$$

where c_p is the specific heat at constant pressure and $\overline{\rho}$, $\overline{T}$ are the mean density and temperature, thereby completing the inflow specification.

In this study, the first- and second-order statistical moments prescribed at the inflow plane are based on the DNS results of Pirozzoli and Bernardini (2011) and Pirozzoli and Bernardini (2013), obtained for supersonic turbulent boundary layers at $M_\infty = 2.0$ and comparable friction Reynolds numbers.

Wall boundary conditions

Interaction of the fluid with a solid interface is modeled by an interface exchange term $\boldsymbol{\chi}_{ele}$ as introduced in Eq. 2.32. The pressure term is

$$\boldsymbol{\chi}^p_{\text{ele}} = \begin{bmatrix} 0 \\ p_{\Gamma,\text{ele}} \Delta\Gamma_{\text{ele}} n_1^{\Gamma,\text{ele}} \\ p_{\Gamma,\text{ele}} \Delta\Gamma_{\text{ele}} n_2^{\Gamma,\text{ele}} \\ p_{\Gamma,\text{ele}} \Delta\Gamma_{\text{ele}} n_3^{\Gamma,\text{ele}} \\ p_{\Gamma,\text{ele}} \Delta\Gamma_{\text{ele}} \left(\mathbf{n}^{\Gamma,\text{ele}} \cdot \mathbf{v}^{\Gamma,\text{ele}}\right) \end{bmatrix}, \tag{2.39}$$

where $\Delta\Gamma_{\text{ele}}$ is the element surface area, $\mathbf{n}^{\Gamma,\text{ele}} = [n_1^{\Gamma,\text{ele}}, n_2^{\Gamma,\text{ele}}, n_3^{\Gamma,\text{ele}}]$ is the element normal vector obtained directly from the surface triangle, and $\mathbf{v}^{\Gamma,\text{ele}}$ is the interface velocity. The element interface pressure $p_{\Gamma,\text{ele}}$ is obtained by solving a one-sided face-normal Riemann problem with a suitable approximate or exact Riemann solver.

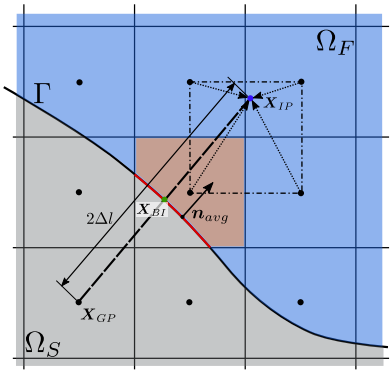

Figure 2.2: Schematic of the ghost-cell extending procedure for a cut-cell.

The viscous stress at the boundary is modeled by

$$\boldsymbol{\chi}^{v}_{\text{ele}} = \begin{bmatrix} 0 \\ D_1 \\ D_2 \\ D_3 \\ C \end{bmatrix}, \tag{2.40}$$

where the contribution to the momentum equation is

$$\mathbf{D} = \int_{\Gamma_{\text{ele}}} \bar{\tau} \cdot \mathbf{n}^{\Gamma,\text{ele}} \, dS \tag{2.41}$$

and the contribution to the energy equation is

$$C = \int_{\Gamma_{\text{ele}}} \left(\bar{\tau} \cdot \mathbf{v}^{\Gamma,\text{ele}} \right) \cdot \mathbf{n}^{\Gamma,\text{ele}} \, dS, \tag{2.42}$$

where $\bar{\tau}$ denotes the local viscous stress tensor.

In case of an isothermal interface, the heat transfer across the fluid–solid-boundary

$$q = \int_{\Gamma_{\text{ele}}} k \nabla T \cdot \mathbf{n}^{\Gamma,\text{ele}} \, dS, \tag{2.43}$$

needs to be taken into account within the flux balance of the cut-cell by the heat transfer term

$$\boldsymbol{\chi}^{ht}_{\text{ele}} = \begin{bmatrix} 0 \\ 0 \\ 0 \\ 0 \\ q \end{bmatrix}. \tag{2.44}$$

In the context of IB methods, cells located inside the solid region of the computational domain and adjacent to the fluid–solid interface, referred to as ghost cells, are assigned ghost states to satisfy the prescribed $\boldsymbol{\chi}_{ele}$. These ghost states enforce the boundary conditions at the interface without requiring any modification of the interpolation stencils used in the finite-volume reconstruction scheme. The ghost-cell methodology originally proposed by Mittal and Iaccarino (2005) for a sharp representation of immersed boundaries was later extended to finite-volume-based cut-cell methods by Örley et al. (2015), and is adopted in the present work.

The identification of ghost points and the extension of the solution into the solid region do not require a fully resolved cut-cell geometry. Accordingly, this procedure is carried out using the average face centroid and the cut-cell normal vector $\boldsymbol{n}_{\text{avg}}$, defined as the area-weighted average of the normals of all constituent cut elements. First, ghost-cells $\boldsymbol{X}_{GP}$ that contribute to the interpolation stencil are identified, as illustrated in Figure 2.2. Next, for each ghost-cell, the boundary intercept point $\boldsymbol{X}_{BI}$ is determined such that the line segment $\overline{\boldsymbol{X}_{GP}\boldsymbol{X}_{BI}}$ intersects the immersed boundary at $\boldsymbol{X}_{BI}$ along the local normal

direction of the interface segment. The line segment is then extended into the fluid region to locate the corresponding image point,

$$\boldsymbol{X}_{IP} = \boldsymbol{X}_{BI} + \boldsymbol{n}_{avg} \cdot \Delta l, \tag{2.45}$$

where $\Delta l = \|\boldsymbol{X}_{BI} - \boldsymbol{X}_{GP}\|$ denotes the distance between the ghost-cell and the boundary intercept.

Once the image point is located, a trilinear interpolation is employed to evaluate the value of a generic quantity ϕ_{IP} at $\boldsymbol{X}_{IP}$. For Dirichlet boundary conditions, the ghost-cell value is obtained as

$$\phi_{GP} = 2 \cdot \phi_{BI} - \phi_{IP} + \mathcal{O}(\Delta l^2), \tag{2.46}$$

whereas Neumann boundary conditions are imposed as

$$\phi_{GP} = \phi_{IP} - 2 \cdot \Delta l \left.\frac{\partial \phi}{\partial n}\right|_{\boldsymbol{X}_{BI}} + \mathcal{O}(\Delta l^2). \tag{2.47}$$

2.2. ANALYSIS METHODS

2.2.1. INTRINSIC AVERAGING

When quantifying spanwise-averaged flow characteristics in simulations involving spanwise-heterogeneous roughness, intrinsic averaging is adopted as a fundamental statistical operation in the post-processing of mean quantities. Unlike flows over spanwise-homogeneous surfaces, spanwise averaging in this context cannot be treated as a simple ensemble average. Instead, the contribution of each cut-cell must be weighted by its corresponding fluid volume fraction:

$$\langle \phi \rangle_{i_0,j_0} = \frac{\sum_{k=1}^{k=K} \langle \phi \rangle_{i_0,j_0,k} \alpha_{i_0,j_0,k} V_{i_0,j_0,k}}{\sum_{k=1}^{k=K} \alpha_{i_0,j_0,k} V_{i_0,j_0,k}}. \tag{2.48}$$

where $\langle \phi \rangle$ is a general variable, α and V are the volume fraction and corresponding volume of a cut cell. i, j, k are the indices of cells in the streamwise, wall-normal and spanwise directions.

2.2.2. SPECTRAL ANALYSIS

Spectral analysis is necessary when we study the unsteady flow phenomena, like STBLI. The signals of interest, such as the wall-pressure or shock motions, are inherently unsteady and broadband. Power spectral density (PSD), denoted by $\mathcal{P}$,

$$P = \int_{-\infty}^{\infty} \mathcal{P}(f)\, \mathrm{d}f \tag{2.49}$$

quantifies how the power of a signal is distributed across different frequencies, where P is the total power of the signal. Rather than describing the signal in the time domain, the PSD provides a frequency-domain representation, indicating which frequency components contain the dominant energy. The PSD can be computed via the Wiener-Khinchin

theorem, which states that $\mathcal{P}$ is the Fourier transform of the autocorrelation function $R_x(\tau)$:

$$\mathcal{P}(f) = \int_{-\infty}^{\infty} R_x(\tau)\, e^{-j2\pi f\tau}\, \mathrm{d}\tau \tag{2.50}$$

where the autocorrelation function is defined as:

$$R_x(\tau) = \lim_{T\to\infty} \frac{1}{T} \int_{-T/2}^{T/2} x(t)\, x^*(t-\tau)\, \mathrm{d}t. \tag{2.51}$$

Here $x(t)$ denotes the signal of interest, such as the wall pressure signals, and τ is the time delay.

While a conventional fast Fourier transform (FFT) yields high frequency resolution, its spectral estimate exhibits large variance and poor convergence. By dividing the signal into overlapping segments and averaging the periodograms of each segment, Welch's method significantly reduces the variance of the spectral estimate, leading to smoother and more repeatable spectra (Welch, 1967). This property is particularly important for STBLI, where the low-frequency unsteadiness of the separation shock is broadband and stochastic in nature.

In the following spectral analysis of the wall-pressure, separation-bubble volume, and shock-location signals, the Welch method combined with a Hann window is employed to estimate the PSD. The implementation procedure is summarized as follows:

- Each time signal is divided into eight segments of equal length, with an overlap ratio of 50% between adjacent segments.
- A Hann window is applied to each segment prior to spectral transformation by gradually reducing the signal to near zero at the edges of each segment, in order to mitigate spectral leakage arising from finite-length truncation.
- A FFT is performed on each windowed segment, and the corresponding periodogram is computed.
- The spectra obtained from all segments are subsequently ensemble-averaged to yield the final PSD estimate.

2.2.3. DYNAMIC MODE DECOMPOSITION

Dynamic mode decomposition (DMD) is a data-driven modal decomposition technique that aims to extract coherent spatial-temporal structures from a sequence of time-resolved data by approximating the underlying linear evolution operator. Each DMD mode is associated with a single growth/decay rate and frequency, enabling the identification of the dominant coherent structures that govern the system dynamics. It was proposed by Schmid (2010) and has been applied widely to a variety of flow problems, including jet flow, vortex identification, unsteadiness of STBLI and many others (Schmid, 2022; Zhang et al., 2014; Laguarda et al., 2024b; Hu, 2020).

Considering a sequence of snapshots:

$$\mathbf{x}_1, \mathbf{x}_2, \ldots, \mathbf{x}_m, \qquad \mathbf{x}_k \in \mathbb{R}^n. \tag{2.52}$$

The snapshots can be arranged into two data matrices:

$$\mathbf{X} = [\mathbf{x}_1\ \mathbf{x}_2\ \cdots\ \mathbf{x}_{m-1}], \qquad \mathbf{Y} = [\mathbf{x}_2\ \mathbf{x}_3\ \cdots\ \mathbf{x}_m], \tag{2.53}$$

and assume a best-fit linear mapping advancing the system by one time step:

$$\mathbf{Y} \approx \mathbf{A}\mathbf{X}, \tag{2.54}$$

In the least-squares sense, the operator can be written as

$$\mathbf{A} \approx \mathbf{Y}\mathbf{X}^{+}, \tag{2.55}$$

where $(\cdot)^{+}$ denotes the Moore–Penrose pseudoinverse. However, explicitly forming the full matrix $\mathbf{A} \in \mathbb{R}^{(n-1)\times(n-1)}$ is intractable due to its large dimensionality and is unnecessary, since only its eigenvalues and eigenmodes are of interest.

To avoid explicitly forming $\mathbf{A}$, Schmid proposed a more robust implementation in which a low-dimensional surrogate matrix $\tilde{\mathbf{A}}$ is constructed, from which the DMD eigenvalues and modes can be efficiently approximated (Schmid, 2010). A truncated singular value decomposition (SVD) of $\mathbf{X}$ is performed,

$$\mathbf{X} \approx \mathbf{U}\mathbf{\Sigma}\mathbf{V}^{T}, \tag{2.56}$$

where $\mathbf{U} \in \mathbb{C}^{(m-1)\times r}$, $\mathbf{V} \in \mathbb{C}^{r\times r}$, $\mathbf{\Sigma} \in \mathbb{C}^{(m-1)\times r}$ ($r \le (m-1)$ indicates optional truncation), leading to the reduced operator

$$\tilde{\mathbf{A}} = \mathbf{U}^{T}\mathbf{A}\mathbf{U} = \mathbf{U}^{T}\mathbf{Y}\mathbf{V}\mathbf{\Sigma}^{-1} \in \mathbb{R}^{r\times r}. \tag{2.57}$$

The eigen-decomposition

$$\tilde{\mathbf{A}}\tilde{\phi}_j = \mu_j\tilde{\phi}_j \tag{2.58}$$

yields the DMD eigenvalues μ_j and eigenvectors $\tilde{\phi}_j$. The following transformation can be used to map the eigenvectors in the subspace back to physical space

$$\phi_j = \mathbf{Y}\mathbf{V}\mathbf{\Sigma}^{-1}\tilde{\phi}_j. \tag{2.59}$$

The growth rate β_j and angular frequency ω_j of each DMD mode can be directly obtained from the corresponding eigenvalue μ_j:

$$\mu_j = |\mu_j|e^{i\theta_j} \equiv e^{(\beta_j + i\omega_j)\Delta t}, \tag{2.60}$$

where $\theta_j = \arg(\mu_j)$, $\beta_j = \ln|\mu_j|/\Delta t$ and $\omega_j = \theta/\Delta t$.

Based on the above decomposition, the snapshots data can be approximately represented by a linear combination of the DMD modes:

$$\mathbf{X} \approx \underbrace{\begin{bmatrix}\phi_1 & \phi 2 & \dots & \phi_{m-1}\end{bmatrix}}_{\mathbf{\Phi}} \underbrace{\begin{bmatrix}\alpha_1 & & & \\ & \alpha_2 & & \\ & & \dots & \\ & & & \alpha_{m-1}\end{bmatrix}}_{\mathbf{D}_\alpha = \mathrm{diag}\{\alpha\}} \underbrace{\begin{bmatrix}1 & \mu_1 & \dots & \mu_1^{m-2} \\ 1 & \mu_2 & \dots & \mu_2^{m-2} \\ \vdots & \vdots & \ddots & \vdots \\ 1 & \mu_{m-1} & \dots & \mu_{m-1}^{m-2}\end{bmatrix}}_{\mathbf{V}_{and}} \tag{2.61}$$

where Vandermonde matrix $\mathbf{V}_{and} \in \mathbb{C}^{(m-1)\times(m-1)}$. The computation of the unknown amplitudes vector $\boldsymbol{\alpha} := [\alpha_1 ... \alpha_{m-1}]$ is an optimization problem formulated by:

$$\underset{\alpha}{\text{minimize}} \|\mathbf{X} - \boldsymbol{\Phi}\mathbf{D}_{\alpha}\mathbf{V}_{and}\|_F^2 \tag{2.62}$$

For analysis and physical interpretation, a further reduction of the number of modes is helpful. For this purpose, Jovanović et al. (2014) introduced the sparsity-promoting dynamic decomposition method (SPDMD), which is based on regularizing the least-squares deviation in Eq. (2.62) with an additional term that penalizes the ℓ_1-norm of the amplitude vector $\boldsymbol{\alpha}$:

$$\underset{\alpha}{\text{minimize}} \left(\|\mathbf{X} - \boldsymbol{\Phi}\mathbf{D}_{\alpha}\mathbf{V}_{and}\|_F^2 + \gamma \sum_{j=0}^{m-1} |\alpha_j| \right), \tag{2.63}$$

where γ is a regularization parameter that determines the sparsity. The alternating direction method of multipliers was provided by Jovanović to solve the convex optimization problem of Eq. (2.63). The readers are referred to their publication for more algorithmic details (Jovanović et al., 2014).

3

Convergent-Divergent Riblets

风起于青萍之末。
The wind rises from the ends of the green duckweed leaves.
《风赋》 / *Ode to the Wind*

As introduced in Chapter 1, convergent–divergent (C–D) riblets are capable of inducing strong secondary flows, thus enhancing the momentum transfer in the boundary layer, similar to micro-vortex generators (MVGs), but with a much smaller protrusion into the high-speed flow. This feature suggests their potential for reducing parasitic drag, particularly in high-speed flow applications. Previously, Guo et al. (2022a) applied C–D riblets to the control of a compression-corner STBLI using direct numerical simulation (DNS) and demonstrated a substantial reduction in the separation region. Wen et al. (2024) conducted experimental investigations on an impinging STBLI and similarly observed a corrugated separation line accompanied by an overall reduction in separation extent. Despite these encouraging findings, high-fidelity numerical simulations assessing the control effects of C–D riblets on impinging STBLIs are still lacking in the published literature.

This chapter, therefore, investigates the control effects of C–D riblets on an impinging STBLI using wall-resolved LES, with particular emphasis on their influence on upstream turbulent boundary-layer properties, the extent of flow separation, and the resulting unsteady pressure loads.

3.1. FLOW CONFIGURATION AND NUMERICAL SETUPS

3.1.1. FLOW CONFIGURATION

We investigate the interaction between an impinging shock and an incoming turbulent boundary layer, as illustrated in Figure 3.1. Three simulations are considered: a baseline smooth-wall case ($\mathcal{S}$) and two controlled cases employing C–D riblet patches of different heights (denoted as $\mathcal{CD}1$ and $\mathcal{CD}2$).

All simulations share identical inflow conditions, consisting of a Mach 2.0 turbulent boundary layer interacting with an oblique impinging shock wave at a shock angle of $\phi = 40.04°$. The computational domain for the baseline smooth-wall case $\mathcal{S}$ has dimensions $L_x \times L_y \times L_z = 45.4\delta_0 \times 16.5\delta_0 \times 4\delta_0$, where δ_0 denotes the 99% boundary-layer thickness at the inflow plane. The nominal shock impingement point, x_{imp}, is located $32\delta_0$ downstream of the inflow plane.

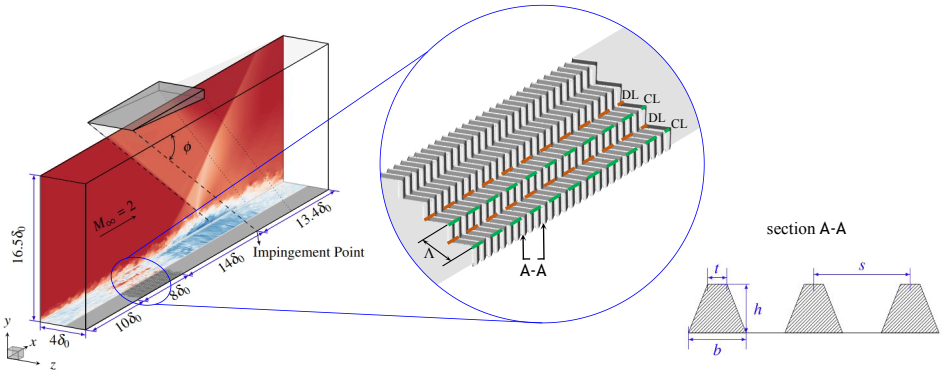

Figure 3.1: Schematic of the computational domain of a Mach 2.0 STBLI over C-D riblets.

M_∞	T_0 [K]	p_0 [kPa]	δ_0 [mm]	δ_{imp} [mm]	$Re_{\tau,0}$	$Re_{\tau,imp}$	Re_{δ_0}	ϕ
2.0	288.2	355.6	5.2	7.7	250	355	11.6×10^3	40.04°

Table 3.1: Summary of flow parameters adopted in current research. $Re_{\tau,0}$ is evaluated at the inlet, and $Re_{\tau,imp}$ at the impingement point.

The fluid is modeled as a perfect gas with standard air properties. The inlet stagnation temperature and pressure are $T_0 = 288.2$ K and $p_0 = 355.6$ kPa, respectively. The Reynolds numbers $Re_{\delta_0} = \rho_\infty u_\infty \delta_0 / \mu_\infty$ is 11.6×10^3 at the inlet of the computational domain, where ρ_∞, u_∞, μ_∞ are density, velocity and dynamic viscosity of the free stream flow. The corresponding friction Reynolds number $Re_{\tau,0} = \delta_0 / \delta_\nu$ is 250 at the inlet. The viscous length scale $\delta_\nu = \mu_w / (\rho_w u_\tau)$ is computed with the parameters at the wall, with $u_\tau = \sqrt{\tau_w / \rho_w}$ being the friction velocity, and τ_w and ρ_w are the stress per plane area and the density of the fluid at the wall. In the absence of the impinging shock and expansion fan, the 99% boundary layer thickness at the inviscid impingement point, which is located $32\delta_0$ downstream of the inlet, is $\delta_{imp} = 1.48\delta_0$ and the corresponding friction Reynolds number is $Re_{\tau,imp} = 355$. The relevant flow parameters are summarized in Table 3.1.

3.1.2. RIBLETS POSITION AND GEOMETRY

For cases $\mathcal{CD}1$ and $\mathcal{CD}2$, a riblet patch is introduced $10\delta_0$ downstream of the computation domain inlet to ensure that the incoming turbulence has reached a statistically developed state (Laguarda and Hickel, 2024a). The riblet patch terminates $14\delta_0$ upstream of the nominal shock impingement point, spanning the region $(x - x_{imp})/\delta_0 = -22$ to -14. The riblets are positioned such that the entire interaction region develops downstream of the riblets, thereby eliminating any direct geometric influence of the riblets on the interaction. Consequently, the effect of riblet-induced vortices on the STBLI can be isolated. The patch extends over a streamwise length of $8\delta_0$, which allows the secondary flow to fully develop before interacting with the shock.

Regarding the riblet geometry, the riblets are sunken (recessed) into the wall surface. The riblet patch spans the entire spanwise extent of the domain. The spanwise width Λ between two adjacent convergent lines (CLs) or divergent lines (DLs) is $1.0\delta_0$, as illustrated in Figure 3.1. The yaw angle γ of riblets, defined as the acute angle between the riblet passage and the streamwise direction, is set to 45°. This combination of geometric parameters has been shown to produce the strongest secondary flows (Guo et al., 2022d; Guo et al., 2020). The riblets have a trapezoidal cross-section, characterized by a top width $t = 0.04\delta_0$ and a base width $b = 0.12\delta_0$, with a spacing of $s = 0.2\delta_0$ between adjacent riblets, see Figure 3.1. In inner scaling, these parameters correspond to $t^+ = t/\delta_\nu = 9.8$, $b^+ = b/\delta_\nu = 29.5$, and $s^+ = s/\delta_\nu = 49.2$, respectively. The riblet height differs between the two cases: $h = 0.03\delta_0$ ($h^+ = h/\delta_\nu = 7.4$) for $\mathcal{CD}1$, and $h = 0.10\delta_0$ ($h^+ = 24.6$) for $\mathcal{CD}2$. A summary of the geometric parameters is provided in Table 3.2.

3.1.3. BOUNDARY CONDITIONS AND GRID DISTRIBUTION

The bottom wall is modeled using an adiabatic no-slip boundary condition in all cases. At the inflow plane, the digital-filter method described in Section 2.1.4 is employed to

	Λ/δ_0	γ	t/δ_0	b/δ_0	s/δ_0	h/δ_0	t^+	b^+	s^+	h^+
$\mathcal{CD}1$	1.0	45°	0.04	0.12	0.2	0.03	9.8	29.5	49.2	7.4
$\mathcal{CD}2$	1.0	45°	0.04	0.12	0.2	0.10	9.8	29.5	49.2	24.6

Table 3.2: Geometric parameters for C-D riblets. For the corresponding definitions, see Fig. 3.1.

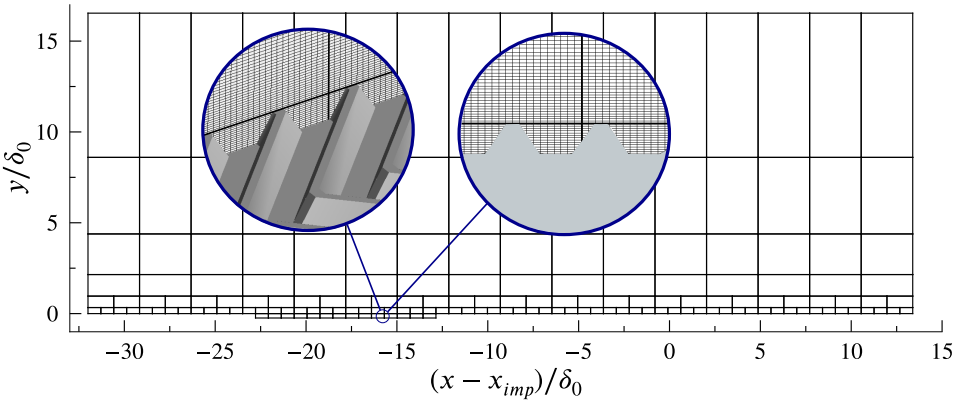

Figure 3.2: Schematic of the block distribution of the numerical grid and enlarged views of the near-wall mesh for case $\mathcal{CD}2$. The left panel presents a three-dimensional perspective view of the mesh, while the right panel shows an x–y cross-sectional view.

generate a synthetic turbulent inflow with prescribed spatial and temporal correlations. At the top boundary, a non-reflecting boundary condition based on Riemann invariants is applied; the oblique shock and the trailing-edge expansion fan are introduced using the Rankine–Hugoniot relations and Prandtl–Meyer theory (Poinsot and Lele, 1992), respectively. Periodic boundary conditions are imposed in the spanwise direction.

The computational domain is discretized using a block-structured Cartesian grid with an equal number of cells per block but varying grid spacing. For the smooth wall baseline case, the Cartesian grid consists of $N_x \times N_y \times N_z = 512 \times 192 \times 128 = 12.6 \times 10^6$ cells. The grid resolution in the wall units is $\Delta x^+ = 21.9$ and $\Delta z^+ = 7.74$, with $\Delta y^+_{wall} \leq 0.93$. As depicted in Figure 3.2, the mesh is gradually coarsened with increasing distance from the wall, and a mild stretching is applied in the wall-normal direction using a constant stretching factor of 1.02. The riblets are sunken into the wall surface; accordingly, an additional layer of blocks is introduced to accommodate the immersed riblet geometry. The mesh is further refined in the streamwise and spanwise directions, yielding grid resolutions of $\Delta x^+ = 5.49$, $\Delta z^+ = 3.87$, and $\Delta y^+_{\text{wall}} \leq 0.93$. This resolution is considerably finer than that typically employed in LES, resulting in a total of 45.6×10^6 grid cells for both riblet cases.

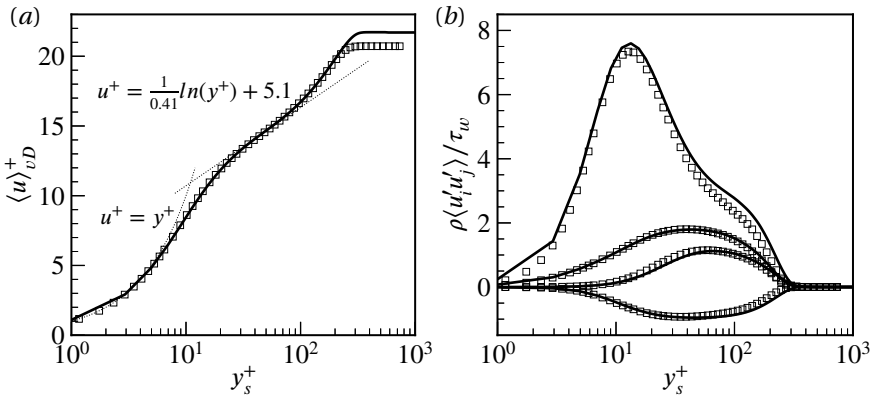

Figure 3.3: Comparison of present LES (—) for the smooth wall case and DNS (□) of Pirozzoli and Bernardini (2011); (a) van Driest transformed mean velocity profiles and (b) density scaled Reynolds stresses. Note: LES results are taken from $(x - x_{imp})/\delta_0 = -20.0$, where $Re_\tau = 285$, and DNS data is at $Re_\tau = 250$.

3.1.4. OTHER NUMERICAL SETUP

All simulations were initialized using the inviscid shock reflection solution. After an initial transient period of approximately 2000 δ_0/u_∞, all cases were integrated for more than 4000 δ_0/u_∞ to obtain converged statistics for the low-frequency dynamics of STBLI. Flow statistics were computed by time-averaging the instantaneous three-dimensional solutions. Two arrays of numerical probes were placed at the DL and CL, with a sampling rate of $f_s \approx 46 u_\infty/\delta_0$. Additionally, instantaneous three-dimensional snapshots of the interaction region were saved at intervals of $\Delta t \approx \delta/u_\infty$ for post-processing, yielding an ensemble of approximately 4100 snapshots per case.

3.2. RESULTS AND DISCUSSIONS

3.2.1. BASELINE TURBULENT BOUNDARY LAYER

Before discussing the effects of C-D riblets on STBLI, the baseline smooth-wall LES results are first compared with available DNS data to assess the capability of the present solver in capturing the key flow features of the incoming turbulent boundary layer. Figure 3.3(a) presents the van Driest–transformed mean velocity profile of the smooth-wall case at a streamwise location $20\delta_0$ upstream of the shock impingement point. At this station, the flow is unaffected by the interaction, while being sufficiently downstream of the inflow plane ($12\delta_0$) to allow the turbulence generated by the digital filter to reach a fully developed natural state (Laguarda and Hickel, 2024a). The velocity profile agrees well with the classic law of the wall. Reference DNS data of a Ma 2.0 TBL from Pirozzoli Pirozzoli and Bernardini (2011) is also included in the figure and is in good agreement with the LES data, confirming the accuracy of the incoming turbulent boundary layer. Note that the LES has a slightly higher friction Reynolds number ($Re_\tau = 285$ at this station) than the DNS case ($Re_\tau = 250$), which is correctly represented by higher $\langle u \rangle^+_{vD}$ in the wake region. The density-scaled Reynolds stresses are shown in Figure 3.3(b) and further highlight the very good agreement between the baseline LES and DNS results for a smooth wall.

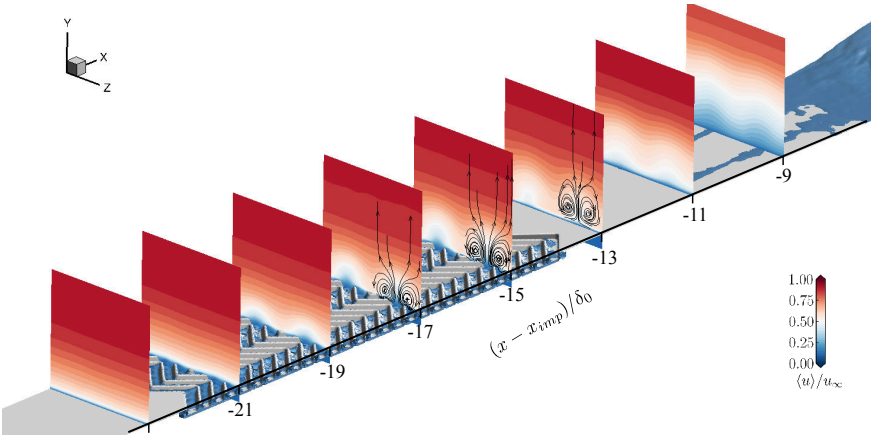

Figure 3.4: Cross-stream slices of the streamwise velocity field for case $\mathcal{CD}2$. The slices are taken at streamwise locations ranging from $(x - x_{imp})/\delta_0 = -23$ to -9, with a spacing of $2\delta_0$. The isosurface indicates the location where $\langle u \rangle = 0$.

Small differences near the boundary-layer edge can be attributed to the difference in Reynolds number. Further validations of the current baseline case could be found in the recent work of Laguarda et al. (2024b), where detailed comparisons against experimental data were performed. The predicted wall-pressure distributions, skin-friction evolution, interaction scales, intermittency, and flow organization were shown to agree well with available experimental measurements.

3.2.2. TURBULENT BOUNDARY LAYER MODULATION BY RIBLETS

As expected, the interaction of the incoming turbulent boundary layer with the C-D riblet patch induces secondary flows within the boundary layer. The imposed yaw angle of the riblets guides the near-wall flow from the divergent line (DL) toward the convergent line (CL), introducing a systematic spanwise motion (Guo et al., 2022c). As a result, the induced secondary flow exhibits a downwash motion over the DLs and an upwash motion over the CLs, forming pairs of counter-rotating vortices.

Figure 3.4 presents cross-stream slices of the streamwise velocity field for case $\mathcal{CD}2$. A pair of induced vortices can be clearly identified, which gradually develop in the streamwise direction.

The global strength of the secondary flow can be quantified using the metric introduced by Guo et al. (2022c), defined as

$$I = \frac{1}{A}\int_A \frac{\sqrt{\langle v \rangle^2 + \langle w \rangle^2}}{u_\infty} \mathrm{d}y\mathrm{d}z\,, \tag{3.1}$$

where A denotes the integration area from the wall to the local boundary layer thickness over the cross-stream plane. To further assess the effect of riblets on the secondary flow, additional simulations without shock impingement are considered. These cases correspond to turbulent boundary layers developing over the same riblet configurations, in the absence of an impinging shock and expansion fan. Figure 3.5 shows the streamwise

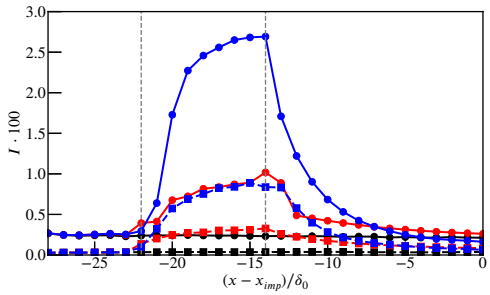

Figure 3.5: Streamwise evolution of the secondary-flow intensity I over the riblet patch without shock impingement for the baseline $\mathcal{S}$ in black, case $\mathcal{CD}1$ in red and $\mathcal{CD}2$ in blue. The lines with circle markers are computed using both $\langle v \rangle$ and $\langle w \rangle$, while the lines with square markers include only the induced spanwise velocity $\langle w \rangle$. The gray dash lines show the riblets patch region.

evolution of this intensity over the smooth-wall and riblet patch (lines with circle markers) for all cases. Owing to the inherently non-zero wall-normal velocity in a turbulent boundary layer, the intensity I exhibits a finite value upstream of the riblet patch. To isolate the contribution of the riblet-induced secondary motion, an alternative definition of the intensity is considered, in which only the induced spanwise velocity $\langle w \rangle$ is retained in Eq. 3.1. The resulting intensity is shown by the lines with square markers. For both definitions, the baseline remains nearly constant, as expected. In contrast, for the riblet cases,the secondary flow intensifies rapidly over the first half of the riblet patch, followed by a substantially reduced growth rate and saturation, suggesting that the riblet patch length is sufficient for the secondary flow to reach a developed state. It is also observed that the maximum intensity in $\mathcal{CD}2$ is approximately three times that in $\mathcal{CD}1$, roughly scaling with the riblet height. After passing over the riblets, the secondary flow intensity defined by both measures decays rapidly downstream. This suggests that the modulation induced by the riblets is spatially localized, and its effectiveness is likely sensitive to the relative positioning between the riblets and the shock impingement location.

The mean flow structures of a cross-section at $(x - x_{imp})/\delta_0 = -15$ are shown in Figure 3.6. For the controlled cases, the induced secondary-flow structure is clearly observed: low-momentum fluid is lifted away from the wall over CL, leading to a significant enlargement of the subsonic region within the boundary layer. In the channels between adjacent riblets, strong spanwise flows $\langle w \rangle$ from DL to CL are observed, exceeding 20% of u_∞. This consistent with the conclusion of Guo et al. (2020) that the large-scale secondary flow is driven by the spanwise velocity generated by the yawed riblet passages.

Pronounced turbulent kinetic energy (TKE) amplification is observed over the CL in the controlled cases, as shown in the last row of Figure 3.6. This phenomenon is primarily associated with the sustained upwash induced by the secondary flow, which lifts near-wall, turbulence-rich, low-momentum fluid into regions of strong mean shear, thereby significantly enhancing the turbulence production. Moreover, the intensity of the induced secondary flow is strongly correlated with the riblet height: $\mathcal{CD}2$, with a height of $0.1\delta_0$, exhibits substantially larger velocity magnitudes—and correspondingly stronger upwash and TKE enhancement—than $\mathcal{CD}1$, whose height is only $0.03\delta_0$.

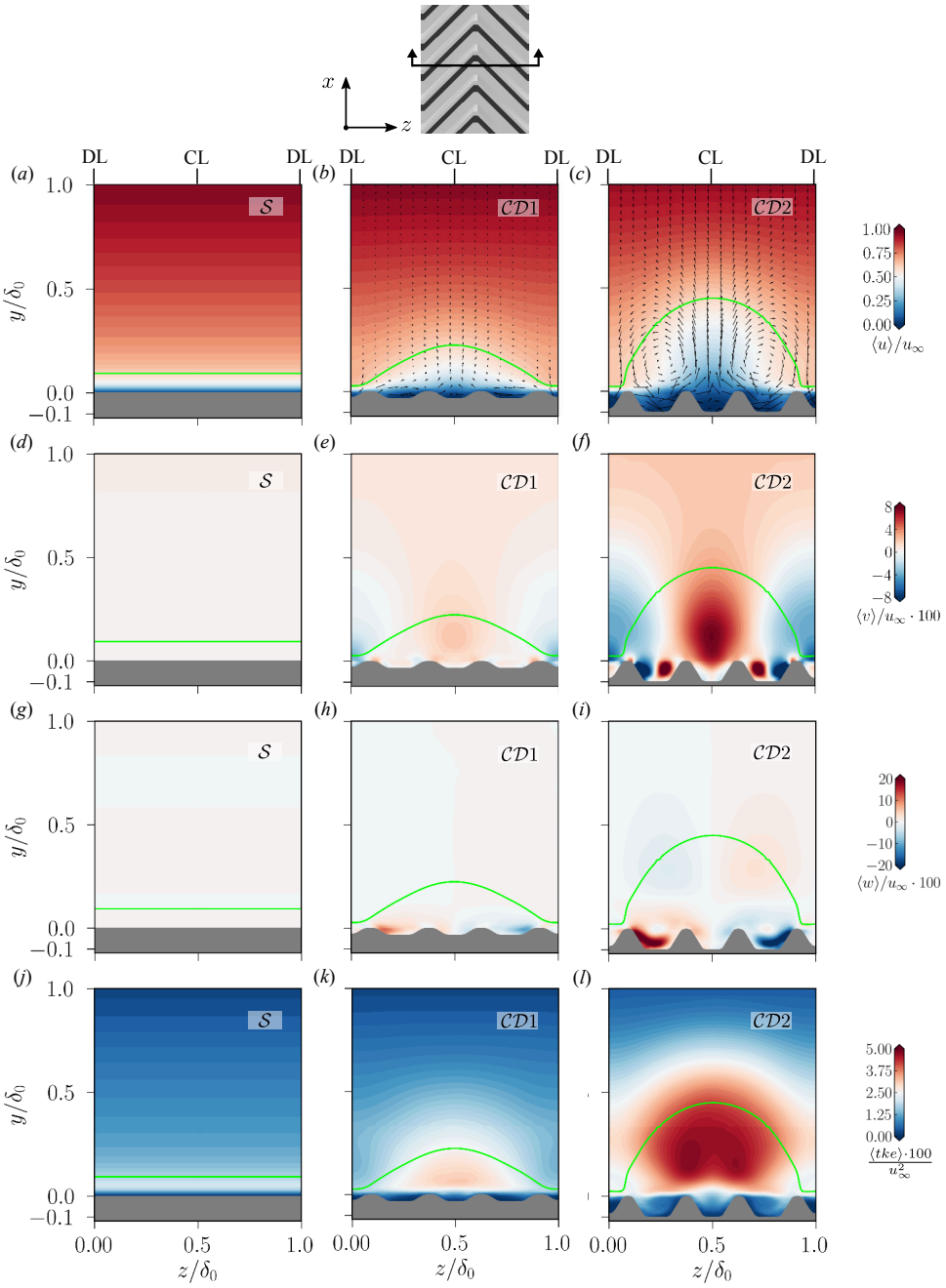

Figure 3.6: Mean flow (a, b, c) streamwise velocity, (d, e, f) wall-normal velocity, (g, h, i) spanwise velocity, (f, k, l) turbulent kinetic energy distribution in a cross-stream plane at $(x - x_{imp})/\delta_0 = -15$. The sonic line is shown in lime. The locations of divergent and convergent lines are indicated on top of the first row.

A station located downstream of the riblets at $(x - x_{imp})/\delta_0 = -13.0$ is also selected to examine the characteristics of the turbulent boundary layer right before the interaction, as shown in Figure 3.7. Compared with the secondary flow in Figure 3.6, the flow topology is qualitatively similar but the intensity of the secondary flow has decayed quickly. The enlarged subsonic region in the riblet cases implies an increased susceptibility of the boundary layer to upstream influence from downstream perturbations. In contrast, for the smooth-wall case, the subsonic region remains confined close to the wall. The wall-normal velocity distributions further indicate that, in addition to the upwash over the CL, a downwash occurs over DL, which slightly compresses the height of the local subsonic region.

The mean streamwise and wall-normal velocity profiles from all the cases at $(x - x_{imp})/\delta_0 = -13$ are shown in Figure 3.8. For the two riblet cases, the spanwise-averaged mean streamwise velocity profiles are generally less full than that of case $\mathcal{S}$, indicating a reduced ability to resist flow separation on average. However, owing to the presence of the induced secondary flow, pronounced spanwise heterogeneity is observed between the DLs and CLs. Specifically, the streamwise velocity profiles at the DLs are noticeably fuller than those at the CLs, and are even fuller than the smooth-wall profile in the near-wall region, suggesting that the downwash locally energizes the turbulent boundary layer at the DLs.

The wall-normal velocity profiles in Figure 3.8(b) further show that the induced upwash over the CLs is stronger than the downwash over the DLs in both $\mathcal{CD}1$ and $\mathcal{CD}2$. This spanwise modulation of the mean velocity profiles is consistent with the secondary-flow-induced redistribution of momentum, with downwash at the DLs enhancing near-wall momentum and upwash at the CLs lifting low-momentum fluid away from the wall.

Table 3.3 summarizes several key quantitative metrics characterizing the baseline and controlled cases, including the shape factor H, the spanwise-averaged height of the subsonic region $h_{\text{sonic}}/\delta_0$, the maximum wall-normal velocity, and the secondary-flow intensity I. Compared with the smooth-wall case $\mathcal{S}$, both controlled cases exhibit increased shape factors and a pronounced enlargement of the subsonic region, consistent with the lift-up of low-momentum fluid induced by the secondary flow. Moreover, the substantially larger values of $\langle v \rangle_{\max}$ and I in $\mathcal{CD}2$ further confirm the stronger secondary flow associated with the larger riblet height.

The riblet patch inevitably introduces additional pressure drag compared with the smooth baseline. With the present setup, the pressure contribution accounts for approximately 17% of the total drag for $\mathcal{CD}1$, increasing to about 41% for $\mathcal{CD}2$. Equivalently, the pressure drag is approximately 20% and 70% of the friction drag for $\mathcal{CD}1$ and $\mathcal{CD}2$, respectively, indicating an approximate scaling with the riblet height.

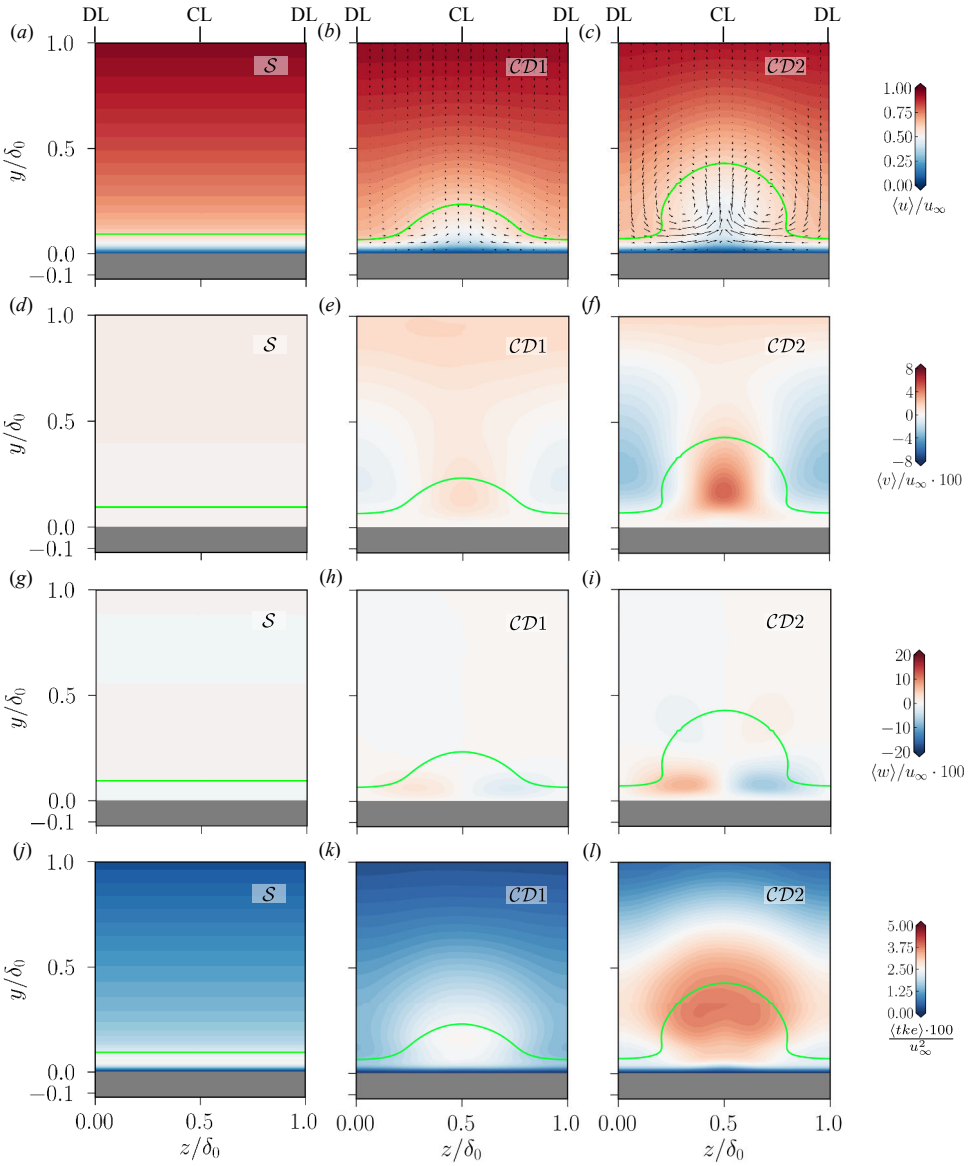

Figure 3.7: Mean flow (a, b, c) streamwise velocity, (d, e, f) wall-normal velocity, (g, h, i) spanwise velocity, (f, k, l) turbulent kinetic energy distribution in a cross-stream plane at $(x - x_{imp})/\delta_0 = -13$. The sonic line is shown in lime. The locations of divergent and convergent lines are indicated on top of the first row.

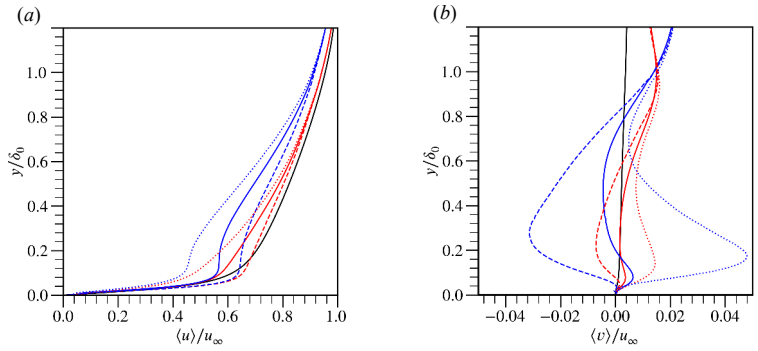

Figure 3.8: Profiles of the mean (a) streamwise velocity and (b) wall-normal velocity at $(x - x_{imp})/\delta_0 = -13$. The black solid line corresponds to case $\mathcal{S}$, the red lines to case $\mathcal{CD}1$, and the blue lines to case $\mathcal{CD}2$. For the riblet cases, solid lines denote spanwise-averaged profiles, dashed lines indicate profiles at the divergent lines (DLs), and dotted lines represent profiles at the convergent lines (CLs).

Case	H	h_{sonic}/δ_0	$\langle v \rangle_{max}/u_\infty$	I
$\mathcal{S}$	3.02	0.096	–	0
$\mathcal{CD}1$	3.17	0.143	1.31%	0.0090
$\mathcal{CD}2$	3.61	0.251	4.16%	0.0166

Table 3.3: Summary of the shape factor H, spanwise-averaged height of subsonic region, maximum wall-normal velocity, and vorticity intensity I of the baseline and controlled cases at $(x - x_{imp})/\delta_0 = -13$.

3.2.3. INTERACTION REGION

Time-averaged pressure fluctuation distributions at DL and CL are shown in Figure 3.9. The shock system, sonic lines, and zero streamwise velocity lines are superimposed on the contours to serve as a reference. Strong pressure fluctuations are observed at two locations: one near the impingement point of the oblique shock on the shear layer, and the other in the vicinity of the separation shock, particularly above the intersection between the impinging and separation shocks. The amplification of pressure fluctuations in these regions is primarily associated with the inherent unsteadiness of the separation bubble and the low-frequency oscillation of the separation shock (Wu et al., 2026). Compared with case $\mathcal{S}$, both riblet cases exhibit stronger pressure fluctuations near the former location, which can be attributed to the enhanced unsteadiness induced by the enlarged separation bubble. In addition, the riblet cases display noticeably larger interaction regions, as the onset of the interaction shifts upstream with increasing ridge height. Clear differences between the DLs and CLs are also evident. At the CLs, the increased height of the subsonic region facilitates upstream propagation of downstream disturbances, thereby enlarging the interaction region. In contrast, at the DLs, the upstream extent of the reversed-flow bubble is reduced, whereas an opposite trend is observed at the CLs in both riblet cases. It is noted, however, that the reversed-flow region remains very shallow in all cases, which is likely attributable to the relatively low Reynolds number (Laguarda et al., 2024b).

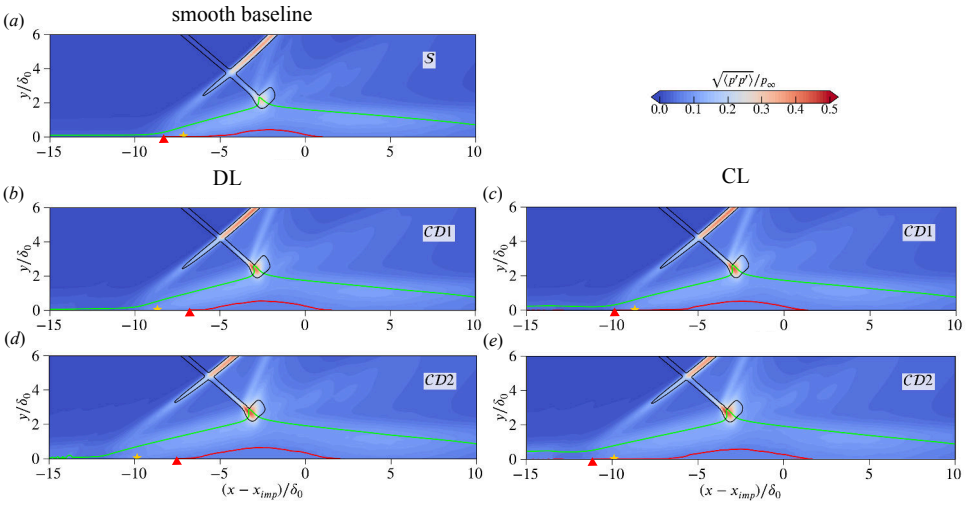

Figure 3.9: Time-averaged pressure fluctuation distributions on the (a,b,d) $z = 0$ plane, corresponding to the divergent line (DL), and on the (c,e) $z = 0.5\delta_0$ plane, corresponding to the convergent line (CL). The sonic line is indicated in lime, the zero streamwise velocity line in red, and the shock system (visualized by isolines of density gradient magnitude $|\nabla\rho|\delta_0/\rho_\infty = 0.79$) in black. The location of the peak wall-pressure fluctuation is marked by the yellow star, and the leading edge of separation is marked by the red triangle.

Time-averaged wall-surface variables along the streamwise direction are presented in Figure 3.10. The mean skin-friction coefficients shown in Figure 3.10(a) exhibit pronounced spanwise heterogeneity between the DLs and CLs for both riblet cases, with $\langle C_f \rangle$ at the CLs being consistently lower than that at the DLs. This spanwise difference gradually diminishes toward the middle of the separation bubble. Such a distribution indicates that the riblet-induced secondary flows tend to suppress separation at the DLs while promoting it at the CLs. From the spanwise-averaged perspective, the riblet cases show a slight upstream shift of the separation point compared with the smooth-wall case, whereas the downstream reattachment location is also displaced slightly downstream.

The wall-pressure distributions shown in Figure 3.10(b) indicate that the onset of the interaction region shifts upstream for both cases $\mathcal{CD}1$ and $\mathcal{CD}2$. Meanwhile, the peak wall-pressure downstream of the reattachment point is reduced compared with the smooth-wall case, implying a more gradual pressure rise across the interaction region. In Figure 3.10(c), it can be seen that the peak wall-pressure fluctuations near the separation shock foot are slightly attenuated in both riblet cases, and the magnitude of this reduction increases with riblet height. Relative to case $\mathcal{S}$, the peak reduction reaches 7.8% for $\mathcal{CD}1$ and 11.8% for $\mathcal{CD}2$. In addition, spanwise variations are observed near the fluctuation peak, with increased wall-pressure fluctuations at the DLs and reduced levels at the CLs compared with the spanwise averaged one. Figure 3.10(d) presents the streamwise distributions of the mean wall-pressure gradient, where a monotonic decrease in the peak value is observed as the riblet height increases. Similar to the wall-pressure distributions, no clear spanwise heterogeneity is evident in the wall-pressure gradient. The decrease in the wall-pressure gradient indicates a more smeared shock foot and partly explains the

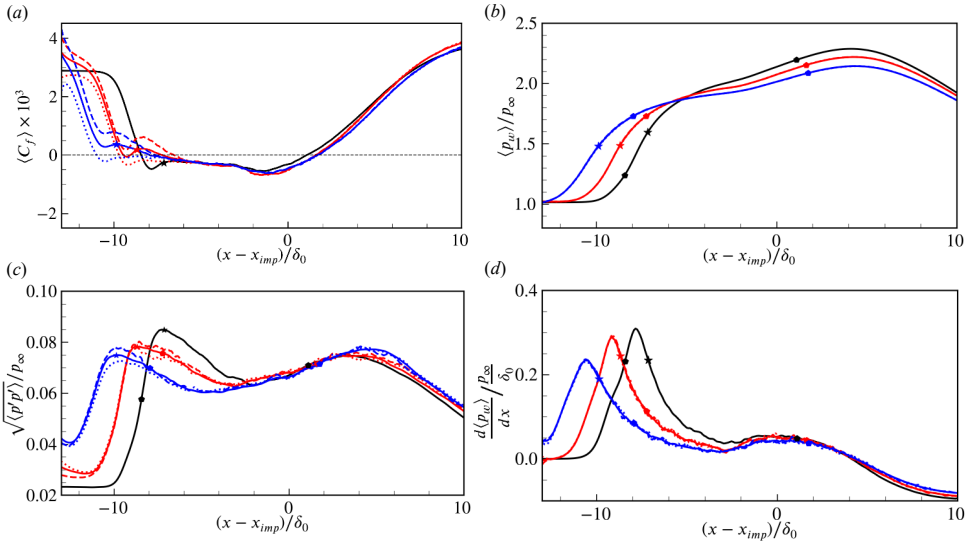

Figure 3.10: Streamwise distributions of time-averaged (a) skin friction coefficient, (b) wall-pressure, (c) wall-pressure fluctuation, and (d) wall-pressure gradient. The black solid line corresponds to the smooth-wall case $\mathcal{S}$, while the red and blue lines represent cases $\mathcal{CD}1$ and $\mathcal{CD}2$, respectively. For the riblet cases, solid lines denote spanwise-averaged profiles, dashed lines indicate profiles at the divergent lines (DLs), and dotted lines represent profiles at the convergent lines (CLs). Star markers indicate the locations of the maximum wall-pressure fluctuation, and pentagon markers denote the spanwise-averaged separation and reattachment points.

reduction of the wall-pressure fluctuation peak.

Figure 3.11 shows the time- and spanwise periodic-averaged distributions of the skin-friction coefficient, which clearly delineate the footprint and shape of the separation region downstream of the riblets. Compared with the smooth-wall case $\mathcal{S}$, the upstream portion of the separation region in the riblet cases becomes highly corrugated in the spanwise direction. Consistent with the trends observed in Figure 3.10(a), the DLs are characterized by locally increased $\langle C_f \rangle$ and delayed separation, owing to the energization of the near-wall flow by the riblet-induced downwash motions. In contrast, at the CLs, the induced upwash leads to reduced $\langle C_f \rangle$ and promotes earlier local separation. Compared with case $\mathcal{CD}1$, separation in case $\mathcal{CD}2$ is more strongly suppressed near the DLs; however, the overall separation region extends further upstream, indicating an enhanced spanwise modulation accompanied by a globally extended interaction.

The spatial distribution of the wall-pressure fluctuation, $\sqrt{\langle p'p' \rangle}/p_\infty$, is shown in Figure 3.12. Compared with the baseline case $\mathcal{S}$, both riblet cases exhibit elevated wall-pressure fluctuations upstream of the interaction region. In contrast, the peak fluctuation associated with the separation shock foot is reduced, with an attenuation observed as the ridge height increases. Moreover, the wall-pressure fluctuation displays clear spanwise heterogeneity, consistent with the trends reported in Figure 3.10(c). In particular, pressure fluctuations are noticeably alleviated at the CLs, whereas higher fluctuation levels persist near the DLs.

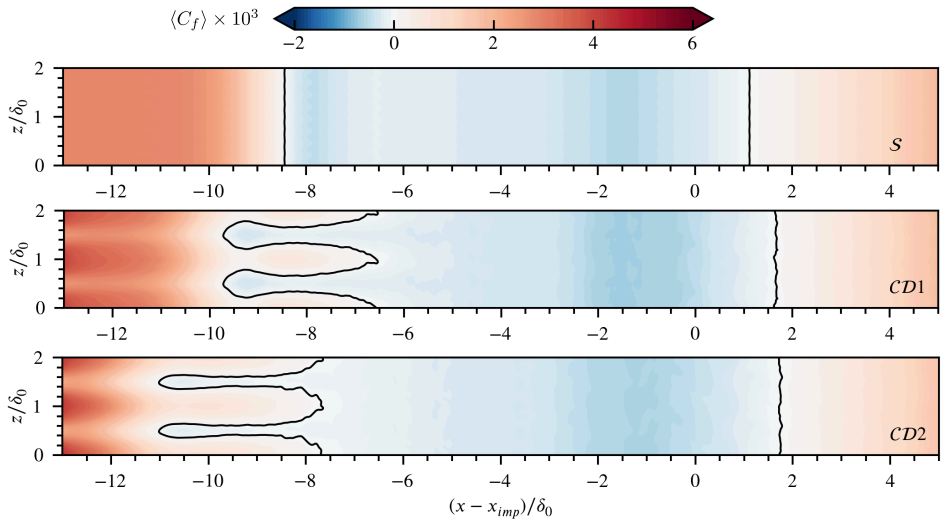

Figure 3.11: Time-averaged skin friction coefficient distribution downstream of riblets. Black lines denote the region of reverse-flow. DL is located at $z/\delta_0 = 0, 1, 2$, while CL is located at $z/\delta_0 = 0.5, 1.5$.

3.2.4. SPECTRAL ANALYSIS OF WALL-PRESSURE FLUCTUATION

To complement the spatial analysis, the frequency characteristics of the wall-pressure fluctuations are examined through spectral analysis. Wall-pressure signals are collected at $z = 0$ (DL) and $z/\delta_0 = 0.5$ (CL) for the riblet cases, whereas for the baseline case $\mathcal{S}$ only signals at $z = 0$ are considered, owing to the spanwise homogeneity of the wall-pressure fluctuation distribution.

As shown in Figure 3.13, a distinct low-frequency component with a characteristic frequency of $St_{L_{sep}} \approx 0.05$ is observed near the separation shock foot for all cases. This low-frequency content is more broadbanded and less localized in the streamwise direction and attenuated in the riblet cases, with the strongest reduction occurring in case $\mathcal{CD}2$. The location of the maximum wall-pressure fluctuation is consistently found slightly downstream of the low-frequency component. This offset arises because, at the considered Reynolds number, the total pressure fluctuation is dominated by high-frequency contributions (Wu et al., 2026), which originate from the amplification of turbulence within the separated shear layer and require a finite streamwise distance to develop downstream of the shock foot. A comparison between the DL and CL spectra for the riblet cases shows that the low-frequency component remains largely unchanged, whereas the high-frequency content is significantly attenuated at the CLs, particularly in case $\mathcal{CD}2$.

To clearly compare the relative contributions of the low- and high-frequency components to the reduction of wall-pressure fluctuations, the signals measured at the DL and CL are further examined. The wall-pressure fluctuation obtained by integrating the power spectral density is shown in Figure 3.14(a). For case $\mathcal{CD}2$, the wall-pressure fluctuations at the DL and CL, represented by the blue dashed and dotted lines respectively, are both lower than those of the baseline case $\mathcal{S}$. Moreover, near the peak region, the fluctuation

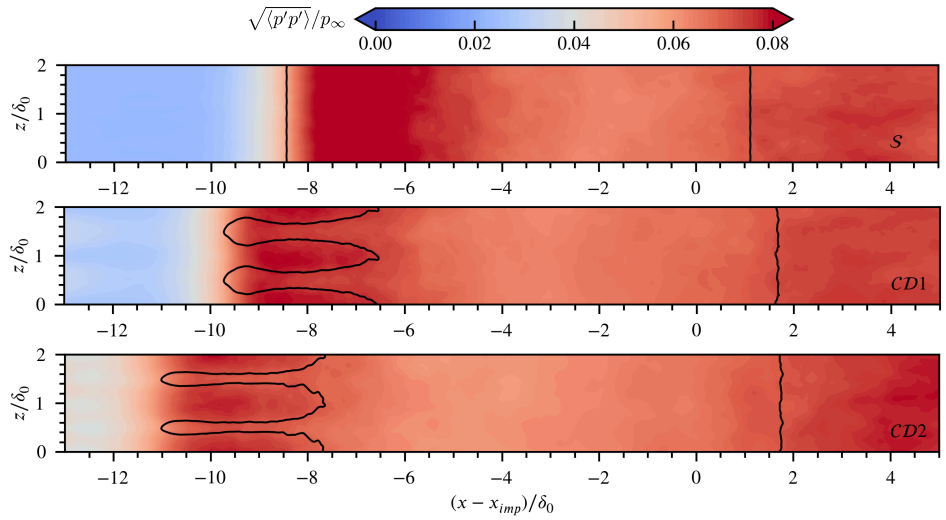

Figure 3.12: Wall-pressure fluctuation distribution downstream of riblets. Black lines denote the region of reverse-flow. DL is located at $z/\delta_0 = 0, 1, 2$, while CL is located at $z/\delta_0 = 0.5, 1.5$.

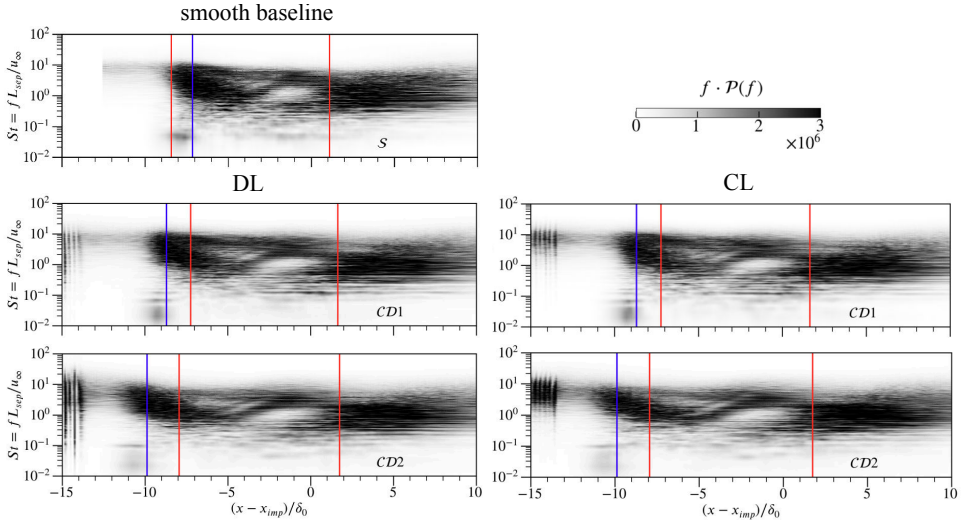

Figure 3.13: Pre-multiplied power spectral density maps of wall-pressure signals along streamwise direction at DL (left column) and CL (right column). The red lines denote the separation and reattachment locations, while the blue lines indicate the location of the pressure fluctuation peak.

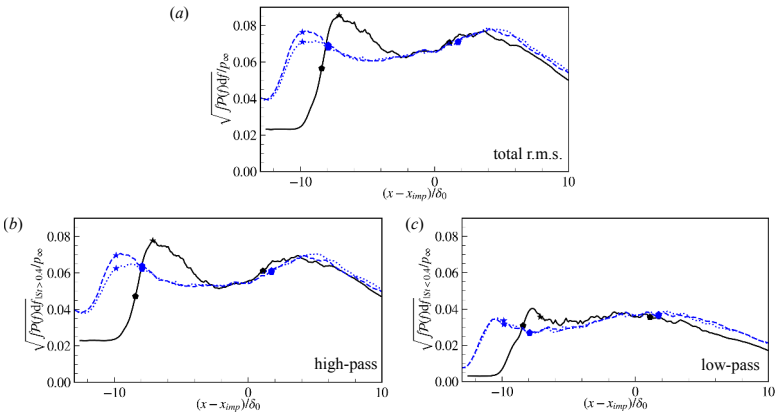

Figure 3.14: Wall-pressure fluctuations obtained by integrating the power spectral density: (a) total fluctuation, (b) contribution from the low-frequency content, and (c) contribution from the high-frequency content. The black line corresponds to case $\mathcal{S}$, while the blue dashed and dotted lines represent the results at the DL and CL for $\mathcal{CD}2$, respectively. Star markers indicate the locations of the maximum wall-pressure fluctuation, and pentagon markers denote the spanwise-averaged separation and reattachment points.

level is clearly higher at the DL than that at the CL, which is consistent with the trend observed in Figure 3.10(c).

The contributions of the low- and high-frequency components to the wall-pressure fluctuations have been computed by filtering the PSD with a spectral cut-off filter. The cut-off frequency separating the low- and high-frequency ranges is set to $St_{L_{sep}} = 0.4$, following our previous work (Wu et al., 2026), in which this value was shown to provide a clear separation between low- and high-frequency contributions. In Figure 3.14, it is observed that, for $\mathcal{CD}2$, the peak values of both the low-frequency and high-frequency contributions at the DL and CL are consistently lower than those of $\mathcal{S}$, indicating that the riblet configuration attenuates wall-pressure fluctuations across both frequency bands. A clear difference between the DL and CL is observed near the fluctuation peak, where the high-frequency component is more strongly reduced at the CL. In contrast, the low-frequency pressure fluctuations exhibit nearly identical levels at the DL and CL.

Overall, these results indicate that the spanwise heterogeneity of the wall-pressure fluctuations near the shock foot primarily originates from the stronger attenuation of the high-frequency component at the CL. This observation can be attributed to the upwash induced by the secondary flow, which lifts the turbulence-rich shear layer away from the wall, thereby reducing the high-frequency pressure fluctuations sensed at the wall.

3.3. CONCLUSION

In this chapter, the effects of convergent–divergent (C–D) riblets on a Mach 2.0 impinging shock-wave/turbulent boundary layer interaction (STBLI) are investigated using wall-resolved large-eddy simulations at $Re_\tau = 355$. A smooth-wall baseline case and two controlled cases employing C–D riblet patches with heights of 3% and 10% boundary layer thickness, installed upstream of the interaction region, are considered under identical

inflow conditions.

The results show that the C–D riblets induce well-organized counter-rotating vortices within the turbulent boundary layer, characterized by downwash at the divergent lines (DLs) and upwash at the convergent lines (CLs) of the riblets. These secondary flows substantially modify the incoming boundary layer prior to the interaction: the bottom part of the velocity profile becomes fuller near the wall at the DLs and less full at the CLs, while the subsonic portion of the boundary layer is significantly enlarged. Also the spanwise averaged boundary layer is less full than that over the smooth wall. As a consequence, the shock–boundary layer interaction region is enlarged, and the separation topology is altered, with separation being suppressed near the DLs but promoted near the CLs.

The peak wall-pressure fluctuations near the shock foot are attenuated by the C–D riblets. This attenuation results from a reduction in both the low- and high-frequency components of the pressure fluctuations. In addition, pronounced spanwise heterogeneity of wall-pressure fluctuations is observed near the separation shock foot, which is primarily attributed to the stronger attenuation of the high-frequency content at the CLs due to the lift-up effect induced by the secondary flow.

Overall, this study demonstrates that C–D riblets are capable of reshaping the separation bubble and attenuating wall-pressure fluctuations in STBLI through systematic modification of the incoming turbulent boundary layer. However, similar to micro-vortex generators, the effectiveness of C–D riblet patches is expected to be sensitive to their installation location because of the rapid decay of the induced vortices. Moreover, they inevitably introduce additional parasitic drag. These limitations motivate the exploration of alternative passive control strategies that retain the benefits of flow manipulation while alleviating the associated drawbacks. Such considerations naturally lead to the investigation of ridge-type roughness, which is the focus of the next two chapters.

4

RIDGE-TYPE ROUGHNESS

失之东隅，收之桑榆。
What was lost in one respect was gained in another.
《后汉书》/ *Book of the Later Han*

Parts of this chapter have been published in *Flow Turbul. Combust.* **115**, 29-49, (Wu et al., 2025b).

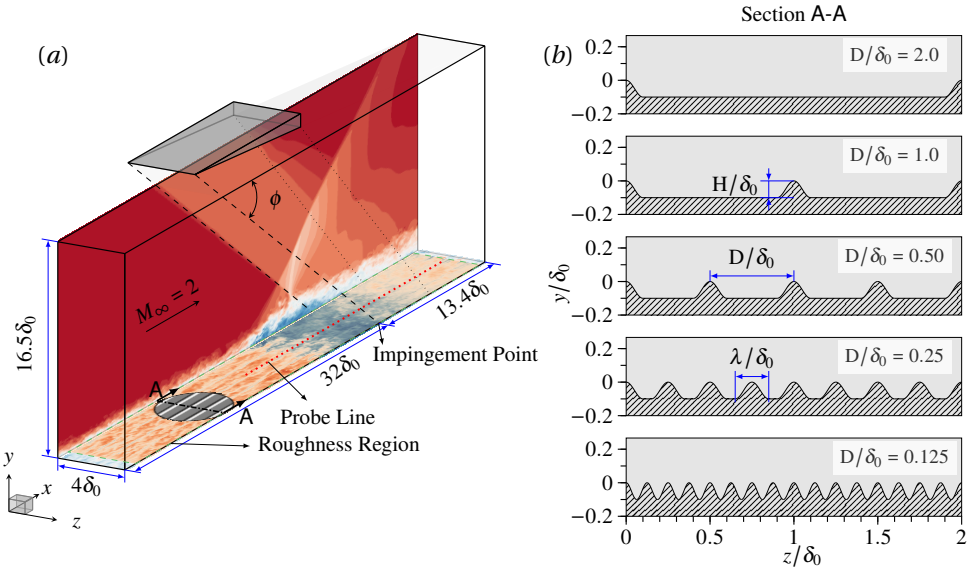

Figure 4.1: (a) Schematics of the computational domain (including streamwise velocity contours), and (b) schematic view of the investigated ridge-type rough walls with relevant definitions.

As discussed in Section 1.5, ridge-type roughness can induce large-scale secondary flows in turbulent boundary layers, which may in turn modulate the STBLI. Moreover, due to its streamwise-homogeneous geometry, it does not introduce pressure drag and is expected to be insensitive to the installation location. In this chapter, the effects of ridge-type roughness on STBLI are therefore investigated.

4.1. FLOW CONFIGURATION AND NUMERICAL SETUP

4.1.1. FLOW CONFIGURATION

Five ridge-type rough-wall configurations with different ridge spacings are investigated in this chapter. These cases are considered together with the baseline case presented in the previous chapter. The same flow configuration described in Chapter 3 is adopted, namely a Mach 2.0 turbulent boundary layer interacting with an oblique impinging shock wave with a shock angle of $\phi = 40.04°$. The same flow parameters are also used. This results in the STBLI flow depicted in Figure 4.1(a).

4.1.2. ROUGHNESS GEOMETRY

The spanwise heterogeneous roughness consists of sinusoidal ridges with non-dimensional spacing D/δ_0, width λ/δ_0, and height H/δ_0, see Figure 4.1(b). To better assess their efficacy for STBLI control, a parametric study on the ridge spacing is performed, where considered values are $D/\delta_0 = \{2.0, 1.0, 0.5, 0.25, 0.125\}$, or $D/\delta_{imp} = \{1.35, 0.68, 0.34, 0.17, 0.085\}$ if normalized with boundary layer thickness at the virtual impingement point, as shown in Figure 4.1(b). The normalized ridge spacing values are also included in Table 4.1 for

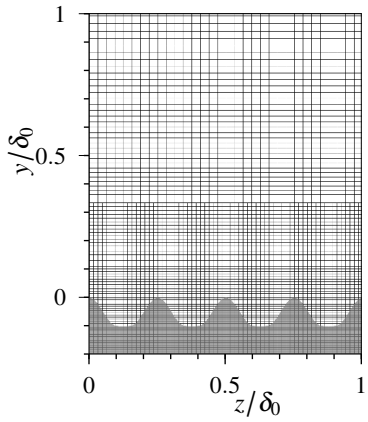

Figure 4.2: A zoomed-in view of the Cartesian mesh near the rough wall with $D/\delta_0 = 0.25$ in the cross-stream plane. The mesh is uniform in the streamwise direction.

convenience. The non-dimensional height of the ridges is $H/\delta_0 = 0.1$ and their width is $\lambda/\delta_0 = 0.2$ for all rough wall cases, except the case with $D/\delta_0 = 0.125$ which does not have the flat bottom valley and only consists of continuous sinusoidal waves with $D = \lambda$ due to the limited space in the spanwise direction. If scaled with the viscous length of the baseline case at the inlet, the non-dimensional width and height are $\lambda^+ = \lambda/\delta_v = 49.6$ and $h^+ = H/\delta_v = 24.8$. Note that the crests of the ridges are at the plane of $y = 0$ and the geometry of the ridge-type roughness is homogeneous along the streamwise direction.

4.1.3. BOUNDARY CONDITIONS AND GRID DISTRIBUTION

The boundary conditions are identical to those described in Section 3.1.3; the only difference is that the wall geometry is replaced from the C-D riblets to ridge-type roughness.

The Cartesian grid for the smooth-wall baseline case is the same as in Chapter 3: consists of $N_x \times N_y \times N_z = 512 \times 192 \times 128 = 12.6 \cdot 10^6$ cells. The grid resolution in wall units is $\Delta x^+ = 21.9$ and $\Delta z^+ = 7.74$, with $\Delta y^+_{wall} \leq 0.93$. The mesh is coarsened in the streamwise and spanwise directions within the boundary layer above $y \approx 0.7\delta_0$ and within the freestream flow. For the rough wall cases, the mesh is locally refined near the wall to fully resolve the geometry and turbulent structures around the roughness ridges, see Figure 4.2. Note that the shape of each sinusoidal ridge is well resolved with 14 cells and the mesh is stretched in the wall-normal direction with a very mild constant stretching factor of 1.02. For the controlled cases, the viscous-scaled grid resolution is $\Delta x^+ = 5.49$, $\Delta z^+ = 3.87$, $\Delta y^+_{wall} \leq 0.93$, which is much finer than what is normally required in LES, resulting in $58.7 \cdot 10^6$ cells in total.

4.1.4. OTHER NUMERICAL SETUP

All simulations were initialized from the inviscid shock-reflection solution. After an initial transient period of approximately 2000 δ_0/u_∞, each case was further integrated for more than 4000 δ_0/u_∞ to ensure statistically converged results, particularly for the low-frequency dynamics characteristic of STBLI. Flow statistics were obtained by time-

STBLI case	smooth	$\mathcal{R}_1$	$\mathcal{R}_2$	$\mathcal{R}_3$	$\mathcal{R}_4$	$\mathcal{R}_5$
D/δ_0	—/—	2.0	1.0	0.5	0.25	0.125
D/δ_{imp}	—/—	1.35	0.68	0.34	0.17	0.085
H_{md}/H	—/—	0.05	0.10	0.20	0.40	0.5
$\Delta\langle u\rangle^+_{vD}$	0.0	1.05	1.42	2.31	1.91	-0.16
H_{sonic}/δ_{99}	0.096	0.106	0.110	0.112	0.138	0.131
H_{vortex}/δ_{99}	0.0	0.50	0.58	0.45	0.23	0.12
$\langle v\rangle_{max}/u_\infty * 100$	0.0	3.04	2.99	2.86	1.37	0.56
L_{sep}/δ_0	9.48	9.86	9.70	11.46	13.27	13.25
$A_{sep}/A_{sep_{smooth}}$	1.00	0.85	0.87	1.09	1.41	1.49
p_t/p_{t_0}	0.9391	0.9377	0.9374	0.9396	0.9443	0.9424

Table 4.1: Summary of parameters in STBLI cases.

averaging the instantaneous three-dimensional solutions. An array of numerical probes was placed at the ridge top in the mid-plane for the following spectral analysis, with a sampling rate of $f_s \approx 46u_\infty/\delta_0$. Additionally, instantaneous three-dimensional snapshots of the interaction region were saved at intervals of $\Delta t \approx \delta/u_\infty$ for instantaneous flow analysis, yielding an ensemble of approximately 4100 snapshots per case.

4.2. EFFECTS OF RIDGE SPACING ON THE MEAN FLOW

4.2.1. COMPARISON OF MEAN VELOCITY AND REYNOLDS-STRESS PROFILES

The state of the incoming turbulent boundary layer (TBL) plays a pivotal role in the STBLI dynamics and organization, particularly in light of the working principle of the proposed flow-control method. Therefore, the analysis of the results is first focused on the upstream TBL. A probing station located $20\delta_0$ upstream of the impingement point, which is free from the influence of the STBLI, is used for this purpose. Meanwhile, the probing station, situated $12\delta_0$ downstream from the inflow plane, is appropriately positioned to ensure the turbulence reaches equilibrium (Morgan et al., 2011; Laguarda and Hickel, 2024a).

In order to better compare the characteristics of the TBL and to also assess the outer-layer similarity between the smooth wall and rough wall cases, a shifted wall-normal coordinate correction is considered. As explained by Chung et al. (2021), this is necessary because the outer turbulent flow does not perceive its origin at $y = 0$ if the wall is rough. The origin of the wall-normal coordinate is thus shifted to the average roughness elevation height, or meltdown height, above the valley of the rough wall. The functional relation between y_s/δ_0 and y/δ_0 can be written as:

$$y_s/\delta_0 = (y + H - H_{md})/\delta_0 \tag{4.1}$$

This is illustrated in Figure 4.4, which shows the definition of the shifted wall-normal coordinate y_s and the non-dimensional roughness meltdown height H_{md}/δ_0. For the

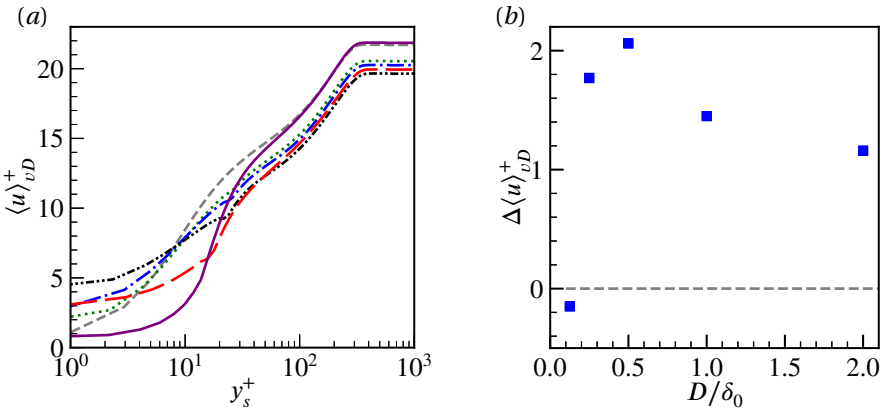

Figure 4.3: (a) van Driest transformed mean velocity profiles of the incoming turbulent boundary layer for: -- smooth wall; ····· $D/\delta_0 = 2.0$; -·-· $D/\delta_0 = 1.0$; -··-·· $D/\delta_0 = 0.5$; — — $D/\delta_0 = 0.25$; — $D/\delta_0 = 0.125$. (b) Roughness function for different non-dimensional ridge spacings. All results are taken at $(x - x_{imp})/\delta_0 = -20.0$.

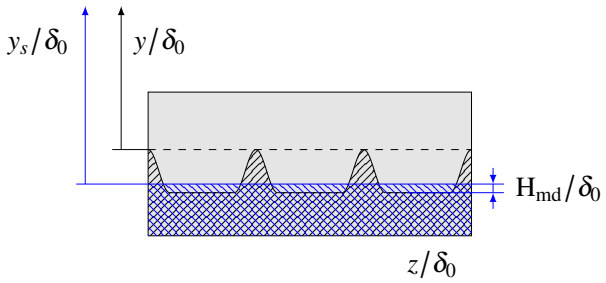

Figure 4.4: Definition of the shifted wall-normal coordinate y_s and roughness meltdown height H_{md}.

smooth wall case, y_s/δ_0 simplifies to y/δ_0.

A comparison of the van Driest transformed mean velocity profiles of the controlled cases is shown in Figure 4.3(a). It is worth mentioning that intrinsic averaging is applied, considering only the fluid volume fraction of cells that are cut by the geometry as weights when calculating the flow statistics. A clear downshift of the profile is observed for all rough-wall cases except for the case with a ridge spacing of $D/\delta_0 = 0.125$. The downshift indicates a drag increase and the corresponding momentum deficit due to the surface roughness, which can be quantified with the roughness function $\Delta\langle u \rangle^+_{vD} = \langle u \rangle^+_{vD,S} - \langle u \rangle^+_{vD,R}$, where $\langle u \rangle^+_{vD,S}$ and $\langle u \rangle^+_{vD,R}$ represent the velocity profile over the smooth wall and the rough wall, respectively. The larger $\Delta\langle u \rangle^+_{vD}$, the higher the added drag as a result of the roughness (Chung et al., 2021). Note that the downshift of velocity profiles is usually measured in the log-law region; however, $\Delta\langle u \rangle^+_{vD}$ is measured here in the free stream because the investigated Reynolds number is low.

Figure 4.3(b) shows the relation between $\Delta\langle u \rangle^+_{vD}$ and D/δ_0. Interestingly, when D/δ_0 decreases, $\Delta\langle u \rangle^+_{vD}$ increases first (i.e., increased added drag) and then decreases. For the smallest spacing $D/\delta_0 = 0.125$, $\Delta\langle u \rangle^+_{vD}$ drops below zero, indicating a decrease in drag

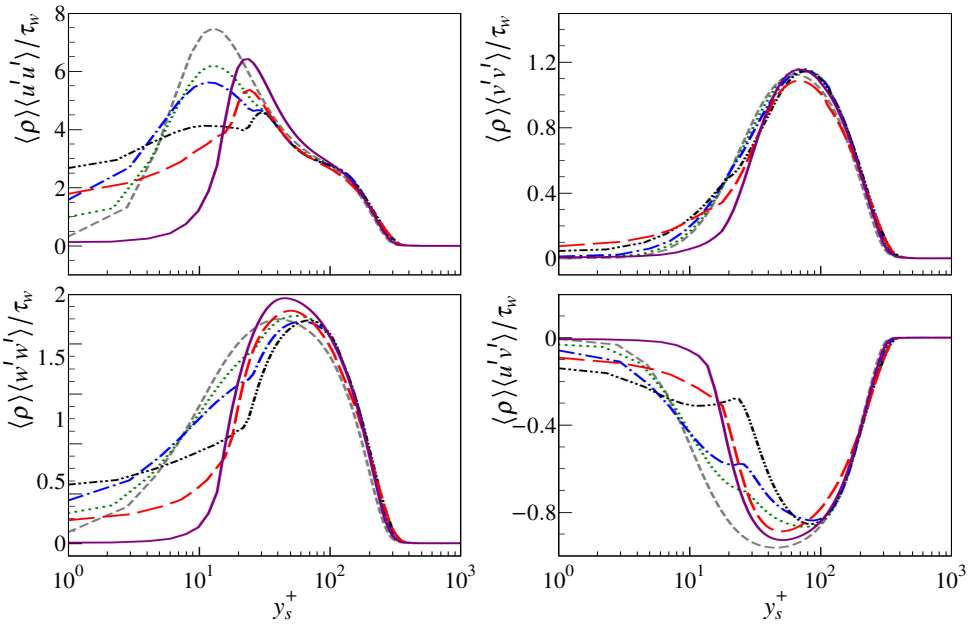

Figure 4.5: Density scaled Reynolds stress profiles of the incoming turbulent boundary layer at $(x - x_{imp})/\delta_0 = -20.0$ for smooth wall and rough wall cases: – – – smooth wall; ····· $D/\delta_0 = 2.0$; –·– $D/\delta_0 = 1.0$; –··– $D/\delta_0 = 0.5$; — — $D/\delta_0 = 0.25$; — $D/\delta_0 = 0.125$.

compared to the smooth wall. This non-monotonic trend of $\Delta\langle u\rangle^+_{vD}$ is consistent with previous studies of Deyn et al. (2022a). The effect of the ridge spacing is expected to tend to diminish when the spacing approaches zero or infinity since – in both circumstances – the rough wall asymptotically tends towards an effectively smooth wall. For large finite ridge spacing, friction increases due to the larger wetted area compared to a smooth wall. As the spacing keeps decreasing, the ridge-type rough wall eventually transitions into the category of riblets and the skin friction reduces by exposing less surface area to high-velocity flow (Choi et al., 1993).

Profiles of the Reynolds stresses $\tau_{ij} = \langle\rho\rangle\langle u'_i u'_j\rangle$ for the smooth-wall and rough-wall cases are compared in Figure 4.5. The Reynolds stresses are normalized with the local wall shear at the probing station, whose value is obtained by integrating the wall shear stress in the spanwise direction over the wetted area and then normalizing it by the projected (plane) area. The profiles match well in the outer region of the TBL, while visible differences are found in the inner region up to approximately $y_s^+ = 100$ due to different wall geometries. The peak of $\tau_{xx} = \langle\rho\rangle\langle u'u'\rangle$ reduces when D/δ_0 decreases from 2.0 to 0.5 and then increases for D/δ_0 from 0.5 to 0.125. The Reynolds shear stress shows a similar trend when the ridge spacing varies.

4.2.2. ROUGHNESS-INDUCED SECONDARY FLOWS

The instantaneous vortical structures are visualized with the Q criterion in Figure 4.6. Compared with the smooth-wall case, the introduction of ridge-type roughness visibly

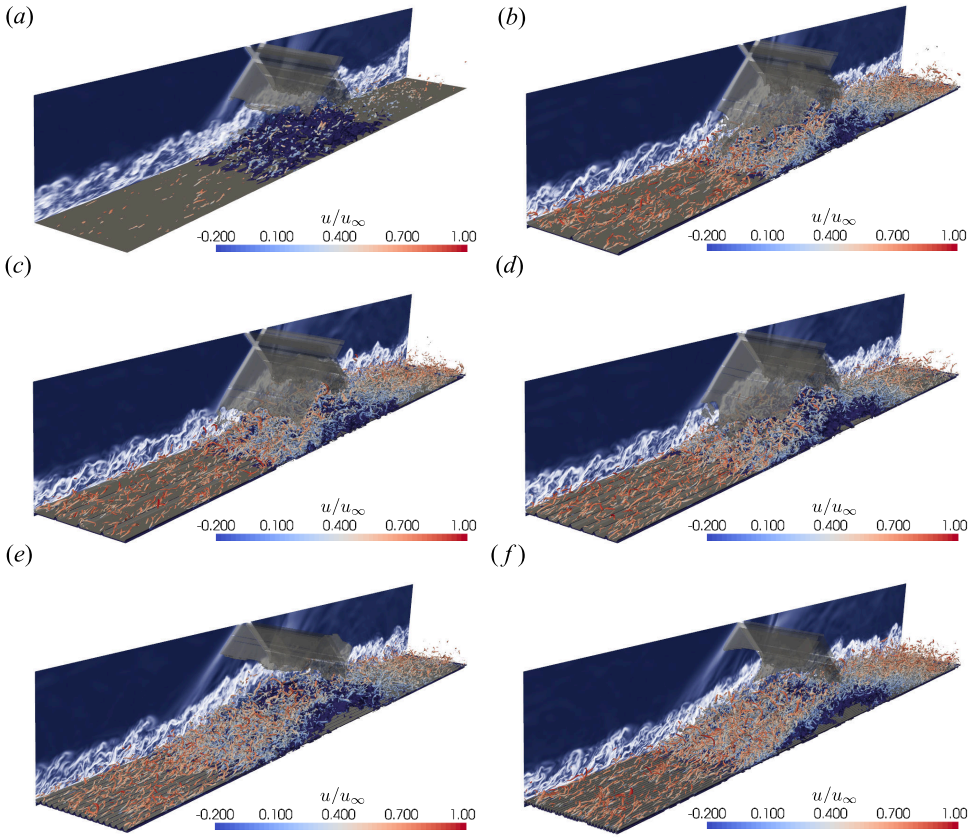

Figure 4.6: Instantaneous vortical structures in the STBLI region for different ridge-type roughness spacings. The vortical structures are identified using the Q criterion ($Q_{cr} = 5.3$) and coloured by the normalized streamwise velocity u/u_∞. The dark-blue region corresponds to the reversed-flow region. Panels (a)–(f) correspond to the smooth-wall case and rough-wall cases with $D/\delta_0 = 2.0$, 1.0, 0.5, 0.25, and 0.125, respectively.

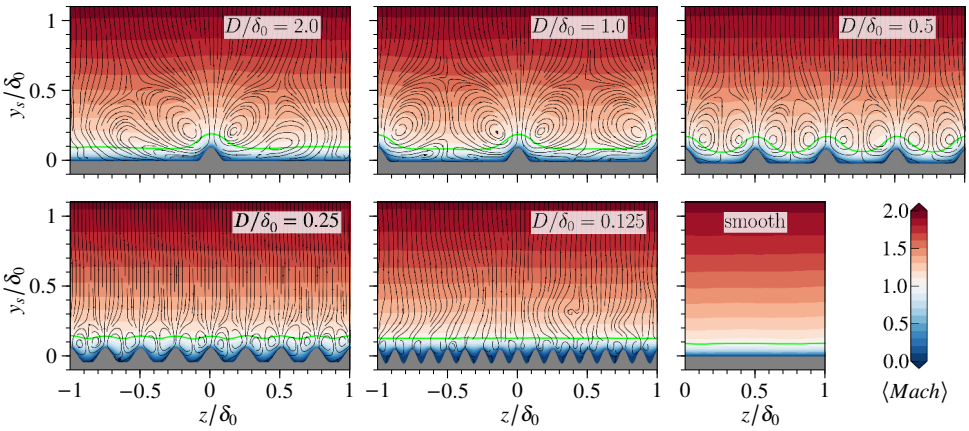

Figure 4.7: Mean flow streamlines and Mach number distribution in a cross-stream plane at $(x-x_{imp})/\delta_0 = -20$. The sonic line is shown in lime.

modifies the upstream turbulent boundary layer before it encounters the shock. The rough-wall cases exhibit a much denser population of streamwise-oriented vortical structures upstream of the interaction region, indicating that the incoming boundary layer has already been disturbed by the surface roughness. This upstream modification affects the subsequent STBLI, with the reversed-flow region progressively enlarging as the ridge spacing decreases from $D/\delta_0 = 1.0$ to $D/\delta_0 = 0.25$.

The time-averaged roughness-induced secondary flow is visualized in Figure 4.7, which shows streamlines and Mach number distribution of the mean flow in the cross-stream plane at $(x-x_{imp})/\delta_0 = -20$. Clear streamwise vortices induced by the roughness structure can be observed in the cross-stream plane, with upwash occurring at the ridges for all rough wall cases, consistent with findings from the incompressible flow experiment of Zampiron et al. (2020). The effect of rough walls on the Mach number distribution is confined within the thickness of the TBL, that is, the outer flow is only marginally affected by the rough wall upstream of the interaction region. The shape of the sonic line, see the lime line around 0.1 δ_0 above the wall in Figure 4.7, is clearly altered by the wall shape. For larger ridge spacing cases, the sonic line basically follows the curvature of the rough wall structure. For the smaller ridge spacing cases, the sonic line remains at a distance of 0.1 δ_0 above the ridges and tends to recover a straight line. Note that this causes a larger subsonic cross-section area as compared to the smooth wall and the cases with wide ridge spacing. Figure 4.9(a) summarizes the spanwise-averaged height of the sonic lines expressed in the shifted wall normal coordinate. By measuring from the shifted wall origin, the spanwise-averaged height conveniently represents the subsonic area of the incoming boundary layer. When reducing the ridge spacing, the mean sonic height increases first, reaching for $D/\delta_0 = 0.25$ the maximum value of 48% larger than the one in the smooth wall case, and then decreases.

Contours of the vertical velocity and velocity vectors in Figure 4.8 also visualize the secondary-flow vortices. The maximum magnitude of the vertical velocity is observed to be around 3% of the freestream velocity, which agrees with the results reported by

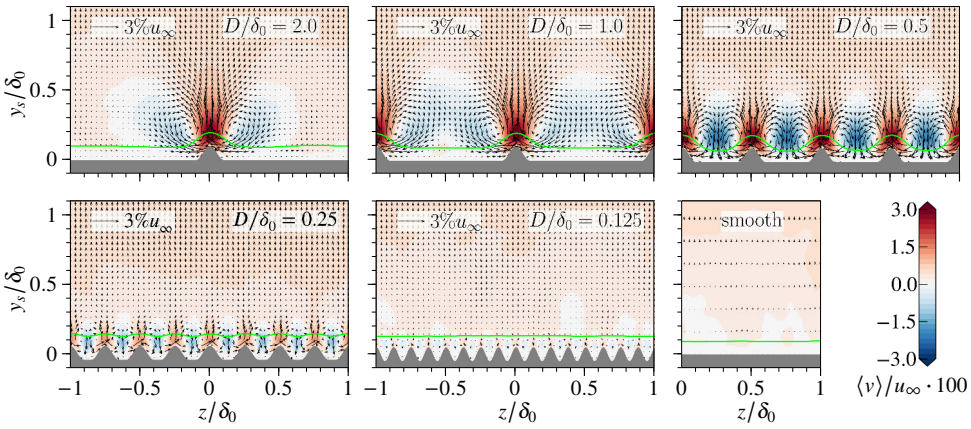

Figure 4.8: Mean vertical velocity in a cross-stream plane at $(x - x_{imp})/\delta_0 = -20$ with superposed cross-stream velocity vectors. The sonic line is shown in lime.

Vanderwel et al. (2019). From the streamline map of Figure 4.7, it seems that another vortex pair adjacent to the vortex touching the ridges is induced in the cases $D/\delta_0 = 2.0, 1.0$. However, this vortex pair is actually rather weak compared to the vortex pair near the ridges. Figure 4.8 shows that the magnitude of cross-stream velocity vectors in the valley is close to zero. The size of secondary flow vortices, which is here measured as the distance from the shifted wall origin to the highest location with secondary flow towards the wall, increases with D/δ_0 and reaches a maximum of around 0.5 local boundary layer thickness δ_{99} in case D/δ_0=1.0 as shown in Figure 4.9(b). This trend of size increase aligns with the findings of Zampiron et al. (2020) and Zhdanov et al. (2024), who indicate that in incompressible channel flow over ridges, the size of secondary vortices increases until they fill the entire channel.

The intensity of the secondary flows can be evaluated both locally and globally. Locally, the intensity of the secondary motions can be represented by the maximum vertical velocity of the secondary flows before the interaction, as shown in Figure 4.9(c). The maximum vertical velocity increases with the ridge spacing from $D/\delta_0 = 0$ to 1.0 and then remains almost constant regardless of the increase of the ridge spacing. However, the maximum downwash velocity in the valleys reduces with the larger ridge spacing as the vortices stretch wider. On the other hand, the global intensity of the secondary flow can be quantified by the variable introduced by Guo et al. (2022c), which is defined in Equ. 3.1. As shown in Figure 4.9(d), the global intensity I peaks at $D/\delta_0 = 0.5$, which is consistent with the observation in Figure 4.8 that strong secondary vortices fully fill the whole span for the case with $D/\delta_0 = 0.5$.

4.2.3. SPANWISE AVERAGED VARIABLES IN THE INTERACTION REGION

Figure 4.10 shows contour plots of the mean pressure fluctuation distribution on the $z = 0$ plane for all cases. The shock system, sonic line, and separation lines are superimposed on the contours to provide a reference. It is clear that the most intensive pressure fluctuations appear along the separation shock, especially in the part above the intersection of incident

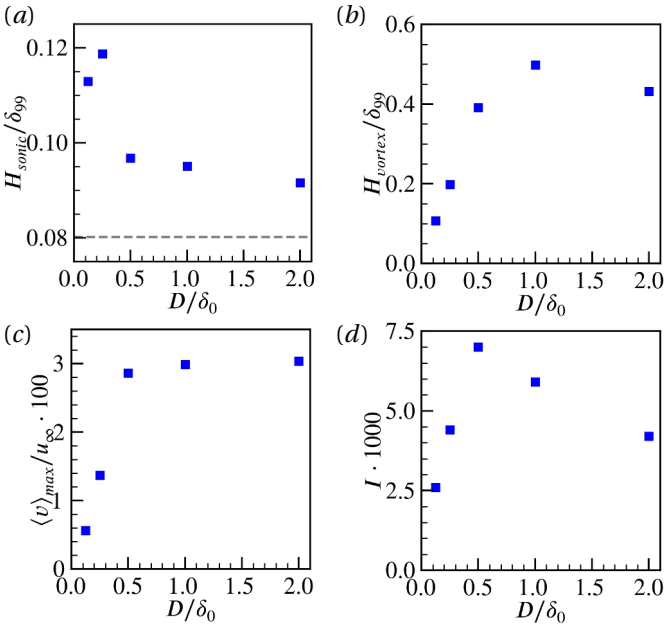

Figure 4.9: (a) Spanwise-averaged height of the mean sonic line, (b) height of the secondary vortices induced by the rough wall structure, (c) maximum value of the mean vertical velocity, and (d) mean secondary flow intensity of such vortices at $(x - x_{imp})/\delta_0 = -20$ as a function of the ridge distance D/δ_0 . The corresponding value from the smooth wall case is indicated with a dashed line in (a).

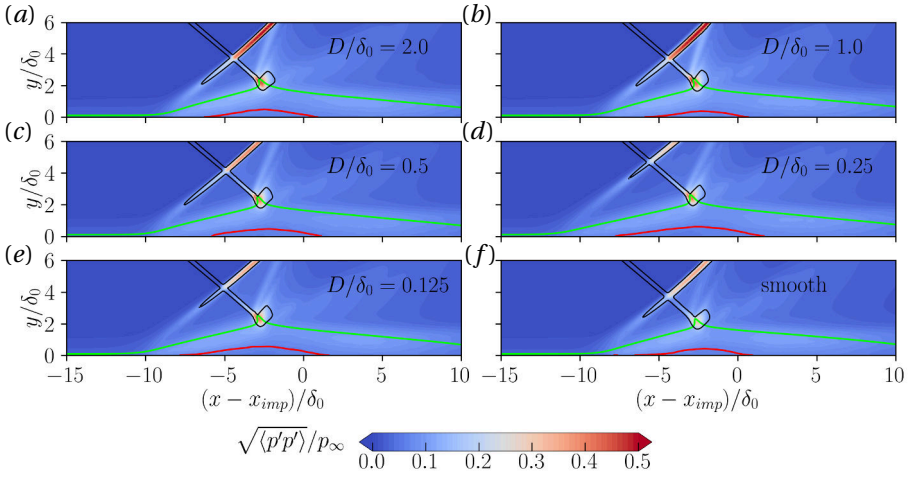

Figure 4.10: Mean pressure fluctuation distribution at $z = 0$ plane. Solid line color legend: zero mean streamwise velocity (red), mean sonic line (lime) and mean shock position (black).

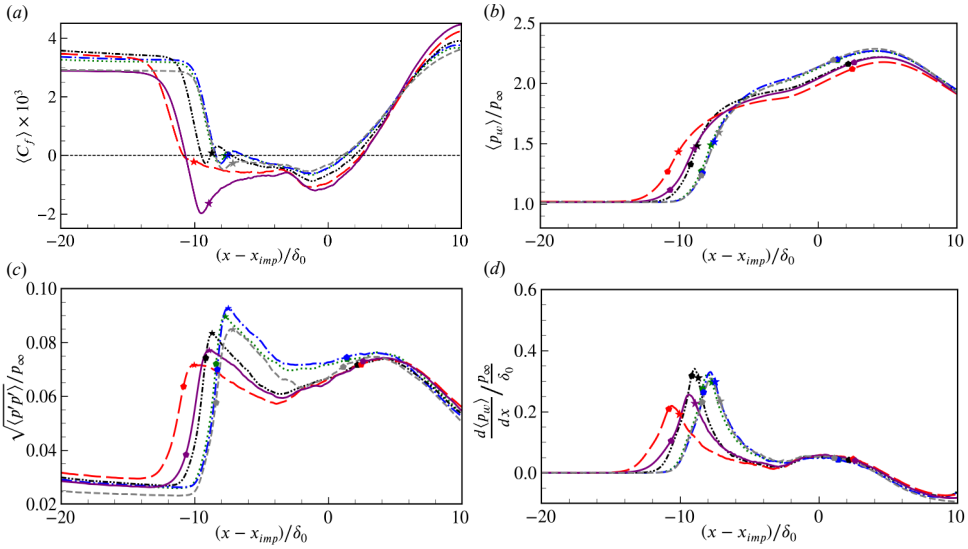

Figure 4.11: Spanwise averaged (a) wall-pressure and (b) wall-pressure fluctuation (c) friction coefficient along streamwise direction for: - - - smooth wall; ····· $D/\delta_0 = 2.0$; -·-·- $D/\delta_0 = 1.0$; -··-·· $D/\delta_0 = 0.5$; — — $D/\delta_0 = 0.25$; —— $D/\delta_0 = 0.125$. Pentagon markers show the separation/reattachment location, and star markers represent the location of maximum pressure fluctuation.

shock and separation shock. Another region of high pressure fluctuations is found around the location where the incident shock impinges on the shear layer. Milder pressure fluctuations are found along the sonic line and expansion fan. Compared with the smooth wall case, cases $D/\delta_0 = 2.0$ and $D/\delta_0 = 1.0$ show a higher pressure fluctuation intensity at the separation shock. Contrarily, case $D/\delta_0 = 0.25$ exhibits the weakest pressure fluctuations at the separation shock. It is also noticeable that the case $D/\delta_0 = 0.25$ is characterized by an elevated shock intersection point and the longest interaction length, and the separation region is clearly enlarged for this case. To better quantify the impact of wall roughness, the streamwise distributions of the skin friction coefficient $\langle C_f \rangle$, spanwise-averaged wall-pressure $\langle p_w \rangle / p_\infty$, wall-pressure fluctuation $\sqrt{\langle p'p' \rangle}/p_\infty$, and wall-pressure gradient along streamwise direction $\mathrm{d}\langle p_w \rangle / \mathrm{d}x$ are discussed next.

Figure 4.11(a) shows that the friction coefficient C_f upstream of the interaction region changes in a non-monotonic fashion with increasing D/δ_0, reaching a maximum value for $D/\delta_0 = 0.5$. This is consistent with the analysis of the upstream TBL. The C_f distribution also indicates that the separation region is divided into a primary separation zone and a secondary separation zone for large ridge spacing cases, i.e., $D/\delta_0 = 2.0, 1.0, 0.5$. The total separation length increases when decreasing D/δ_0 from 1.0 to 0.25, while it remains almost unaffected for other values of D/δ_0 and slowly approaches the smooth wall case for further increased or decreased ridge spacing. The case $D/\delta_0 = 0.125$ exhibits the lowest $\langle C_f \rangle$ in the separation region, especially right after the separation, indicating a stronger reverse flow in the separation bubble.

The wall-pressure distributions are shown in Figure 4.11(b), where no significant difference is observed between the smooth wall and the $D/\delta_0 = 2.0, 1.0$ cases. However,

when D/δ_0 decreases from 1.0 to 0.25, the onset of the interaction moves upstream, resulting in an increase in the total interaction length. For $D/\delta_0 = 0.125$, the onset location moves downstream instead. At the same time, the maximum wall-pressure near the reattachment point first drops, then rises with decreasing D/δ_0. A non-monotonic trend is evident, with the case $D/\delta_0 = 0.25$ exhibiting the longest interaction length yet the smallest pressure increase, resulting in the most gradual pressure rise. Profiles of the wall-pressure r.m.s. fluctuation are shown in Figure 4.11(c). A typical feature of impinging STBLI is that the pressure fluctuation exhibits a local minimum in the middle of the separation bubble and local maxima near the separation and reattachment points (Pasquariello et al., 2017). It is evident that for $D/\delta_0 = 2.0$ and 1.0, the peak value of $\sqrt{\langle p'p' \rangle}/p_\infty$ slightly increases compared with that in the baseline case. We also observe that the peak value in the case $D/\delta_0 = 0.25$ is 12% lower than the baseline peak value, which hints at an attenuated separation shock unsteadiness. Therefore, it is worth investigating in more detail the behavior of the pressure fluctuations across different frequencies, which might provide additional insight on the reduction of the pressure peak and the mechanism responsible for this. This will be partially addressed in the upcoming sections. Case $D/\delta_0 = 0.125$ shows a peak pressure fluctuation between the values for $D/\delta_0 = 0.25$ and the smooth wall case. The location of the peak pressure fluctuation moves similarly to the onset of the interaction, with case $D/\delta_0 = 0.25$ exhibiting the most upstream location, which is consistent with a substantial increase in the size of the reverse-flow region. The streamwise wall-pressure gradient is shown in Figure 4.11(d). For cases with relatively large ridge spacing ($D/\delta_0 = 0.5, 1.0, 2.0$), the peak wall-pressure gradient is slightly higher than that of the smooth-wall case. In contrast, cases with smaller ridge spacing exhibit a reduced peak wall-pressure gradient, indicating a more smeared separation shock foot.

4.2.4. EFFECTS ON SEPARATION REGION

Figure 4.12 shows the local skin-friction coefficient distribution projected on the horizontal plane, thus including the effect of the increased wetted area. Before the interaction region, the skin friction shows the periodic pattern of the ridges, where higher friction appears due to the increased surface area. The separation and reattachment lines are highly spanwise corrugated in rough wall cases. This is because the ridges protrude into higher-speed flow, delaying separation and accelerating reattachment on top of the ridges relative to the flow in the valleys. The flow near the corners between ridges and valleys separates more easily due to corner effects. At corners, the wall-shear stress on the two adjacent walls reduces and it drops to zero right at the corner, giving rise to a less full boundary layer in this region, thus promoting separation. An interesting observation for cases with larger ridge spacing, such as $D/\delta_0 = 2.0, 1.0, 0.5$, is that the flow over the valleys reattaches to the wall shortly after the initial separation, forming a locally attached region before the main separation bubble. A similar flow topology was also reported by Guo et al. (2022a). The flow over the valley for these three cases, $D/\delta_0 = 2.0, 1.0, 0.5$, delays the mean-flow separation compared to the smooth wall case. This is believed to be the result of the downwash flow, which enhances momentum exchange brought about by the secondary vortices. For smaller ridge spacing, the subsonic region of the upstream turbulent boundary layer becomes thicker, promoting the upstream propagation of the

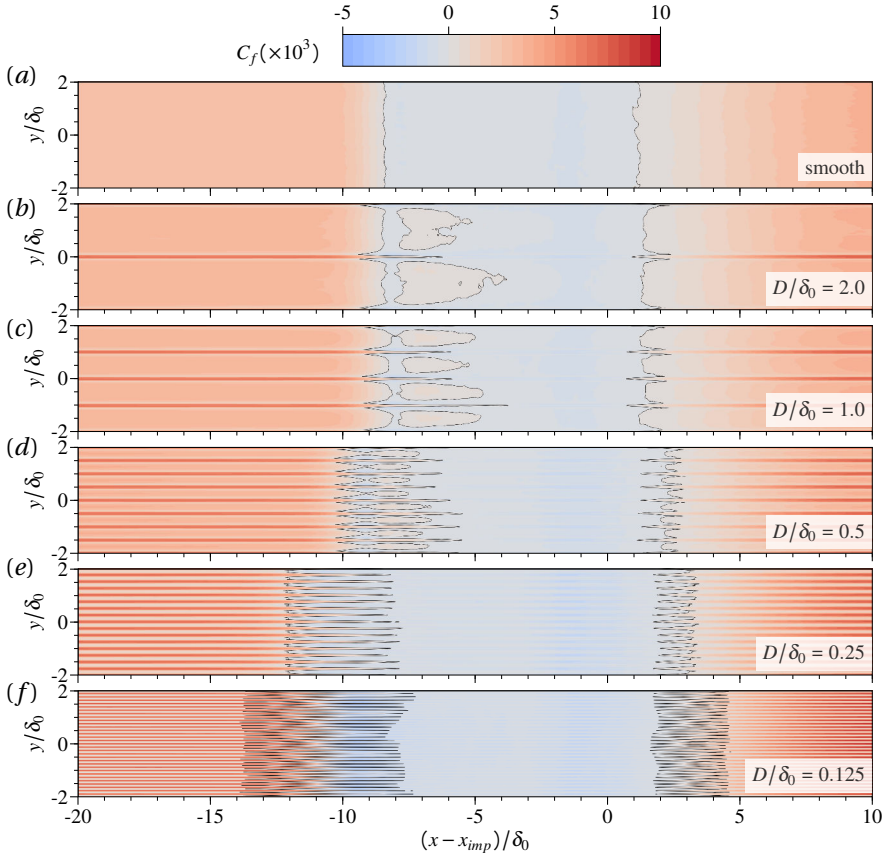

Figure 4.12: Local skin friction coefficient distribution projected on the horizontal plane. Black lines denote the location where $\langle C_f \rangle = 0$.

adverse pressure gradient, making separation more likely.

Figure 4.13 summarizes how the separation length and separation area change with different ridge spacings. The separation length is calculated from the spanwise averaged $\langle C_f \rangle$ distribution, and measured as the distance between the first separation point to the final reattachment point. For cases $D/\delta_0 = 2.0, 1.0$, the separation length is slightly larger than the smooth wall case, but the separation area reduces around 15% because the flow reattaches in the valleys. For the small ridge spacing case $D/\delta_0 = 0.25, 0.125$, the separation lengths increase by around 40% and the separation areas increase by 41% and 48% respectively.

4.2.5. EFFECTS ON TOTAL PRESSURE RECOVERY

The assessment of total pressure recovery holds critical importance in aero-engine inlet design. We therefore analyse the total pressure recovery at the $(x - x_{imp})/\delta_0 = 10$ plane, which is near the outlet of the computational domain. As shown in Figure 4.14(a), overall,

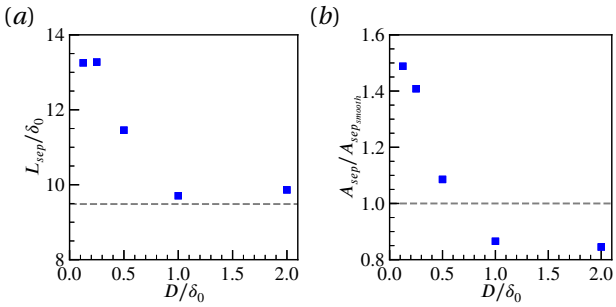

Figure 4.13: (a) Spanwise-averaged separation length and (b) relative separation area as a function of D/δ_0. The dashed line ---- denotes the corresponding value in smooth wall case.

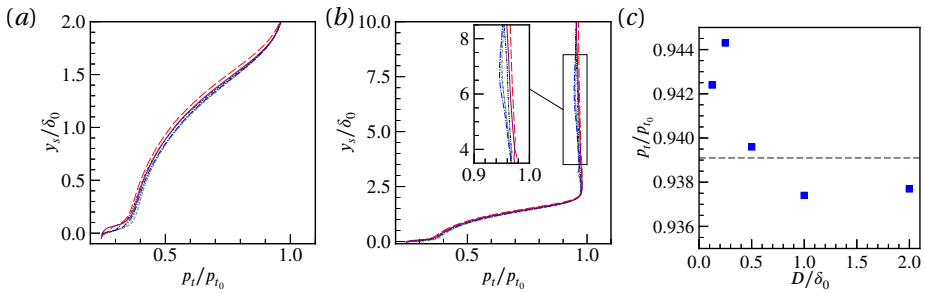

Figure 4.14: Spanwise-averaged total pressure recovery profile at the $(x - x_{imp})/\delta_0 = 10$ plane (a) near the wall and (b) away from the wall for: ---- smooth wall; ····· $D/\delta_0 = 2.0$; -·-· $D/\delta_0 = 1.0$; -··-·· $D/\delta_0 = 0.5$; — — $D/\delta_0 = 0.25$; —— $D/\delta_0 = 0.125$. (c) Mass-flow averaged total pressure recovery at the same plane as a function of D/δ_0.

the profiles for the smooth wall and two large ridge spacing cases $D/\delta_0 = 2.0$, 1.0 are very similar and have the highest total pressure in the near-wall region $y_s/\delta_0 < 2.0$. The total pressure recovery decreases as D/δ_0 reduces from 1.0 to 0.25, and subsequently increases as the ridge spacing decreases further. However, when the view is expanded to observe areas farther from the wall, as depicted in Figure 4.14(b), the trend in total pressure recovery with ridge spacing is inverted compared to the near-wall region. Case $D/\delta_0 = 0.25$ exhibits the highest pressure recovery in a relatively large region from $y_s/\delta_0 = 2.5$ until $y_s/\delta_0 = 10.0$. Even though the curves show only small differences, the trend is significant and consistent with the observation that cases with higher friction suffer from more viscous loss in the near-wall region, while they also benefit from a more diffused shock, resulting in higher total pressure recovery. Since the mass flow away from the wall is significantly higher than the mass flow near the wall, the overall effect is that case $D/\delta_0 = 0.25$ achieves an approximately 0.5% higher mass-flow averaged total pressure recovery than the smooth-wall case, see Figure 4.14(c).

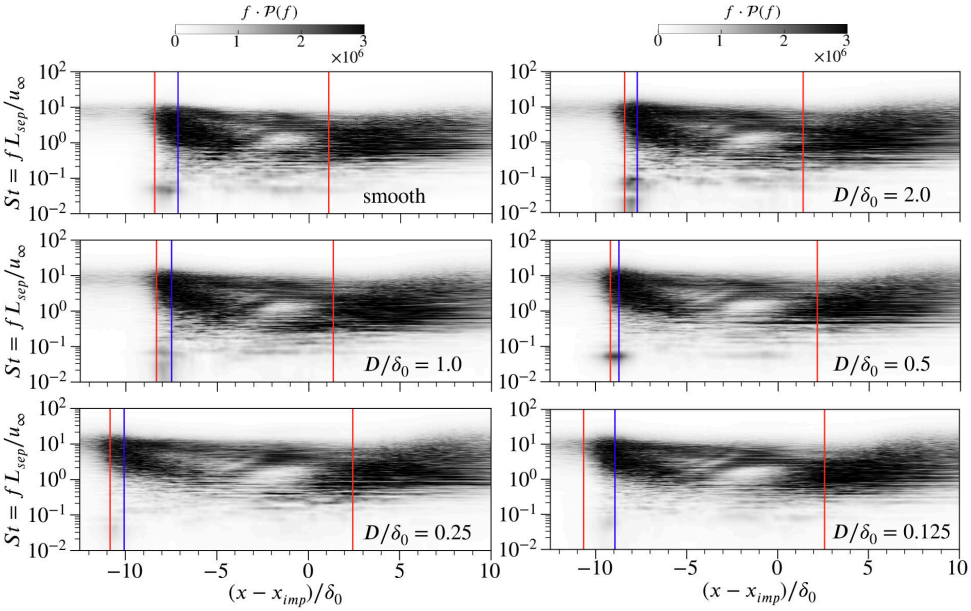

Figure 4.15: Pre-multiplied power spectra density maps of wall-pressure signals at the mid-plane. The red lines denote the location where $\langle C_f \rangle = 0$, i.e., separation and reattachment locations; the blue lines denote the location where maximum pressure fluctuation appears.

4.3. LOW-FREQUENCY DYNAMICS

It is well known that STBLI are subject to large-scale low-frequency oscillations (Clemens and Narayanaswamy, 2014). The streamwise distribution of the wall-pressure fluctuations indicated that streamwise-aligned ridges with a small ridge spacing ($D/\delta_0 = 0.25$) may be effective in attenuating the low-frequency motion of the separation shock. To further support this claim, we analyze the unsteady pressure probe data and perform a modal analysis of the flow field.

4.3.1. SPECTRAL ANALYSIS

We place 282 equally spaced pressure probes ($\Delta/\delta_0 \approx 0.09$) along the streamwise direction at $y = 0$ in the mid-plane, as indicated by the red dotted line in Figure 4.1(a), and samples have been collected over a time span around 4000 δ_0/u_∞ with a sampling frequency of $f_s \approx 46 u_\infty/\delta_0$. This theoretically enables us to capture the flow unsteadiness within a very wide frequency range from 2.5×10^{-4} u_∞/δ_0 to 23 u_∞/δ_0. We employ Welch's method described in Section 2.2.2 to compute the PSD to achieve statistical convergence so that each time window has a length of $889\delta_0/u_\infty$. The corresponding frequency range is $1.12 \times 10^{-3} u_\infty/\delta_0$ to $23 u_\infty/\delta_0$.

The separation length is selected as the characteristic length scale to define the Strouhal number $St_{L_{sep}} = fL_{sep}/u_\infty$. Figure 4.15 shows the pre-multiplied power spectral density (PSD) of the wall-pressure signals. PSDs are shown in absolute value to directly reflect the pressure fluctuation strength.

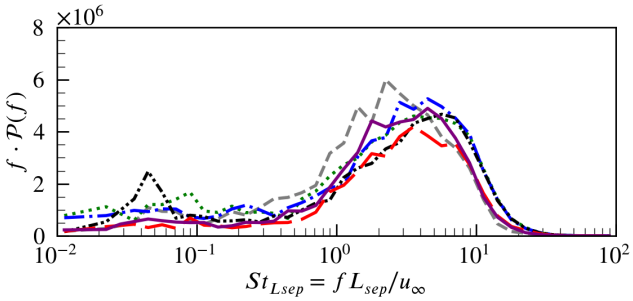

Figure 4.16: Pre-multiplied power spectral density of wall-pressure signals at the location of maximum pressure fluctuation. Line legends: ---- smooth wall; ····· $D/\delta_0 = 2.0$; -·-· $D/\delta_0 = 1.0$; -··-·· $D/\delta_0 = 0.5$; — — $D/\delta_0 = 0.25$; — $D/\delta_0 = 0.125$.

The PSDs of the upstream TBL in all cases show high amplitudes centered around $fL_{sep}/u_\infty \approx 10$, which reflects the characteristic frequency of the turbulent boundary layer. Near the location of the separation line, an energetic low-frequency tone appears, approximately two orders of magnitude lower than the characteristic frequency in the upstream TBL. Because of the diffused character of the separation shock for the low Reynolds number case, the low-frequency content spreads over around two boundary layer thicknesses in the streamwise direction. Correspondingly, the intensity is lower than typically observed in higher Reynolds number impinging STBLI (Pasquariello et al., 2017; Dupont et al., 2006). Comparing the smooth case with the rough cases, we observe that the low-frequency content for the three cases with the relatively large ridge spacing ($D/\delta_0 = 2.0, 1.0, 0.5$) is similar to the smooth-wall case, but it appears significantly weaker for $D/\delta_0 = 0.25$ and 0.125.

Figure 4.15 also indicates that the location of low-frequency content appears near the separation point but does not necessarily coincide with the maximum pressure fluctuation point. The maximum pressure fluctuation appears downstream of the separation points, where the local pressure is mostly influenced by the detached shear layer vortices.

To better compare the spectral characteristics at the location of maximum wall-pressure fluctuation, the spectral content of all investigated cases is shown in Figure 4.16. All cases exhibit pronounced high-frequency content with $St_{L_{sep}} \geq 0.4$, which is associated with the amplification of turbulence in the separated shear layer. For cases with relatively small ridge spacing, such as $D/\delta_0 = 0.25, 0.125$, both the high-frequency component and the low-frequency component with a characteristic frequency of $St_{L_{sep}} \approx 0.05$ are significantly attenuated. This simultaneous reduction suggests that the ridge-type roughness mitigates not only the turbulence amplification within the shear layer but also the large-scale unsteadiness of the separation shock. In contrast, for cases with relatively large ridge spacing, the low-frequency content remains comparable to that of the smooth-wall case or even increases, such as in $D/\delta_0 = 0.5$. This behavior is consistent with the larger peak wall-pressure gradient observed in these cases in Figure 4.11, indicating a sharper separation shock and enhanced low-frequency shock-foot motion, which leaves a stronger footprint on the wall-pressure spectrum.

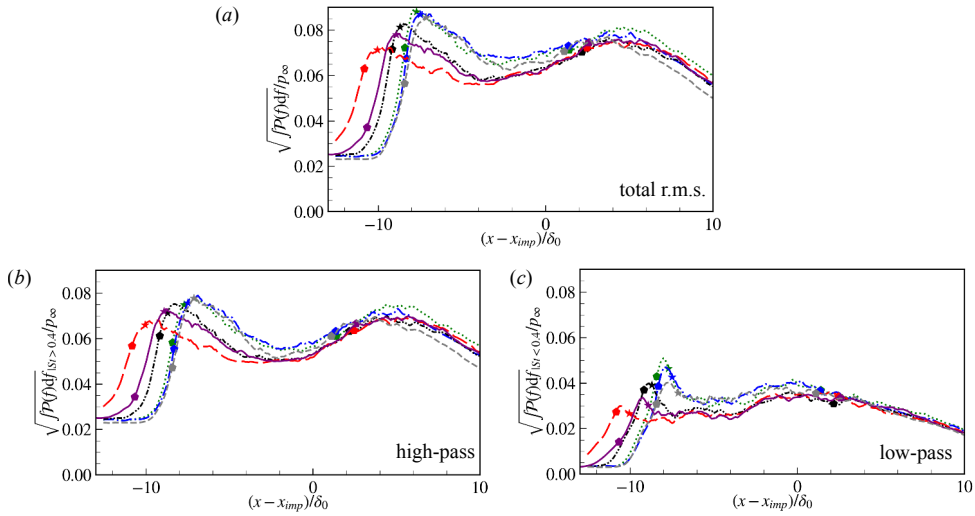

Figure 4.17: (a) Wall-pressure fluctuation obtained by integrating the power spectral density, (b) wall-pressure fluctuation attributed to the high-frequency content ($St_{L_{sep}} > 0.4$), and (c) wall-pressure fluctuation attributed to the high-frequency content ($St_{L_{sep}} < 0.4$). Line legends: ---- smooth wall; ····· $D/\delta_0 = 2.0$; -·-· $D/\delta_0 = 1.0$; -··-·· $D/\delta_0 = 0.5$; — — $D/\delta_0 = 0.25$; —— $D/\delta_0 = 0.125$.

The filtered wall-pressure signals obtained from numerical probes located at the ridge are presented in Figure 4.17 to elucidate the contributions of the low- and high-frequency components. The total wall-pressure fluctuation, computed by integrating the power spectral density, is shown in Figure 4.17(a), where the cut-off frequency separating the low- and high-frequency components is set to $St_{L_{sep}} = 0.4$. As can be seen, the resulting distribution agrees well with the spanwise-averaged $\sqrt{\langle p'p' \rangle}/p_\infty$ shown in Figure 4.11(c), apart from minor statistical noise. Figures 4.17(b) and (c) present the streamwise distributions of wall-pressure fluctuations associated with the high- and low-frequency components, respectively. Compared with the smooth-wall case, the two cases with relatively large ridge spacing ($D/\delta_0 = 2.0$ and 1.0), which also exhibit higher peak pressure fluctuations, show a similar high-frequency pressure-fluctuation distribution near the separation shock foot, but a pronounced increase in the low-frequency pressure-fluctuation peak. Similar observations have also been reported by Guo et al. (2022b) and Della Posta et al. (2024), where passive control energizes the upstream turbulent boundary layer of STBLI and leads to stronger, particularly low-frequency, wall-pressure fluctuations. This observation indicates that the elevated pressure-fluctuation levels in these cases mainly originate from the enhancement of the low-frequency component. In contrast, the case with the smallest ridge spacing ($D/\delta_0 = 0.25$) exhibits a significant attenuation of both the high- and low-frequency pressure-fluctuation components.

4.3.2. DYNAMIC MODE DECOMPOSITION

To better decouple different frequency dynamics and further validate our previous findings, a modal analysis was carried out based on Sparsity Promoting Dynamic Mode De-

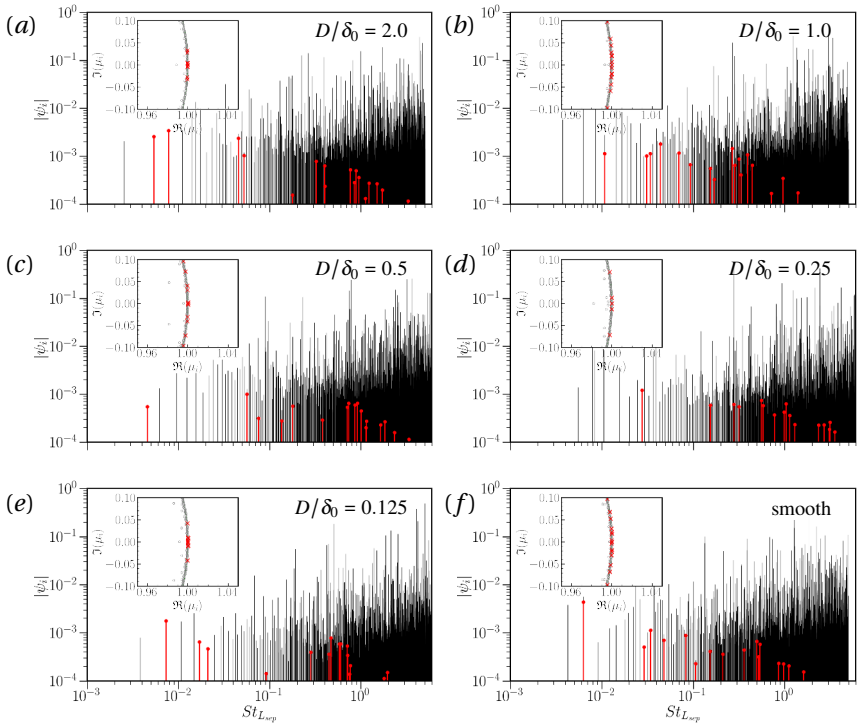

Figure 4.18: Normalized amplitudes (black lines) of the DMD modes from the rough wall cases. The close-up view shows the eigenvalue distribution. The red color indicates a SPDMD subset of N_{sub} = 17 modes.

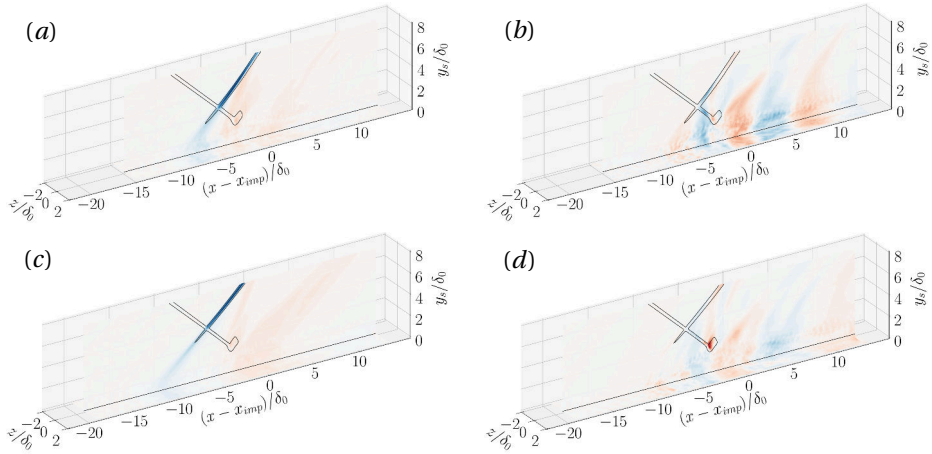

Figure 4.19: Real part of selected mode $\Re(\phi_p)$ at (a) $St_{L_{sep}} = 0.034$ (b) $St_{L_{sep}} = 0.537$ of smooth wall, (c) $St_{L_{sep}} = 0.028$ (d) $St_{L_{sep}} = 0.556$ of $D/\delta_0 = 0.25$ case at initial phase. The mean shock system is superimposed by black solid lines.

composition (SPDMD). Dynamic Mode Decomposition (DMD) (Schmid, 2010) is a purely data-driven decomposition technique that aims to extract coherent spatial-temporal structures from a sequence of snapshots. SPDMD is a variant of DMD that significantly simplifies the analysis and interpretation by automatically selecting the most relevant modes from the standard DMD solution (Jovanović et al., 2014). We apply SPDMD to 4101 2D snapshots of the pressure field at the $z = 0$ and $y = 0$ planes covering a time interval of $tu_\infty/\delta_0 = 3997.5$ at a sampling frequency of $f_s\delta_0/u_\infty \approx 1$ to conduct SPDMD. The corresponding frequency resolution range is $2.5 \times 10^{-4} < St_{\delta_0} < 0.5$.

The mode amplitudes ψ_i, which are normalized by the mean mode amplitude, from the DMD analysis are shown in Figure 4.18 supplemented by a close-up view of eigenvalues μ_i distribution. Since the input data is real-valued, modes appear as complex conjugate pairs but only the ones in the positive branch are shown here. SPDMD effectively selects modes that represent the dynamics at low and medium frequencies; modes selected by SPDMD are colored in red in Figure 4.18. The distribution of the SPDMD selected modes indicates that case $D/\delta_0 = 0.25$ shows attenuated low-frequency unsteadiness. Only one mode with $St_{L_{sep}} < 0.1$ is selected by SPDMD for this case.

Figure 4.19 shows the mode shape of selected low-frequency and high-frequency modes for the smooth-wall case (upper row) and for case $D/\delta_0 = 0.25$ (lower row). Representative low-frequency modes from the smooth-wall and rough-wall case are shown in the left column, Figure 4.19(a,c), and clearly represent the motion of the separation shock. The impinging shock is steady and does not cause any fluctuation. The slightly less pronounced separation shock motion observed for case $D/\delta_0 = 0.25$ is consistent with previous conclusions drawn from the wall-pressure fluctuations in Figure 4.10. We also see that the shock-motion induced pressure fluctuation gradually diffuses when approaching the wall. The high-frequency modes shown in Figure 4.19(b) and (d) primarily show pressure fluctuation caused by the shedding of shear-layer vortices. These

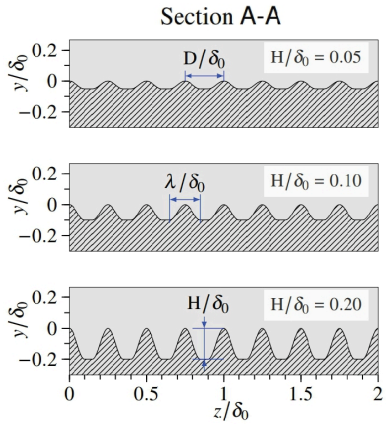

Figure 4.20: Schematic view of the investigated ridge-type rough walls with different ridge heights.

fluctuations propagate further downstream and persist even after the interaction region.

4.4. EFFECTS OF RIDGE HEIGHT

From the previous study about the effects of ridge spacing, it is known that ridge-type roughness with relatively small ridge spacing reduces the wall-pressure fluctuation peak near the separation line despite the enlarged separation bubble (Wu et al., 2025b). The reduced pressure fluctuation peak is related to a more smeared separation shock foot. The height of the ridges has not been varied in previous studies. However, it is reasonable to assume that the ridge height directly affects the size of the subsonic part of the turbulent boundary layer, and thus the formation of isentropic compression waves at the separation and their coalescence into the separation shock. This section investigates the influence of ridge height on STBLI, employing the same numerical setup described in Section 4.1 but with the ridge height as the sole variable, namely, from $0.05\delta_0$ to $0.20\delta_0$. The cross-sections of the investigated rough walls are shown in Figure 4.20.

4.4.1. UPSTREAM TURBULENT BOUNDARY LAYER

Similarly, a probing station located $20\delta_0$ upstream of the impingement point is used to examine the state of the incoming TBL. The origin of the wall-normal coordinate is shifted to the mean roughness-crest elevation relative to the valley of the rough wall, as described in detail in Section 4.2.1. A comparison of the van Driest transformed mean velocity profiles is given in Figure 4.21. A clear downshift of the profiles is observed for all rough-wall cases, which indicates a drag increase and the corresponding momentum deficit due to the surface roughness. This can be quantified with the roughness function $\Delta\langle u\rangle^+_{vD} = \langle u\rangle^+_{vD,S} - \langle u\rangle^+_{vD,R}$, where $\langle u\rangle^+_{vD,S}$ and $\langle u\rangle^+_{vD,R}$ represent the velocity profile over the smooth wall and the rough wall, respectively. Figure 4.21(b) shows that $\Delta\langle u\rangle^+_{vD}$ increases monotonically when the ridge height H/δ_0 increases.

Velocity vectors and vertical velocity contours visualize the roughness-induced stream-

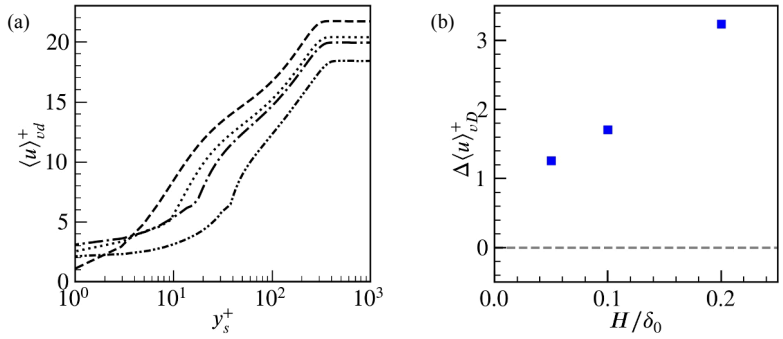

Figure 4.21: (a) van Driest transformed velocity profiles of the incoming TBL for ---- smooth wall; ····· $H/\delta_0 = 0.05$; -·-·- $H/\delta_0 = 0.10$; -··-·· $H/\delta_0 = 0.20$. (b) Roughness function.

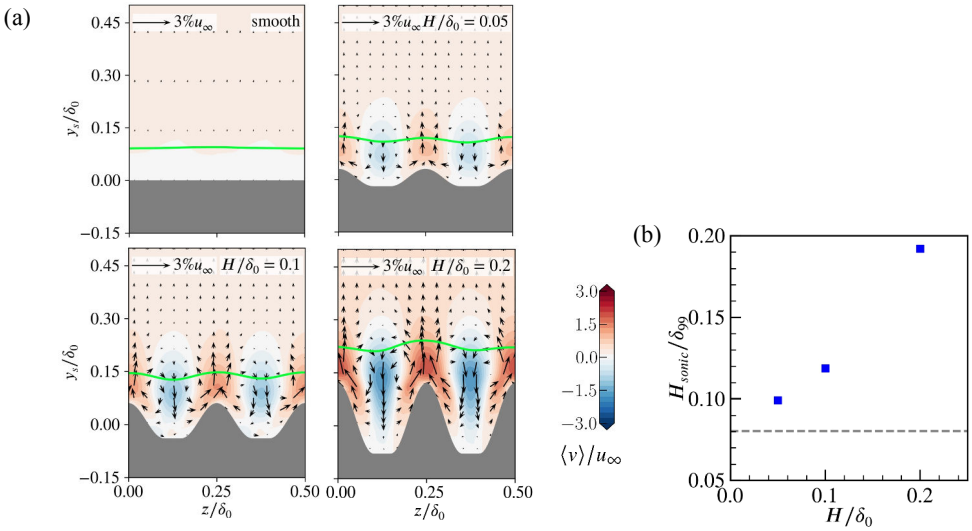

Figure 4.22: (a) Vertical velocity in a cross-stream plane with superposed cross-stream velocity vectors. The solid line shows the sonic line. (b) Spanwise-averaged height of the mean sonic line.

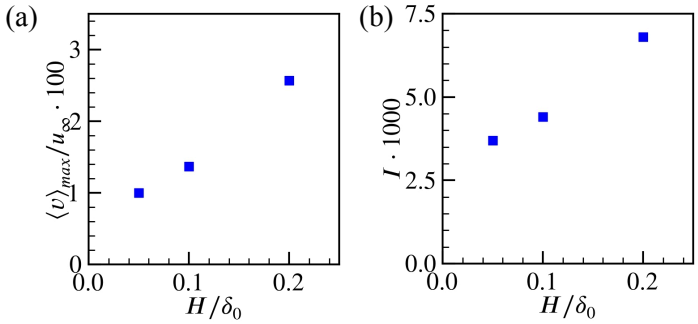

Figure 4.23: (a)Maximum induced vertical velocity and (b) secondary flow intensity as a function of ridge height H/δ_0

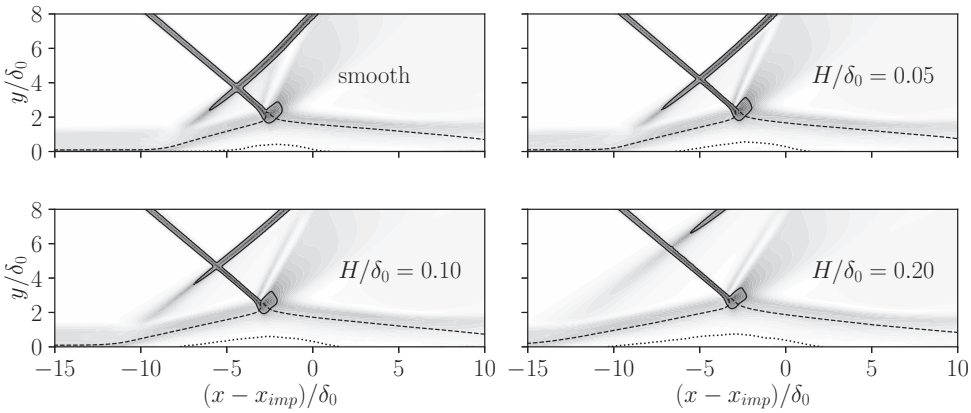

Figure 4.24: Numerical schlieren of the mean flow field on the $z = 0$ plane. —— mean shock position, - - - - mean sonic line, ····· separation line.

wise vortices in Figure 4.22(a). Upwash occurs at the ridges while downwash happens in the valleys. The intensity of the induced secondary flow can be quantified either by the maximum value of the induced vertical velocity or by the parameter I defined in Equation 3.1. Both metrics consistently show an almost linear increase with ridge height, indicating that taller ridges promote stronger cross-stream motion and more pronounced redistribution of momentum within the turbulent boundary layer.

From figure 4.22(a), it can also be observed that the sonic line remains approximately $0.1\delta_0$ above the roughness crest. As a result, the subsonic portion of the boundary layer increases with ridge height. The growth of this subsonic region in the upstream turbulent boundary layer is quantified by the spanwise-averaged elevation of the sonic line in the shifted wall-normal coordinate, as shown in figure 4.22(b).

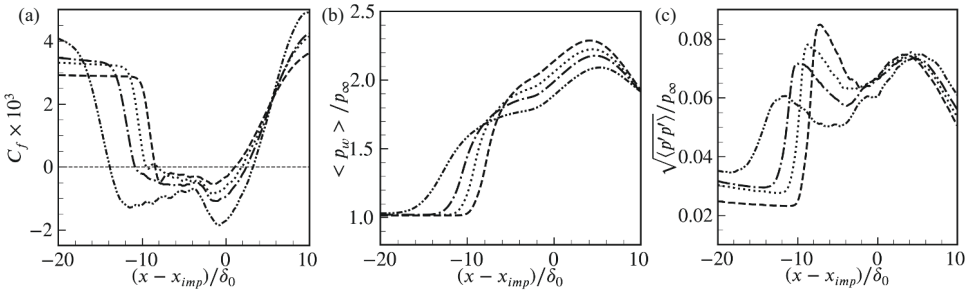

Figure 4.25: Spanwise averaged (a) friction coefficient (b) wall-pressure, and (c) wall-pressure fluctuations for: - - - smooth wall; ····· $H/\delta_0 = 0.05$; -·-·- $H/\delta_0 = 0.10$; -··-·· $H/\delta_0 = 0.20$.

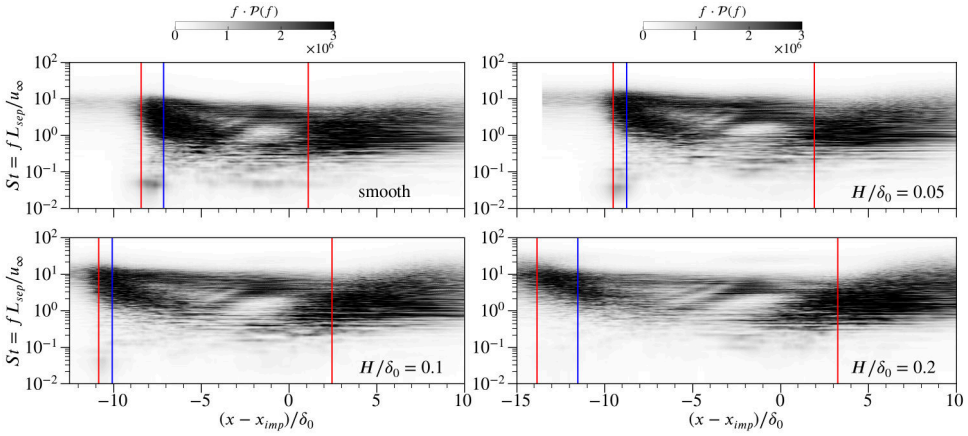

Figure 4.26: Pre-multiplied power spectra density maps of wall-pressure signals at the mid-plane. The red lines denote $\langle C_f \rangle = 0$; the blue lines denote the location of maximum pressure fluctuation.

4.4.2. INTERACTION REGION

Figure 4.24 shows a numerical schlieren visualization of the mean flow field on the $z = 0$ plane. It is noticeable that the separation bubble significantly increases with the increasing ridge height. As the ridge height increases, the separation shock moves further upstream and its foot becomes more diffused, causing the shock to form further from the wall. Spanwise average friction coefficient, wall-pressure, and wall-pressure fluctuation for all cases are presented in Figure 4.25. Friction coefficient distribution indicates that the mean separation region expands with the ridge height. The maximum value of wall-pressure decreases and the interaction onset location moves more upstream with increasing ridge height, which results in a more gradual compression. More interestingly, the peak value of pressure fluctuations near the separation point drops as the ridge height increases but the pressure fluctuations upstream of the interaction region increase.

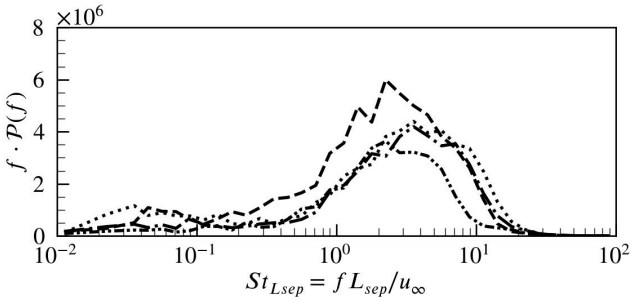

Figure 4.27: Pre-multiplied power spectral density of wall-pressure signals at the location of maximum pressure fluctuation. Line legends: ---- smooth wall; ····· $H/\delta_0 = 0.05$; —·— $H/\delta_0 = 0.10$; -··-·· $H/\delta_0 = 0.20$.

4.4.3. SPECTRAL ANALYSIS

The streamwise distribution of wall-pressure fluctuations suggests that the investigated rough walls are effective in attenuating the low-frequency motion of the separation shock. To further substantiate this observation, pressure signals from 282 numerical probes placed at $y = 0$ along the mid-plane are analyzed, as indicated by the dotted line in Figure 4.1(a). The pre-multiplied power spectral density (PSD) map of the smooth-wall case (Figure 4.26) reveals a pronounced low-frequency component near the separation line at $St_{L_{sep}} \approx 0.05$, which is characteristic of the low-frequency unsteadiness in STBLI. With increasing ridge height, this low-frequency content is progressively attenuated and completely suppressed in the case with $H/\delta_0 = 0.2$, highlighting the effectiveness of ridge-type roughness in mitigating separation-shock unsteadiness.

In addition, the spectra at the locations of maximum wall-pressure fluctuation are examined in Figure 4.27. Since these locations are situated slightly downstream of the dominant low-frequency region, no pronounced low-frequency peak is observed in the corresponding spectra. Nevertheless, compared with the smooth-wall case, all rough-wall configurations exhibit a clear attenuation in the high-frequency range, which accounts for the reduced peak values of wall-pressure fluctuation.

Overall, ridge-type roughness with larger ridge height effectively suppresses both the low-frequency and high-frequency components of wall-pressure fluctuations in the vicinity of the separation shock foot.

4.5. CONCLUSION

In this chapter, the effects of spanwise heterogeneous roughness on the interaction between an impinging shock wave and a turbulent boundary layer at Mach 2.0 and $Re_\tau \approx 355$ are investigated. The structured roughness pattern consists of streamwise-aligned ridges that generate secondary flows of Prandtl's second kind. Two geometric parameters of the ridge-type roughness are examined, namely the ridge spacing and ridge height.

Regarding the effects of ridge spacing with a fixed ridge height of $H/\delta_0 = 0.1$, it is found that both the size and intensity of the induced streamwise vortices increase

with increasing non-dimensional ridge spacing and reach their maximum at $D/\delta_0 = 1.0$. Moreover, large ridge spacings ($D/\delta_0 = 1.0$ and 2.0) reduce the separation area by approximately 15% but result in stronger wall-pressure fluctuations. In contrast, a smaller spacing of $D/\delta_0 = 0.25$ enlarges the separation region and decreases the peak amplitude of pressure fluctuations by about 12% compared with the smooth-wall case. Analysis of wall-pressure spectra and dynamic mode decomposition of two-dimensional pressure fields reveals that the reduction in pressure fluctuations is associated with the attenuation of the low-frequency unsteadiness of the separation shock, as well as the reduction in the high-frequency turbulence from the shear layer.

The effects of ridge height are further examined with the ridge spacing fixed at $D/\delta_0 = 0.25$. Varying the ridge height ($H/\delta_0 = 0.05$, 0.1, and 0.2) increases the skin-friction coefficient upstream of the interaction region. Similar to the case of changing ridge spacing, the roughness generates streamwise vortices in the upstream turbulent boundary layer, with their intensity strengthening as the ridge height increases. Both the separation and interaction lengths increase with ridge height, while the peak pressure-fluctuation amplitude decreases significantly, as verified by spectral analysis.

To the best of our knowledge, this study presents the first observation that ridge-type roughness can reduce the wall-pressure fluctuation peak near the separation point. The increase in total pressure recovery further underscores the potential of ridge-type roughness for engineering applications, such as in supersonic engine inlets. This chapter provides a proof-of-concept for a relatively low Reynolds number. This observation raises the question of whether the control mechanism remains effective in high-Reynolds-number STBLI, where the separation shock is sharper and low-frequency unsteadiness is more pronounced. This issue is addressed in the next chapter.

5

EFFECTS OF REYNOLDS NUMBER

刚者易折，柔者常全。
What is hard is prone to break; what is soft endures whole.
老子/*Lao Tzu*

Parts of this chapter have been published in *J. Fluid Mech.* **1029** A51, (Wu et al., 2026).

In Chapter 4, we applied streamwise-homogeneous ridge-type roughness to impinging STBLI at Mach 2 and $Re_\tau \approx 350$ and reported two important outcomes: the ridge-type roughness with relatively large spacing reduced the shock-induced flow separation, while the ridge-type roughness with relatively small spacing alleviated the pressure fluctuation peak near the separation-shock foot. This reduction in pressure unsteadiness is of clear engineering relevance, as it suggests the potential to passively alleviate dynamic loads associated with the separation shock. However, whether the effect persists at higher Reynolds numbers remained an open question.

The objective of this chapter is to further explore the control effectiveness and the underlying mechanisms of ridge-type roughness, particularly at moderately high Reynolds numbers. To this end, two new rough-wall simulations are conducted at a friction Reynolds number of approximately 1200, based on the incoming turbulent boundary layer. The employed roughness maintains geometric similarity to a selected low Reynolds number case in Chapter 4 in outer scaling for one simulation and in inner scaling for the other. Results are compared with corresponding baseline (uncontrolled) interactions on a smooth wall. This framework allows us to isolate the effects of Reynolds number, roughness scaling, and surface condition on the STBLI flow, and to assess the efficacy of ridge-type roughness as a passive control method for massive flow separation.

5.1. FLOW CONFIGURATION AND NUMERICAL SETUP

5.1.1. FLOW CONFIGURATION

We investigate the interaction of an impinging shock with an incoming turbulent boundary layer flow as illustrated in Figure 5.1. This chapter considers five simulations: two low Reynolds number cases from the previous chapter — one with a smooth wall ($\mathcal{LS}$) and one with a rough wall ($\mathcal{LR}$) — and three moderately high Reynolds number cases, consisting of one smooth wall case ($\mathcal{HS}$) and two rough wall cases ($\mathcal{HR}1$, $\mathcal{HR}2$), which share the same roughness geometry with $\mathcal{LR}$ in outer and inner scaling, respectively.

All above simulations share identical inflow conditions as investigated in the low-Reynolds number STBLI in Chapter 4 except for the Reynolds number. The Reynolds numbers Re_{δ_0} are 11.6×10^3 and 50.1×10^3 at the inlet of the computational domain for the low and higher Reynolds number cases. The corresponding friction Reynolds numbers $Re_{\tau,0} = \delta_0/\delta_\nu$ are 250 and 935, respectively. The flow parameters are summarized in the Table 5.1.

The spanwise heterogeneous roughness consists of sinusoidal ridges defined by non-dimensional wave length λ/δ_0, height H/δ_0, and spacing D/δ_0, while the roughness remains homogeneous in the streamwise direction, see Figure 5.1(b). To systematically

Case	M_∞	T_0 [K]	p_0 [kPa]	δ_0 [mm]	ϕ	Re_{δ_0}	$Re_{\tau,0}$
Low-Re	2.0	288.2	355.6	5.2	40.04°	11.6×10^3	250
High-Re	2.0	288.2	355.6	5.2	40.04°	50.1×10^3	935

Table 5.1: Summary of flow parameters of the incoming flow.

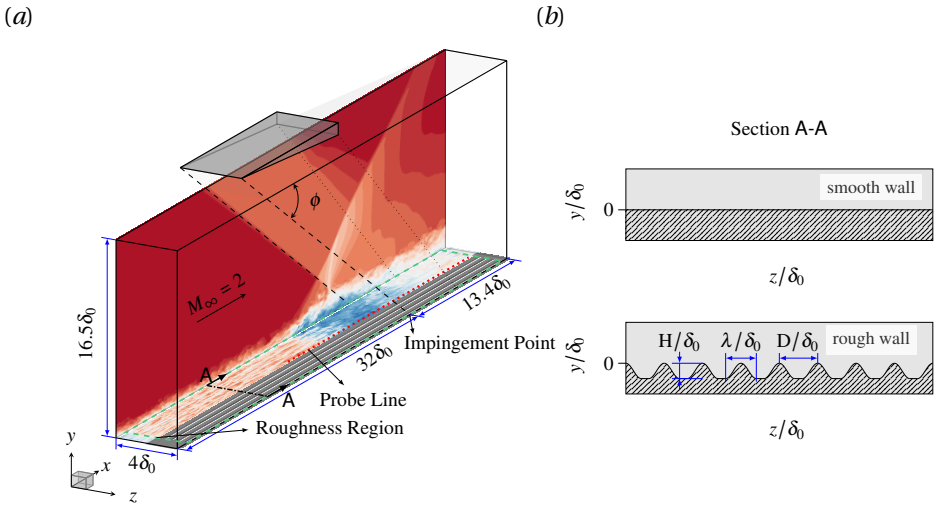

Figure 5.1: (*a*) Schematics of the computational domain (including instantaneous streamwise velocity contours), and (*b*) schematic view of the investigated ridge-type rough walls with relevant geometric definitions.

5

investigate the effect of Reynolds number, two rough walls were designed to maintain identical geometric parameters in either outer or inner scaling. In outer scaling, cases $\mathcal{LR}$ and $\mathcal{HR}1$ share identical geometric parameters: $\lambda/\delta_0 = 0.2$, $H/\delta_0 = 0.1$, and $D/\delta_0 = 0.25$. In inner scaling, cases $\mathcal{LR}$ and $\mathcal{HR}2$ have identical parameters: $\lambda^+ = \lambda/\delta_v = 49.6$, $h^+ = H/\delta_v = 24.8$, and $d^+ = D/\delta_v \approx 60$.

5.1.2. NUMERICAL SETUP

The numerical methodology follows that described in Chapter 4, including the boundary conditions and inflow generation procedure.

The computation domain is discretized by a block-structured, piecewise Cartesian grid with an equal number of cells per block but varying grid spacing. As depicted in

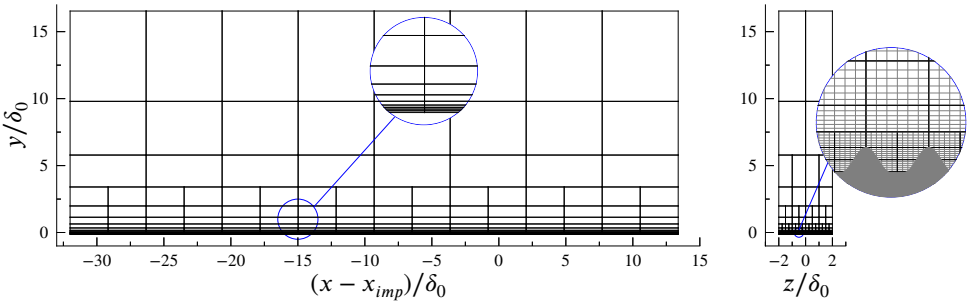

Figure 5.2: Block distribution of the numerical grid for the higher Reynolds case $\mathcal{HR}1$. In the zoom-in view of the right panel, the mesh lines are displayed in gray, with only every fourth line shown in the y- and z-directions for clarity.

Case	$\mathcal{LS}$	$\mathcal{LR}$	$\mathcal{HS}$	$\mathcal{HR}1$	$\mathcal{HR}2$
H/δ_0	-	0.10	-	0.10	0.026
h^+	-	24.8	-	93.5	24.8
λ/δ_0	-	0.2	-	0.2	0.053
λ^+	-	49.2	-	187.1	49.2
D/δ_0	-	0.25	-	0.25	0.063
d^+	-	62	-	235	59
Δx^+_{min}	21.8	5.5	39	39	39
Δy^+_{min}	0.93	0.93	0.94	0.94	0.94
Δz^+_{min}	7.7	3.9	9.8	4.9	4.9
N_x^{max}	512	2048	1088	1088	1088
N_y	192	224	240	312	312
N_z^{max}	128	256	384	768	768
$Re_{\tau,imp}$	355	355	1226	1226	1226

Table 5.2: Case-dependent roughness geometric parameters and grid resolutions.

Figure 5.2, the grid is gradually coarsened in the streamwise and spanwise directions as the distance from the wall increases. In the wall-normal direction, the mesh is progressively stretched with a very mild stretching factor of 1.02. The adequacy of the grid resolution and domain size for the two smooth wall cases was verified by Laguarda et al. (2024b) through grid- and domain-sensitivity studies. For the rough wall cases, extra layers of blocks are added to enclose the computational fluid domain below $y = 0$ and the grid is locally refined to fully resolve the geometry and turbulent structures around the roughness structure, see Figure 5.2. This mesh yields grid-converged results, as demonstrated for the most challenging case, $\mathcal{HR}2$, in Appendix A. Note that the shape of each sinusoidal ridge is well-resolved with 12 cells. The spatial resolution parameters are summarized in Table 5.2.

Other numerical methodology, including initialization from the inviscid shock-reflection solution, transient integration period, statistical averaging procedure, probe placement, and data sampling strategy, is identical to that described in Chapter 4. For brevity, these details are not repeated here.

5.2. RESULTS AND DISCUSSION

5.2.1. INCOMING TURBULENT BOUNDARY LAYER

Before examining the interaction, we first analyze the state of the incoming turbulent boundary layer upstream of the impingement point, which provides the physical basis for understanding the subsequent STBLI dynamics. A probing station is placed $20\delta_0$ upstream of the impingement point, away from the influence of downstream STBLI.

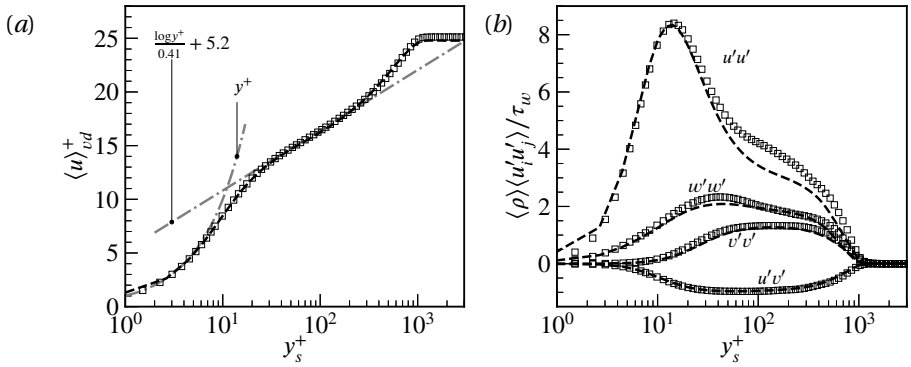

Figure 5.3: Comparison of present LES (----) for the smooth wall case and DNS (□) of Pirozzoli and Bernardini (2011): (*a*) van Driest transformed mean velocity profiles and (*b*) density-scaled Reynolds stresses at $M_\infty = 2.0$ and $Re_\tau \approx 1000$.

Additionally, this station is located $12\delta_0$ downstream of the inflow plane, ensuring that the turbulence has fully developed and reached an equilibrium state (Laguarda and Hickel, 2024a).

To better compare the characteristics of the incoming turbulent boundary layer over smooth and rough walls, the shifted wall-normal coordinate Equation 4.1 in Section 4.2.1 is again applied here. For the smooth wall cases, y_s/δ_0 reduces to y/δ_0.

Figure 5.3 shows the van Driest transformed mean streamwise velocity profile and density-scaled Reynolds stresses for the higher Reynolds number case $\mathcal{HS}$ evaluated at the streamwise location $(x - x_{imp})/\delta_0 = -20.0$, which corresponds to a friction Reynolds number $Re_\tau \approx 1000$. The DNS data of Pirozzoli and Bernardini (2011) is also included as a reference. As observed, our LES results agree with the law of wall and the reference DNS data, in both the inner layer and the log-law region. The Reynolds stresses from the current LES are also in good agreement with the reference DNS data, particularly in the region of peak streamwise stress. The slightly lower resolved Reynolds stresses in the outer layer are expected in wall-resolved LES and are consistent with the use of coarser meshes compared to the fully-resolved reference DNS. As shown in the grid-sensitivity study in Appendix A, the quantities of interest exhibit negligible dependence on grid resolution.

The time- and spanwise-averaged van Driest transformed velocity profiles of the rough walls are compared at the same probing station $(x - x_{imp})/\delta_0 = -20.0$, in Figure 5.4. Both low and higher Reynolds number cases with rough walls exhibit a profile downshift compared to their smooth wall counterparts, which indicates a drag increase and momentum deficit because of the roughness. The downshift can be quantified using the roughness function $\Delta\langle u \rangle^+_{vD} = \langle u \rangle^+_{vD,S} - \langle u \rangle^+_{vD,R}$, where $\langle u \rangle^+_{vD,S}$ and $\langle u \rangle^+_{vD,R}$ are the van Driest transformed mean velocity profiles of the smooth and rough walls, respectively (Chung et al., 2021). For $\mathcal{LR}$, $\Delta\langle u \rangle^+_{vD}$ is found to be 1.81, while $\mathcal{HR}1$ and $\mathcal{HR}2$ exhibit a larger downshift of 3.43 and 2.62, respectively. Consistent values of the roughness function are obtained when the velocity profiles are evaluated separately at ridge and valley locations, as shown in Figure 5.5. We note that the wall-normal coordinate is not shifted here. The profiles collapse well from the logarithmic region outward, demonstrat-

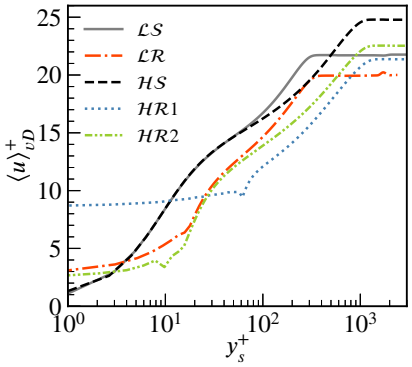

Figure 5.4: van Driest transformed velocity profiles of the incoming turbulent boundary layers of all the cases.

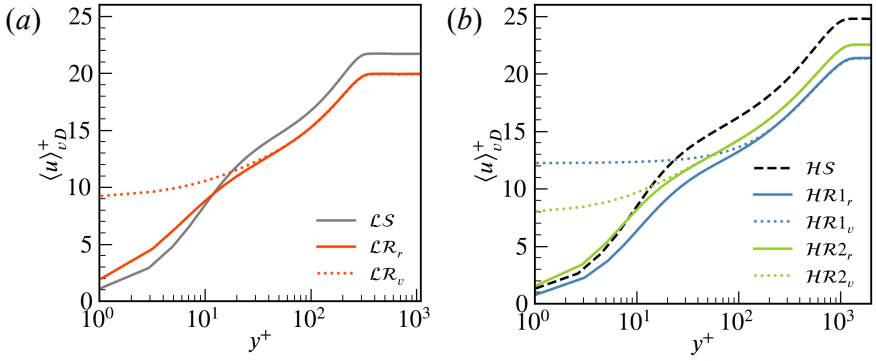

Figure 5.5: Comparison of upstream boundary-layer velocity profiles at the ridge and valley locations for (a) low Reynolds number cases and (b) high Reynolds number cases. Subscripts in the legend indicate ridge (r) and valley (v).

Case	$\mathcal{LS}$	$\mathcal{LR}$	$\mathcal{HS}$	$\mathcal{HR}1$	$\mathcal{HR}2$
H	3.02	3.49	2.97	3.24	3.02
$\Delta\langle u\rangle^+_{vD}$	–	1.81	–	3.43	2.62
$\langle C_f\rangle \times 10^3$	2.92	3.47	2.22	3.00	2.69
$\Delta\langle C_f\rangle/\langle C_f\rangle_s$	–	18.88%	–	34.95%	21.10%

Table 5.3: Summary of the shape factor H, roughness function, the skin-friction coefficients, and their relative changes with respect to the smooth-wall reference cases.

ing outer-layer similarity across spanwise locations. This collapse outside the log layer further indicates that the roughness function remains effectively unchanged between the ridge and valley, which is also confirmed by Wu and Christensen (2007). In all cases, the velocity at $y^+ = 1$ is noticeably higher in the valley region, owing to both the larger physical wall-normal distance and the influence of the secondary flows that transport high-momentum fluid downward into the valley.

The mean drag increase can also be quantified using the skin-friction coefficient $\langle C_f\rangle$ measured at the probing station. For the rough walls with the same geometry in inner-scaling, a drag penalty of around 20% is observed. We note that the wall shear is strongly non-uniform in the spanwise direction: the ridge crests experience locally enhanced shear, whereas the valleys exhibit reduced friction. For this reason, the spanwise-averaged skin-friction coefficient $\langle C_f\rangle$ is computed using the total shear force over the projected wall area. Because the actual wetted area of the rough wall exceeds that of the smooth wall, this definition inherently yields a larger $\langle C_f\rangle$. Thus, the increase in $\langle C_f\rangle$ should not be interpreted as a uniformly higher near-wall momentum. To further clarify this point, we examine the shape factor H based on the spanwise-averaged velocity profile. For the rough-wall cases, H is larger than in the smooth-wall baseline, consistent with a thicker boundary layer. The corresponding values, together with their relative changes compared with the smooth-wall reference cases, are listed in Table 5.3. Despite having equal wetted areas, the increase of $\Delta\langle u\rangle^+_{vD}$ in $\mathcal{HR}1$ and $\mathcal{HR}2$ indicates that the flow is more sensitive to roughness at the higher Reynolds number. It is worth noting that a small dip appears in the rough case profiles near the ridge crest, which is a consequence of intrinsic averaging. Intrinsic averaging accounts only for the fluid volume fraction of cells intersected by the geometry and inside the fluid domain, using these fractions as weights in the calculation of flow statistics. This approach results in an abrupt change in the volume fraction integral distribution, thereby causing the observed dip in the velocity profile and corresponding Reynolds stress profiles.

Density-scaled Reynolds stress profiles $\tau_{ij} = \langle\rho\rangle\langle u_i' u_j'\rangle$ for the smooth-wall and rough-wall cases are reported in Figure 5.6, where $\langle\cdot\rangle$ denotes Reynolds averaging. The Reynolds stresses are normalized by the local wall shear stress, which is calculated by integrating the wall shear stress in the spanwise direction over the wetted area and then normalizing it by the projected (planar) area. Across both Reynolds numbers, the smooth- and rough-wall cases exhibit similar Reynolds-stress distributions in the outer layer, while marked deviations appear near the wall. This behaviour is consistent with the observations of Hwang and Lee (2018) for turbulent boundary layers over ridge-type roughness. The

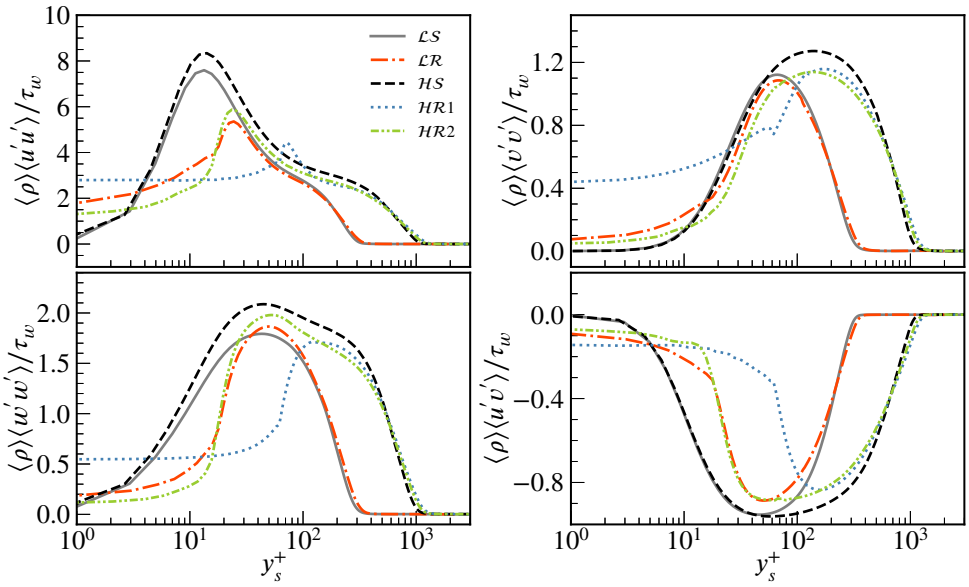

Figure 5.6: Density-scaled Reynolds stress profiles of the incoming turbulent boundary layer at $(x - x_{imp})/\delta_0 = -20.0$ for smooth wall and rough wall cases.

magnitudes of τ_{xx} and τ_{xy} peaks reduce for the rough-wall cases compared with their corresponding smooth-wall case, and their locations move away from the wall, which suggests that the rough wall may reduce the momentum transfer from the outer part of the turbulent boundary layer to the near-wall region. Profiles of $\mathcal{LR}$ and $\mathcal{HR}2$, which share the same geometric parameters in the inner scaling, agree well in the inner region (within $y_s^+ \approx 30$). This agreement suggests that the near-wall flow is primarily modulated by the wall shape in inner scaling.

The mean vertical velocity distribution, shown in Figure 5.7(a) for all cases, highlights the presence of streamwise vortices induced by the ridge-type roughness in all cases, i.e., upwash over the ridges and downwash in the valleys. This secondary flow structure is consistent with roughness-induced secondary motions previously observed in turbulent boundary layers and channel flows with ridge-type roughness (Stroh et al., 2020; Vanderwel et al., 2019; Hwang and Lee, 2018). Such secondary flows diminish for case $\mathcal{HR}2$ due to the spatial constraints imposed by the small roughness structure.

The mean streamwise velocity $\langle u \rangle$ is presented in Figure 5.7(b). Comparing $\mathcal{HS}$ with $\mathcal{LS}$, it is observed that for $\mathcal{HS}$, the high-speed flow approaches closer to the wall, and the extent of the sonic region is reduced to approximately half of that in $\mathcal{LS}$. All the rough wall cases exhibit a significantly enlarged subsonic region compared to their corresponding smooth wall counterparts. The increased subsonic height implies a thicker layer of low-speed fluid that can more effectively transmit the adverse pressure gradient upstream once the interaction sets in. As a consequence, the separation bubble that develops downstream is predisposed to extend further and become larger than in the smooth-wall baselines. In addition, the spanwise modulation associated with the ridge–valley pattern

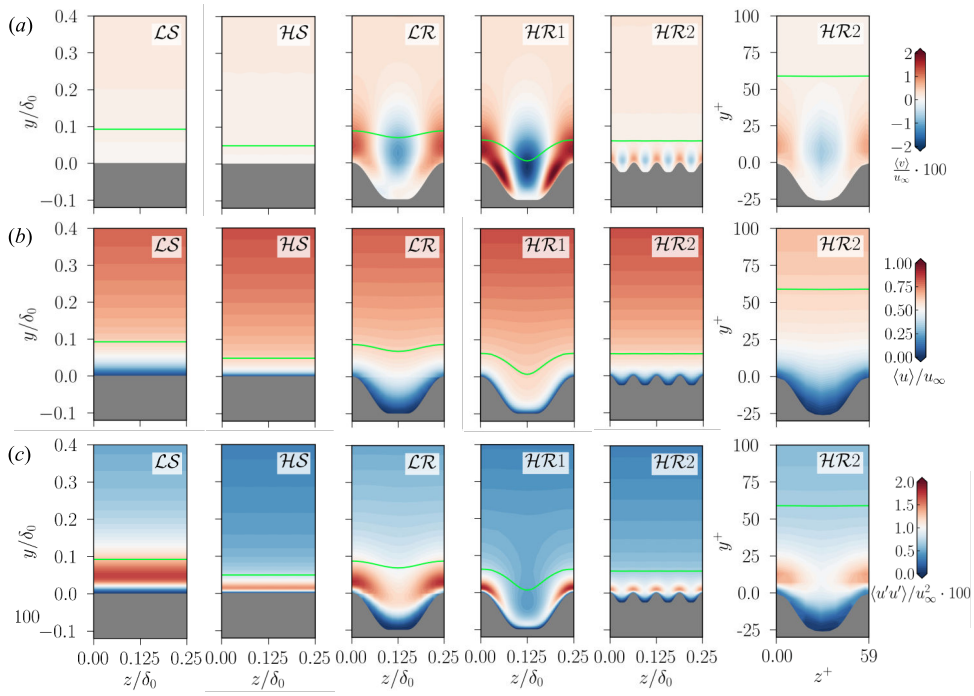

Figure 5.7: Mean flow (a) vertical velocity, (b) streamwise velocity, and (c) streamwise Reynolds stress distribution in a cross-stream plane at $(x - x_{imp})/\delta_0 = -20$. The sonic line is shown in lime. The rightmost column presents the variable distributions within one roughness unit using inner scaling for $\mathcal{HR}2$, for comparison with $\mathcal{LR}$.

generates pockets of low-momentum fluid over the valleys, which precondition the flow for a locally weaker separation shock and a reduced pressure jump at those locations once the interaction is established. These upstream modifications set the stage for the altered separation structure and shock dynamics discussed in Section 5.2.2.

Furthermore, in $\mathcal{HR}1$, the high-speed flow penetrates more deeply into the valleys between ridges than in the $\mathcal{LR}$ case, despite both sharing the same rough wall geometry in outer scaling. This behavior is attributed to a higher Reynolds number in $\mathcal{HR}1$ and the stronger downwash effect of the streamwise vortices. As a result, the sonic line in $\mathcal{HR}1$ bends more closely along the wall surface. In contrast, for $\mathcal{HR}2$, which shares the same rough wall geometry in inner scaling, the sonic line largely remains relatively straight but is displaced further from the wall compared to $\mathcal{HS}$.

The streamwise Reynolds stress, shown in Figure 5.7(c), exhibits significant spanwise variation in the rough-wall cases, with markedly reduced intensity in the valley regions. This suggests that turbulence production is suppressed in these areas, and the near-wall flow lacks sufficient momentum exchange to resist an imposed adverse pressure gradient.

5.2.2. INTERACTION REGION

Time-averaged pressure fluctuation distribution on the $z = 0$ plane is shown in Figure 5.8. The shock system, sonic lines, and zero streamwise velocity lines are superimposed on the contours to serve as a reference. The strongest pressure fluctuations are observed at two distinct locations: near the impingement point of the oblique shock on the shear layer, and in the vicinity of the separation shock, especially above the intersection between the impinging and separation shocks. The amplification of pressure fluctuations in these regions is primarily attributed to the inherent unsteadiness of the separation bubble and the low-frequency oscillations of the separation shock. It is evident that the separation shock emanates from deeper inside the incoming turbulent boundary layer for the higher Reynolds number cases. Between the two smooth-wall cases, the low Reynolds case $\mathcal{LS}$ exhibits a slightly more upstream mean separation bubble with a marginally longer separation length. In addition, the front portion of its separation bubble is significantly thinner, a feature also reported by Laguarda et al. (2024b). All rough-wall cases exhibit a larger reversed-flow bubble compared to their corresponding smooth-wall cases in the present $z = 0$ plane at the ridge-top location. Even more pronounced separation occurs in the valley regions, which will be discussed in the following section.

Time- and spanwise-averaged wall surface variables along the streamwise direction are displayed in Figure 5.9. The streamwise distributions of the mean skin-friction coefficient, in Figure 5.9(a), show an extended separation region for all rough wall cases compared to the baseline smooth wall cases, regardless of the Reynolds number. The spanwise-averaged separation and reattachment locations are reported in Table 5.4. The upstream distribution of C_f exhibits a consistent trend with the roughness function $\Delta\langle u\rangle^+_{vD}$ across all the cases.

As shown in Figure 5.9(b), for all rough-wall cases, the onset of the interaction moves upstream, accompanied by a reduction in the peak wall-pressure downstream of the reattachment point, relative to their respective baseline configurations. It is worth noting that the onset of interaction in $\mathcal{HR}1$ is located approximately $2\delta_0$ upstream of that in $\mathcal{HR}2$. This upstream shift may be attributed to two reasons. The first is the reduced and

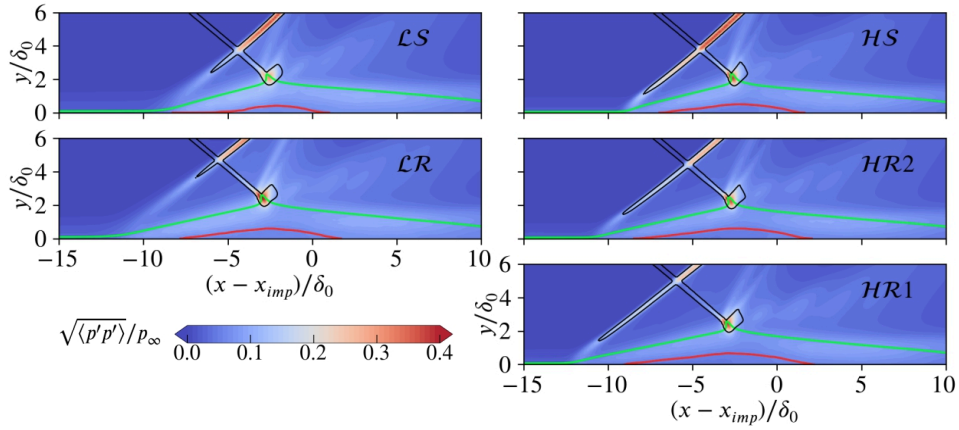

Figure 5.8: Time-averaged pressure fluctuation distribution at $z = 0$ plane. Solid line color legend: zero streamwise velocity line (red), sonic line (lime) and shock system (black).

more outward-distributed τ_{xy} peak, which weakens the momentum transfer from the outer boundary layer toward the near-wall region, thereby diminishing the flow's ability to resist separation. Second, an increase in the subsonic layer thickness leads to a longer upstream influence length, as noted by Délery and Bur (2000).

Furthermore, as shown in Figure 5.9(c), the wall-pressure fluctuation for all cases shows two peaks near the separation and reattachment points. The pressure fluctuation peak near the separation point has approximately the same value for $\mathcal{LS}$ and $\mathcal{HS}$; however, $\mathcal{HS}$ exhibits a sharper spike, because the separation-shock foot is located closer to the wall at higher Reynolds number. More interestingly, results from $\mathcal{HR}1$ and $\mathcal{HR}2$ demonstrate that ridge-type roughness can reduce the wall-pressure fluctuation peak in higher Reynolds number flows, achieving a reduction of up to 27%, which is significantly greater than that observed for the low-Reynolds case $\mathcal{LR}$. We also note that the rough-wall cases exhibit a broader region of elevated wall-pressure fluctuations than the baseline, owing to the enlarged interaction region. However, this does not necessarily indicate a detrimental effect. In practice, different control strategies prioritize different performance metrics—such as reducing peak unsteady loads, minimizing separation length, or improving mean pressure recovery—depending on the specific application. Importantly, the present roughness design achieves a substantial reduction in the peak amplitude of the wall-pressure fluctuations, which is often the most critical metric for engineering applications.

We observe that the reduction in peak pressure fluctuation is accompanied by a corresponding decrease in the peak pressure gradient in all rough-wall cases, as shown in Figure 5.9(c, d), which suggests that rough-wall configurations mitigate peak pressure fluctuations by lowering peak pressure gradients, independent of the Reynolds number. This trend is consistent with the changes in the upstream boundary-layer topology discussed in Section 5.2.1. In particular, the enlarged subsonic region and valley-induced low-momentum zones lead to a more gradual pressure rise, and consequently, a more

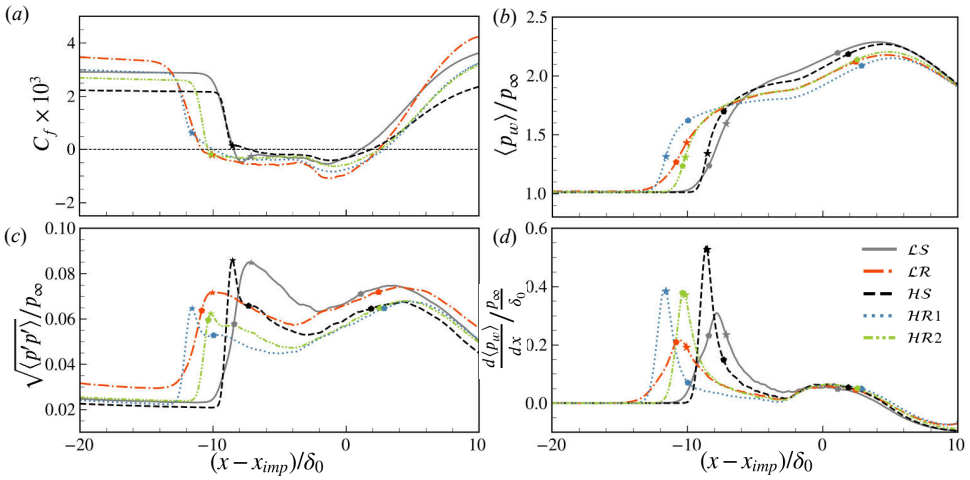

Figure 5.9: Time- and spanwise-averaged (a) friction coefficient (b) wall-pressure (c) wall-pressure fluctuation, and (d) wall-pressure gradient along the streamwise direction. Pentagon markers show the separation/reattachment location, and star markers represent the location of maximum pressure fluctuation.

5

diffused separation-shock foot. This finding also aligns with the principle proposed by Brusniak and Dolling (1994), which emphasizes that minimizing fluctuating pressure loads caused by low-frequency unsteadiness involves reducing the magnitude of the streamwise pressure gradient. Our results also reveal that the peak of wall-pressure gradient in the streamwise direction is significantly larger for higher Reynolds number cases. Of particular interest is the observation that the peak wall-pressure fluctuation coincides closely with the location of the maximum pressure gradient for these cases, see Figure 5.9(d) and Table 5.4. In contrast, for the low Reynolds number cases, the peak in pressure fluctuations is found downstream of the pressure gradient maximum. This distinction suggests that wall-pressure fluctuations are predominantly related to the shock motion at higher Reynolds numbers, whereas at low Reynolds numbers, both the shock motion as well as turbulent structures contribute significantly to the wall-pressure fluctuation peak.

The spanwise heterogeneous roughness significantly changes the distribution of the reverse-flow region as reported by Wu et al. (2025b): for large ridge spacing, the mean flow will reattach in the valley after a short secondary separation region; for the smaller ridge spacing, the flow separation starts more upstream, showing a highly corrugated mean separation line. In the present study, which employs a small ridge spacing, the spatial distribution of the skin-friction coefficient projected onto a wall-normal plane, see Figure 5.10, reveals that the separation region in the valley extends in both upstream and downstream directions, with the upstream extension being more pronounced. For $\mathcal{LR}$ and $\mathcal{HR}2$ (which share geometric parameters in inner scaling), the separation front exhibits a smoother, wider upstream protrusion in the valley region due to enhanced viscous effects near the wall. In contrast, $\mathcal{HR}1$ displays a distinctive two-spike separation front morphology, with the spikes precisely aligned at the ridge-valley corners. This

Case	$\mathcal{LS}$	$\mathcal{LR}$	$\mathcal{HS}$	$\mathcal{HR}1$	$\mathcal{HR}2$
$(x_{sep} - x_{imp})/\delta_0$	-8.42	-10.84	-7.33	-9.96	-10.36
$(x_{att} - x_{imp})/\delta_0$	1.10	2.45	1.89	2.86	2.56
$(x_{p'_{max}} - x_{imp})/\delta_0$	-7.14	-10.06	-8.53	-11.58	-10.16
$(x_{\nabla p_{max}} - x_{imp})/\delta_0$	-7.85	-10.61	-8.62	-11.70	-10.29
L_{sep}/δ_0	9.52	13.29	9.22	12.82	12.92
$A_{sep}/L_z/\delta_0$	9.47	13.43	9.20	13.31	12.82
$V_{rev}/L_z/\delta_0^2$	1.46	3.19	2.43	4.22	3.49
ϑ_{rev}	7.52°	7.36°	7.85°	6.22°	6.57°
ϑ_{def}	11.76°	10.68°	11.80°	10.47°	11.03°

Table 5.4: Summary of separation region characteristics for all cases. All locations are normalized by δ_0; x_{sep}, x_{att}, $x_{p'_{max}}$, $x_{\nabla p_{max}}$ denote the streamwise coordinates of spanwise averaged mean separation, reattachment, peak pressure fluctuation and peak pressure gradient, respectively; L_{sep}, A_{sep}, and V_{rev} are the separation length, area, and volume.

enhanced separation stems from corner flow effects: the wall shear stress diminishes on both adjacent surfaces, resulting in a less momentum-rich boundary layer in these regions. It can also be observed that in the smooth wall cases, the mean skin-friction coefficient $\langle C_f \rangle$ is homogeneous in the spanwise direction, whereas the rough wall cases exhibit pronounced spanwise heterogeneity. A high absolute value of $\langle C_f \rangle$, is observed along the ridge, where the surface protrudes into the high-speed flow. In contrast, the valley region exhibits lower absolute values of $\langle C_f \rangle$, as the flow there is decelerated by the surrounding walls.

The spatio-temporal structures of the skin-friction coefficient are presented in Figure 5.11 to examine the unsteady dynamics of the separation bubble. Figure 5.11(*a*,*b*) shows the evolution of C_f along the centreline ($z = 0$) for the smooth-wall cases at low and high Reynolds numbers. The oblique streaks observed upstream and downstream of the interaction correspond to the characteristic footprints of coherent structures in the turbulent boundary layer. The separation and reattachment lines exhibit distinctly different temporal behaviours: the separation onset undergoes a relatively small, gradual, and slowly varying streamwise excursion, whereas the reattachment point is considerably more unsteady, with larger temporal excursions and a more intermittent, higher-frequency signature. Compared with $\mathcal{LS}$, the $\mathcal{HS}$ case displays a noticeably more compact temporal pattern, leading to a smoother and better-aligned separation front. Figure 5.11(*c*,*e*,*g*) and (*d*,*f*,*h*) show the spatio-temporal variation of C_f at the ridge and valley locations for the three rough-wall cases. At the valley, C_f is consistently lower than at the ridge both upstream and downstream of the interaction region. The separation front at the ridge is more fragmented and exhibits larger streamwise excursions than that at the valley, indicating stronger temporal intermittency. In addition, the separation region at the valley extends further in both the upstream and downstream directions compared with that at the ridge, consistent with the time-averaged separation structure.

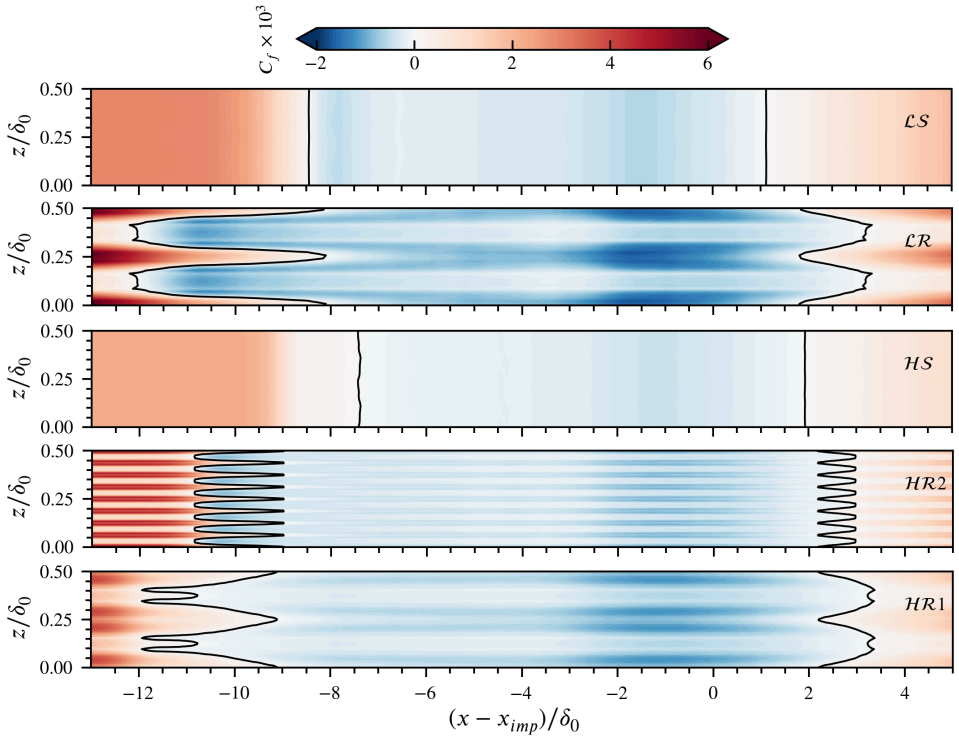

Figure 5.10: Spanwise periodical averaged local skin friction coefficient distribution projected on the horizontal plane. Black lines denote the location where $\langle C_f \rangle = 0$. Note that the spanwise (z) direction is magnified by a factor of 4 compared to the streamwise (x) direction.

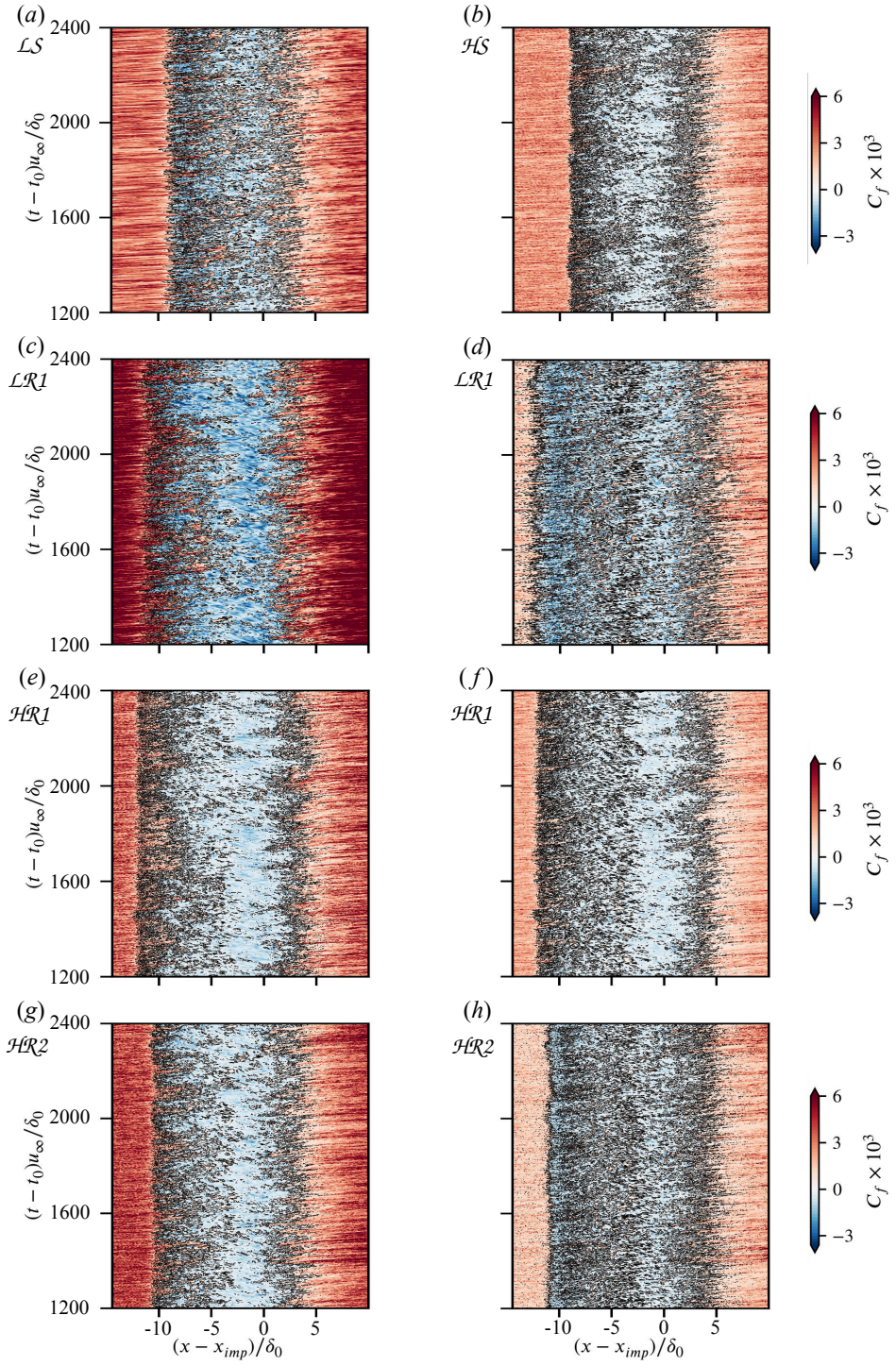

Figure 5.11: Spatio-temporal variation of C_f. (a,b) $\mathcal{LS}$ and $\mathcal{HS}$ at $z = 0$. (c,d) $\mathcal{LR}$; (e,f) $\mathcal{HR}1$; (g,h) $\mathcal{HR}2$, at ridge and valley, respectively.

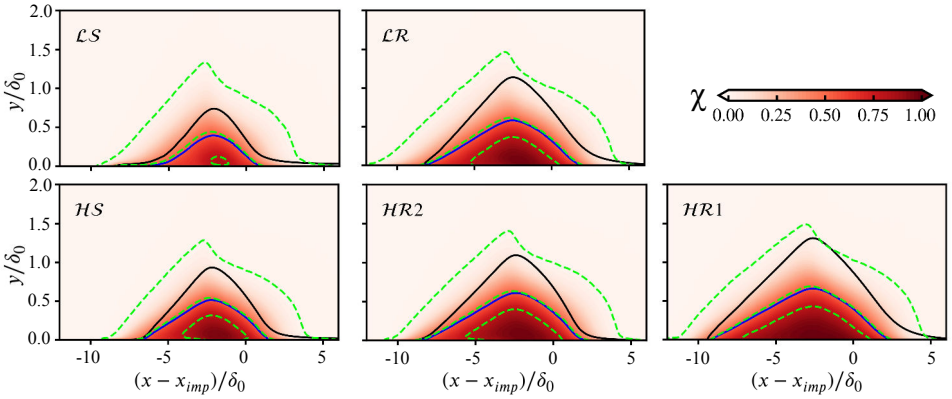

Figure 5.12: Close-up view of the probability distribution of spanwise-averaged reverse-flow region above $y = 0$. The region of mean reverse-flow is contoured by the solid blue lines, and dividing streamlines are marked with solid black lines. The green dashed lines show the isocontours of reverse-flow probability (χ=0.01,0.5 and 0.8).

5

To further elucidate the structure of the reverse-flow, we next examine the spanwise-averaged structure in the x-y plane, which reveals the internal organization of the separation bubble beyond what can be inferred from the surface-based $\langle C_f \rangle$ distributions. The mean reverse-flow region can be identified either by the condition $\langle u \rangle < 0$ or by a reverse-flow probability $\chi > 0.5$, as illustrated in Figure 5.12. The shape of the separation bubble derived from both criteria agrees well, although the latter yields a slightly larger separation volume. Interestingly, for case $\mathcal{LS}$, the separation bubble extends further upstream with a notably shallow leading edge. This observation aligns with the findings of Laguarda et al. (2024b), despite the use of an isothermal wall boundary condition in their study. The rough wall cases exhibit a significantly larger reverse-flow area on the x-y plane compared to their smooth wall counterparts. The angles of the reverse-flow front edge ϑ_{rev} and the post-shock flow deflection ϑ_{def} are summarized in Table 5.4. These angles characterize the degree of outer flow deflection and serve as indicators of separation shock strength. Notably, the separation bubble grows in size for all rough wall cases, and bubble slope and deflection of the outer flow are reduced.

5.2.3. WALL-PRESSURE FLUCTUATION

While the time-averaged flow field provides a foundational understanding of the overall interaction characteristics, it offers only a partial picture of the complex dynamics inherent to STBLI. In particular, the unsteady behavior near the separation-shock foot, marked by low-frequency shock motions and broadband fluctuations, plays a crucial role in shaping the instantaneous flow topology and directly impacts practical concerns such as aeroelasticity and structural fatigue. As highlighted by Délery and Dussauge (2009), the fluctuating nature of shock-induced interactions, despite their physical and practical significance, had long remained underexplored and only began receiving focused attention in recent decades (Dupont et al., 2006; Souverein et al., 2010; Laguarda et al., 2024b). A closer examination of these unsteady features is therefore essential for advancing both

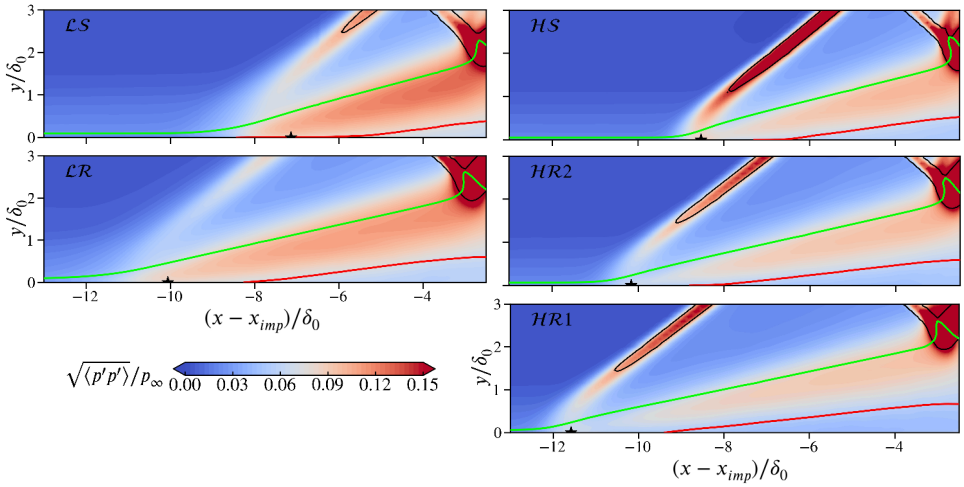

Figure 5.13: Zoom-in view of pressure fluctuation distribution near the separation shock foot and shear layer over the separation bubble. The black star denotes the location of the wall-pressure fluctuation peak near the separation shock foot. The subsonic region is indicated by the lime line, while the reversed-flow bubble is marked with a red line.

physical insight and predictive capability.

The spanwise-averaged pressure fluctuation field in the vicinity of the separation-shock foot is shown in Figure 5.13. While previous observations based on Figure 5.8 indicate that the strongest pressure fluctuations occur near the apex of the separated shear layer and along the separation shock above the intersection point between the impinging and separation shocks, these disturbances are predominantly confined to the outer part of the interaction region and have limited impact on the wall. As shown in Figure 5.13, the two main contributors of pressure fluctuation at the separation shock foot can be identified as the shock unsteadiness and shear layer dynamics for both low and higher Reynolds cases. As discussed in Figure 5.2.2, the wall-pressure fluctuation peak coincides with the wall-pressure gradient peak for the higher Reynolds cases and is closely associated with the shock motion. We find that the wall-pressure fluctuation peak is directly beneath the separation-shock foot in higher Reynolds flows. However, in low Reynolds cases, the pressure fluctuation around the separation shock foot is smeared out quickly when approaching the wall, while the pressure fluctuation coming from the detached shear layer is stronger; thus, the location of the wall-pressure fluctuation peak falls downstream of the separation shock foot.

The spatio-temporal variation of wall-pressure and wall-pressure fluctuations is shown in Figure 5.14. Comparing the smooth- and rough-wall cases, it is evident that the rough-wall configurations exhibit a more gradual pressure rise at the shock foot, consistent with the weakened separation shock. The wall-pressure fluctuations at $z = 0$ (ridge), shown in the middle column of Figure 5.14, reveal the clear footprint of the low-frequency shock motion, characterised by large alternating positive and negative excursions in time near the separation shock foot. The magnitude of these fluctuations is noticeably smaller

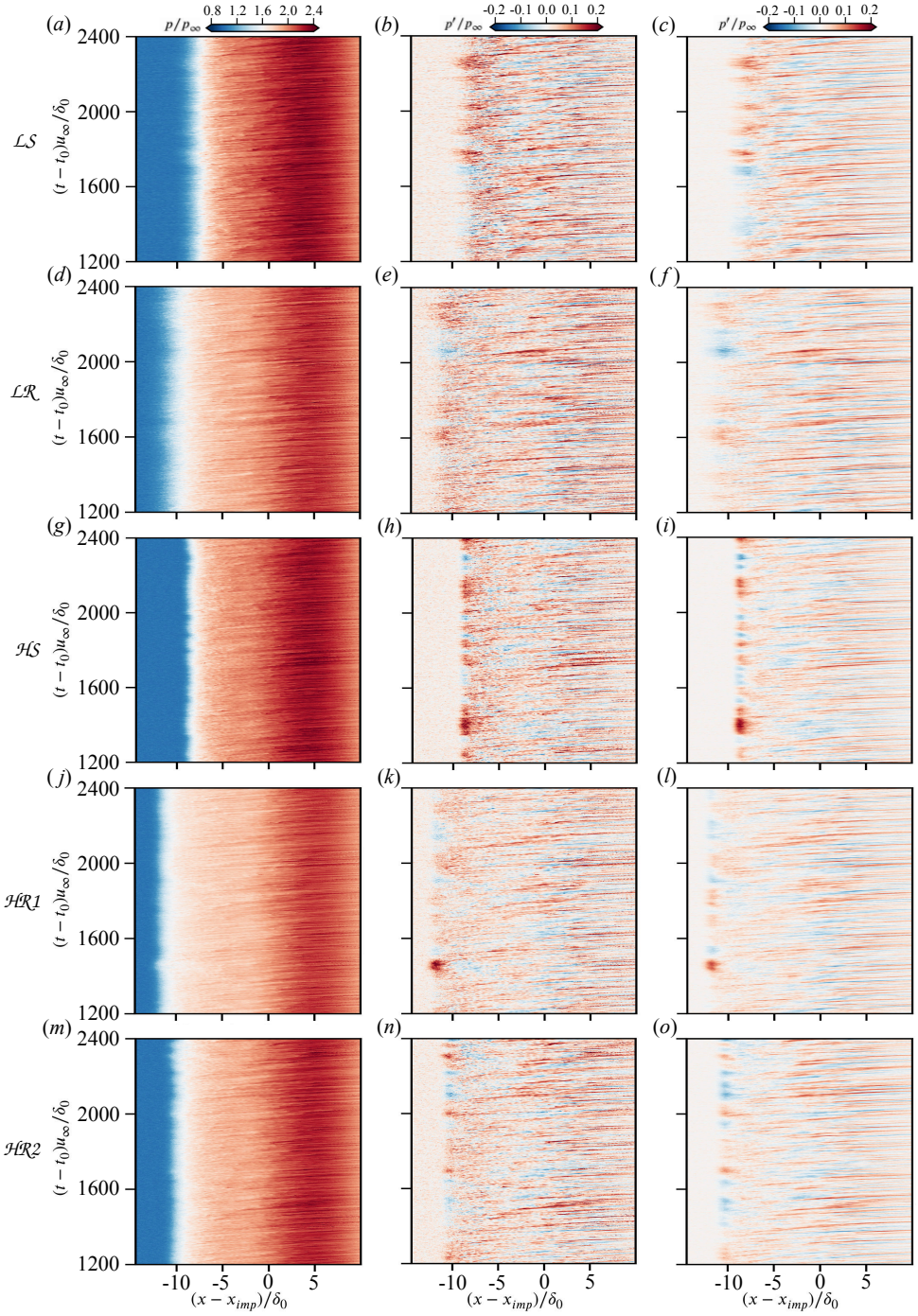

Figure 5.14: Spatio-temporal variation of wall-pressure and wall-pressure fluctuation. Left column: instantaneous wall-pressure signals at $z = 0$; middle column: wall-pressure fluctuations at $z = 0$; right column: spanwise-averaged wall-pressure fluctuations for (a,b,c) $\mathcal{LS}$, (d,e,f) $\mathcal{LR}$, (g,h,i) $\mathcal{HS}$, (j,k,l) $\mathcal{HR}1$, and (m,n,o) $\mathcal{HR}2$.

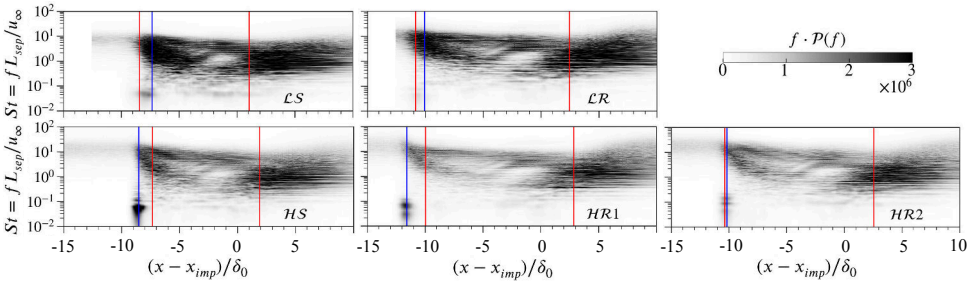

Figure 5.15: Pre-multiplied power spectral density maps of wall-pressure signals along the center line. For the rough-wall cases, this corresponds to the ridge crest. The red lines denote the separation and reattachment locations, while the blue lines indicate the location of maximum pressure fluctuation.

for the rough-wall cases than for their smooth-wall counterparts, reflecting the suppression of shock strength by the spanwise heterogeneity. The higher-Reynolds-number cases exhibit a sharper and shorter streamwise footprint of these fluctuations compared to that in low-Reynolds-number cases, due to the more abrupt pressure jump associated with a fuller incoming boundary layer. Downstream of the shock foot, thin alternating bands of positive and negative fluctuations are observed; these structures correspond to the advective footprints of pressure disturbances generated by vortical shedding from the separated shear layer. The right column presents the spanwise-averaged results, in which the large-scale patterns appear clearer and less contaminated by local spanwise variation.

To complement the spatial analysis, the frequency characteristics of the wall-pressure fluctuations are investigated via spectral analysis. Pre-multiplied power spectral density maps of wall-pressure signals collected at the ridge crest in the mid-plane show significantly stronger low-frequency content for the higher Reynolds cases, see Figure 5.15. Similar to how $\mathcal{LR}$ attenuates the low-frequency content in low Reynolds STBLI flows, rough walls in higher Reynolds interactions, especially $\mathcal{HR}2$, exhibit attenuated low-frequency content near $St_{Lsep} = 0.05$, the characteristic frequency of the low-frequency unsteadiness in STBLIs. We also notice that the wall-pressure fluctuation peak is located a bit downstream of the low-frequency content peak and overlaps with the location of strong high-frequency content in low Reynolds number cases, which is consistent with the results shown in Figure 5.13. On the other hand, the low-frequency content predominantly coincides with the peak wall-pressure fluctuation region for the higher Reynolds cases.

To better quantify the reduction across different frequency components, we examine the pre-multiplied spectra at the position of maximum wall-pressure fluctuation for all the cases, as shown in Figure 5.16. As expected, there are two clearly distinct contributors in the frequency domain, the low-frequency content with $St_{Lsep} \leq 0.4$ and the high-frequency content with $St_{Lsep} > 0.4$.

The peak of the high-frequency content in the higher–Reynolds-number flows occurs at $St_{L_{\text{sep}}} \approx 10$, whereas in the low-Reynolds cases the peak shifts to a lower value of about 3. This shift is associated with the fact that the location of maximum pressure fluctuation in the low-Reynolds-number flows lies further downstream relative to the onset of interac-

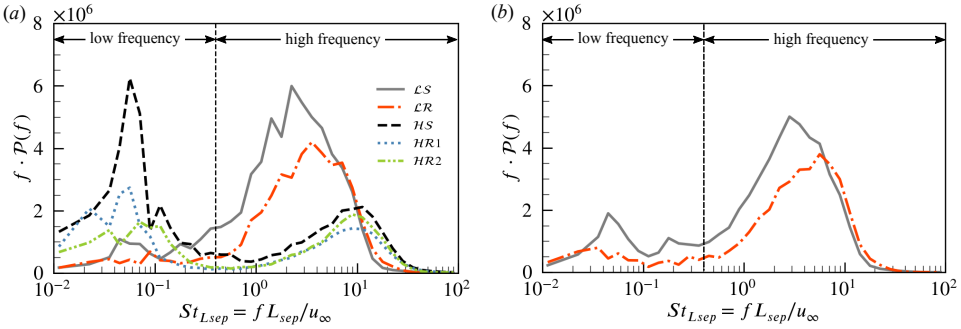

Figure 5.16: Pre-multiplied power spectral density of wall-pressure signals: (a) at the location of peak wall-pressure fluctuations; (b) at $(x - x_{imp})/\delta_0 = -7.6$ and -10.5 for $\mathcal{LS}$ and $\mathcal{LR}$, respectively.

5

tion, where the characteristic frequencies of the amplified turbulence are reduced as the shear-layer structures evolve. At the peak-pressure-fluctuation location in $\mathcal{LS}$, the high-frequency components constitute the primary contribution, while the low-frequency motions play only a secondary role. The $\mathcal{LR}$ configuration diminishes energy across the entire spectrum, with the most significant reduction occurring in the high-frequency range. It is worth noting that the peak of the low-frequency content in both $\mathcal{LS}$ and $\mathcal{LR}$ does not coincide with the location of the maximum pressure fluctuation, but instead occurs slightly upstream, at $(x - x_{imp})/\delta_0 = -7.6$ and -10.5, respectively. Accordingly, the spectra at these upstream locations are shown in Figure 5.16(b), demonstrating a clear suppression of the low-frequency peak at $St_{L_{sep}} \approx 0.05$ in $\mathcal{LR}$, together with a reduction of spectral energy across the entire frequency range. For the higher–Reynolds-number cases, it is evident from Figure 5.16(a) that $\mathcal{HS}$ exhibits the strongest low-frequency peak. The introduction of spanwise heterogeneity reduces this component substantially: $\mathcal{HR}1$ weakens the peak noticeably, and $\mathcal{HR}2$ suppresses it to less than one third of its original magnitude in $\mathcal{HS}$. The two rough-wall cases also introduce a mild reduction in the high-frequency content, but its contribution remains relatively small compared with the dominant low-frequency suppression.

To elucidate the respective roles of low- and high-frequency components in wall-pressure fluctuations, and to assess the influence of ridge-type roughness, the filtered wall-pressure signals from the numerical point probes at the ridge are examined. The wall-pressure fluctuations at the valley are very similar to those at the ridge and are therefore omitted here for brevity. The wall-pressure fluctuation obtained by integrating the power spectral density function is shown in Figure 5.17(a). Since it is derived from signals at a single spanwise location ($z = 0$) without any spanwise averaging, it contains more noise than the pressure r.m.s. computed from the 3D flowfield. The ratio of spectral power in the low- to high-frequency ranges, Figure 5.17(b), shows a clear influence of Reynolds number on the spectral composition of wall-pressure fluctuations: in higher Reynolds flows, the fluctuations near the separation shock foot are dominated by low-frequency components, whereas in low Reynolds flows, high-frequency components prevail. Nevertheless, the difference in Reynolds number has a negligible impact on the spectral composition in the downstream regions of the separation-shock foot.

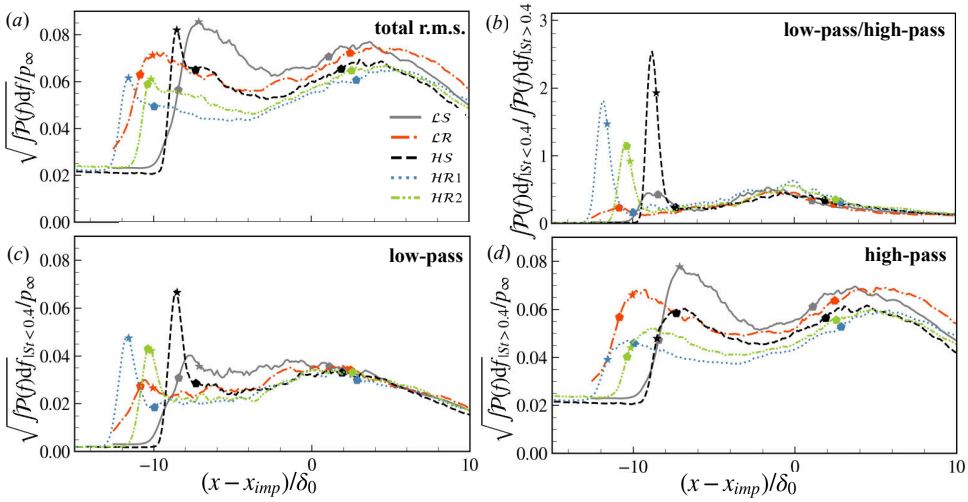

Figure 5.17: (a) Wall-pressure fluctuation obtained by integrating the power spectral density, (b) the ratio of spectral power in the low-frequency range (e.g. $St_{Lsep} < 0.4$) to that in the high-frequency range (e.g. $St_{Lsep} > 0.4$), (c) wall-pressure fluctuation attributed to the low-frequency content, and (d) wall-pressure fluctuation attributed to the high-frequency content. Wall-pressure signals are collected from the numerical probes at the ridge in the $z = 0$ plane. Pentagon markers show the spanwise-averaged separation and reattachment locations, and star markers represent the location of maximum spanwise-averaged pressure fluctuation.

The streamwise distributions of wall-pressure fluctuations attributed to the low- and high-frequency content are shown in Figure 5.17(c) and (d), respectively. Regardless of Reynolds number, both the low- and high-frequency components of wall-pressure fluctuations in rough wall cases exhibit a decrease compared to those in smooth wall cases. This attenuation is particularly pronounced in the low-frequency range for the higher Reynolds cases. For these cases, the overall peak in wall-pressure fluctuations appears in the vicinity of the low-frequency maximum, consistent with the dominant role of low-frequency dynamics near the separation shock foot. In contrast, for low-Reynolds-number flows, the peak shifts closer to the high-frequency maximum, reflecting the enhanced contribution of high-frequency components in that regime. A closer examination reveals that, for all cases, the peak of high-frequency pressure fluctuations consistently appears downstream of the low-frequency peak in the streamwise direction, which explains the observation in Figure 5.9(d) that the wall-pressure fluctuation peak is located downstream of the mean wall-pressure gradient peak in the low Reynolds cases. It is interesting to notice that, compared to $\mathcal{HR}2$, $\mathcal{HR}1$ exhibits a smaller reduction in the low-frequency components but a larger reduction in the high-frequency components. Consequently, the overall reduction in wall-pressure fluctuations is comparable between these two cases.

The analysis reveals that wall-pressure fluctuations originate from two distinct mechanisms: (1) low-frequency components associated with the separation shock motion (dominant in high-Reynolds-number flows) and (2) high-frequency components generated by shock-amplified shear-layer turbulence (governing in low-Reynolds-number regimes). Ridge-type roughness effectively attenuates both spectral components, with

particularly pronounced suppression of low-frequency wall-pressure fluctuations in the higher Reynolds conditions, demonstrating enhanced flow control efficacy at elevated Reynolds numbers.

5.2.4. LOW-FREQUENCY UNSTEADINESS

The previous analysis highlights the prominent role of low-frequency unsteadiness in wall-pressure fluctuations, especially at higher Reynolds numbers; accordingly, we now focus on the dynamics of this low-frequency unsteadiness in the higher Reynolds cases and the influence of ridge-type roughness on it.

The time variations of the reversed-flow bubble volume signals for the higher Reynolds number cases ($\mathcal{HS}$, $\mathcal{HR}1$, and $\mathcal{HR}2$) are shown in Figure 5.18(a), together with their respective spectral content in Figure 5.18(b). The bubble volume signals for these three cases all exhibit aperiodic fluctuations with a local peak in spectra around $St_{L_{sep}} = 0.04 - 0.06$ which is the characteristic frequency for low-frequency unsteadiness, despite the presence of several additional peaks at higher frequencies around $St_{L_{sep}} = 0.10 - 0.20$. This observation aligns with the findings of Morgan et al. (2013) and Laguarda et al. (2024b), which indicate that the low-frequency unsteadiness ($St_{L_{sep}} < 0.1$) of the bubble volume is primarily associated with the expansion and contraction of the recirculation region, while the dominant contributors to the signal variance are the higher-frequency ($St_{L_{sep}} \approx 0.1 - 0.2$) flapping motions of the shear layer.

The time histories of the spanwise-averaged wall-pressure and separation shock location fluctuations are presented in Figure 5.19 and Figure 5.20, respectively. The instantaneous wall-pressure signal is extracted at the location of maximum wall-pressure fluctuation, as discussed in Section 5.2.3, while the instantaneous shock location is determined from three-dimensional snapshots by identifying the local maximum of the density gradient ($|\nabla\rho|$) within a wall-normal plane at $y = 2.0\delta_0$, as illustrated in Figure 5.21. The wall-pressure and shock-location signals exhibit a high degree of similarity in shape but with opposite trends, indicating that higher wall-pressure fluctuations correspond to upstream shock motion, and vice versa. Consequently, the PSDs of wall-pressure and shock location for all three cases display nearly identical spectral characteristics, with a pronounced peak occurring in the low-frequency range around $St_{L_{sep}} = 0.04 - 0.05$.

The cross-correlations between the fluctuations of reversed-flow bubble volume, wall-pressure and separation shock location were computed, and their cross-correlation coefficients and corresponding time lags are summarized in Figure 5.5. As shown in the table, the wall-pressure and reversed-flow volume are quite strongly positively correlated, with maximum correlation coefficients R_{max} in the range of 0.61–0.72 and a positive time lag, indicating that the growth of the reversed-flow bubble precedes a pressure rise at the separation shock foot. Notably, $\mathcal{HS}$ exhibits the shortest time lag, whereas $\mathcal{HR}1$ shows the longest, which can be attributed to the greater distance over which disturbances in the bubble must propagate from roughly the center of the separation bubble to the point of maximum wall-pressure fluctuation.

In addition, the spanwise-averaged separation shock location and wall-pressure signals exhibit a very significant negative correlation with $|R_{max}|$ up to at least 0.94. This high correlation aligns with the pronounced similarity in the temporal evolutions of the wall-pressure and shock location signals. The time lags between the above two signals are

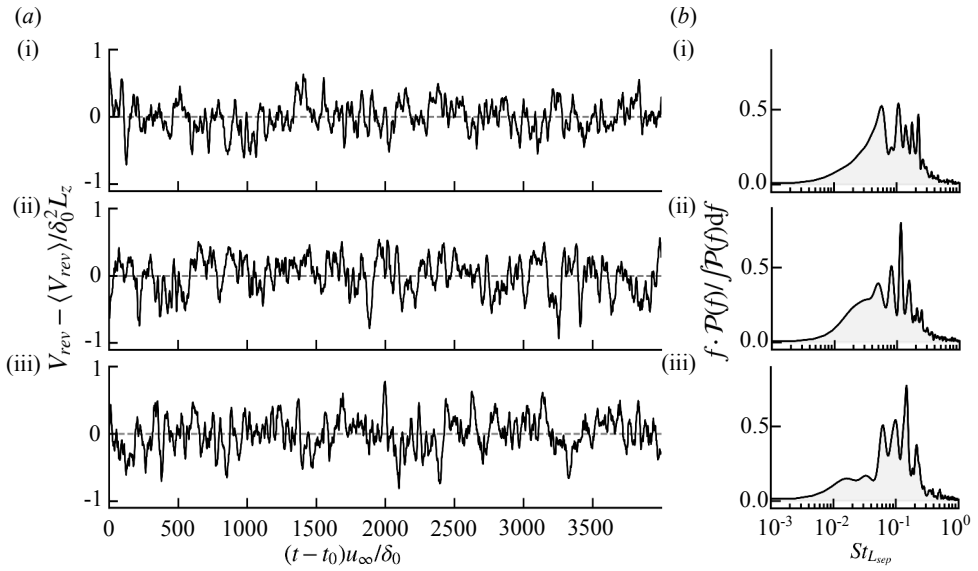

Figure 5.18: (a) Time evolution of the normalized reversed-flow volume fluctuations, and (b) corresponding pre-multiplied and normalized PSD of the signals: (i) $\mathcal{HS}$; (ii) $\mathcal{HR}1$; (iii) $\mathcal{HR}2$.

approximately $2.5\delta_0/u_\infty$ for all three cases, which is attributed to the similar propagation distance from the wall to the mean shock location at $y = 2.0\delta_0$ plane. A set of characteristic lines near the shock foot is extracted from the mean flow field, delineating the right boundary of the domain of dependence of the mean shock at $y = 2.0\delta_0$, as illustrated in Figure 5.21. The integration time along the characteristic line emanating from the sonic line and passing above the point of wall-pressure fluctuation peak is 2.57, 2.54, and 2.56 for the cases $\mathcal{HS}$, $\mathcal{HR}1$, and $\mathcal{HR}2$, respectively. These integration times closely match the corresponding correlation time lags, thereby supporting the reliability of the correlation-based time lag estimation. The observed positive time lag also indicates that wall-pressure fluctuations at the shock foot precede the shock motion, suggesting that the commonly used phrasing—stating that low-frequency shock excursions cause pressure fluctuations near the shock foot—may be an oversimplification, despite the widely acknowledged understanding that the separation-shock results from the coalescence of compression waves that deflect the mean flow. This phenomena also agree with Erengil (1993), who found that the oscillation of the separation point precedes the movement of the separation shock.

Based on the above analysis, it is evident that three key physical quantities involved in the low-frequency unsteadiness of STBLI follow a distinct temporal sequence as shown in Figure 5.21: the evolution of the reversed-flow bubble precedes the wall-pressure fluctuations at the separation shock foot, which in turn drive the motion of the separation shock. Therefore, it is not surprising that the separation shock location also exhibits a strong correlation with the reversed-flow bubble volume, accompanied by a larger time lag compared to that of the wall-pressure, as shown in Figure 5.5. The observed

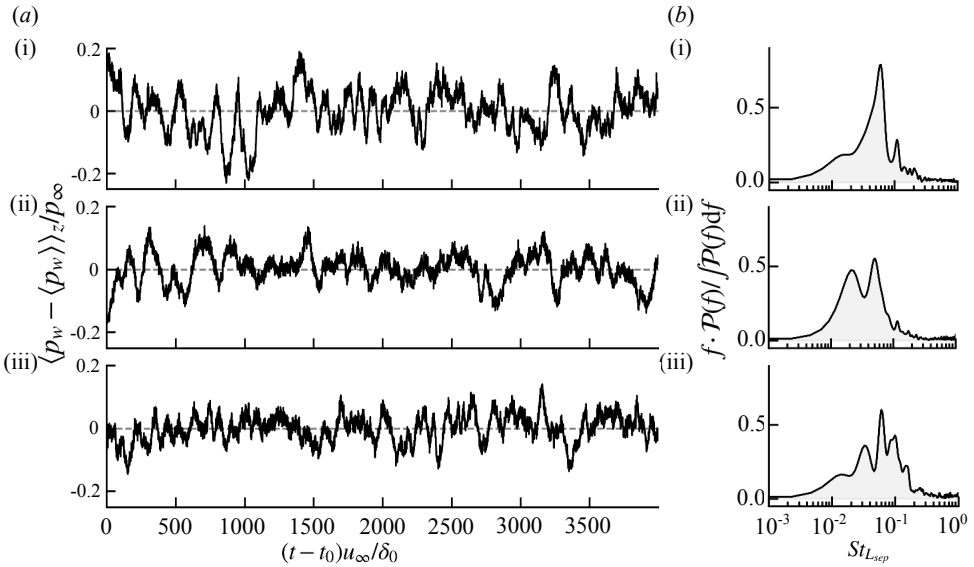

Figure 5.19: (a) Time evolution of the spanwise-averaged wall-pressure fluctuation at the location of its maximum amplitude, and (b) corresponding pre-multiplied and normalized PSD of the signals: (i) $\mathcal{HS}$; (ii) $\mathcal{HR}1$; (iii) $\mathcal{HR}2$.

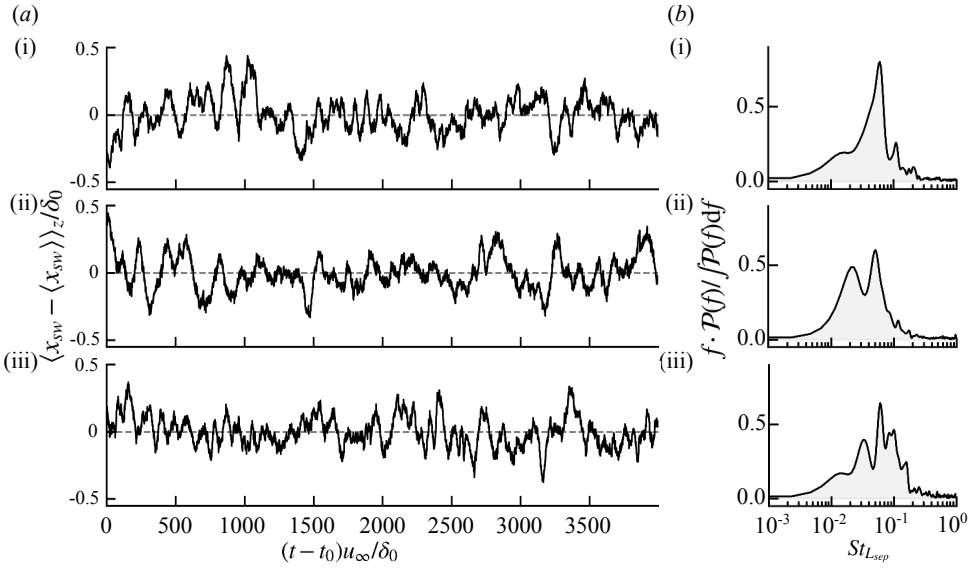

Figure 5.20: (*a*) Time evolution of the spanwise-averaged separation shock location at $y = 2.0\ \delta_0$, and (*b*) corresponding pre-multiplied and normalized PSD of the signal: (i) $\mathcal{HS}$; (ii) $\mathcal{HR}1$; (iii) $\mathcal{HR}2$.

	WP vs RFV	SL vs WP	SL vs RFV
$R_{\max}(\mathcal{HS})$	0.72	-0.97	-0.72
$R_{\max}(\mathcal{HR}1)$	0.61	-0.96	-0.61
$R_{\max}(\mathcal{HR}2)$	0.67	-0.94	-0.68
Lag($\mathcal{HS}$)	8.27	2.68	12.22
Lag($\mathcal{HR}1$)	14.99	2.28	21.47
Lag($\mathcal{HR}2$)	11.61	2.50	17.10

Table 5.5: Maximum (positive or negative) cross-correlation coefficient $R_{\max}$ and time lag ($\Delta t \cdot u_\infty/\delta_0$) between reversed-flow volume (RFV), wall-pressure fluctuation (WP), and shock location (SL) fluctuation in the $\mathcal{HS}$, $\mathcal{HR}1$, and $\mathcal{HR}2$.

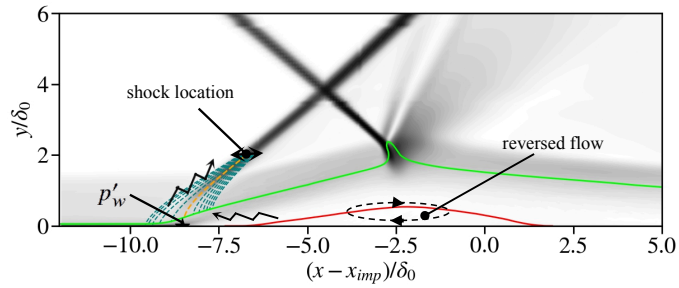

Figure 5.21: Schematic of the relations between reversed-flow, wall-pressure, and separation shock location. Dotted lines indicate the characteristic lines (the orange line indicates the characteristic line emanating above the point of maximum wall-pressure fluctuation), and solid green and red lines represent the sonic and separation lines, respectively.

correlation between the separation shock location and the reversed-flow bubble volume is consistent with the findings of Wu and Martin (2008) and Laguarda et al. (2024b).

We also find that the time lag between the reversed-flow bubble volume and either the wall-pressure at the shock foot or the shock location increases almost linearly as the mean shock position shifts further upstream in the two rough-wall cases, $\mathcal{HR}2$ and $\mathcal{HR}1$. This trend is consistent with the downstream influence mechanism, wherein acoustic disturbances require a longer upstream propagation time to reach the shock foot. Accordingly, the presence of roughness increases the time lag between changes in the reversed-flow region and the shock motion, primarily due to the extended propagation path induced by the upstream extension of separation.

5.2.5. SECONDARY FLOW STRUCTURES DOWNSTREAM OF REATTACHMENT

From the above analysis, we provide compelling evidence supporting that a so-called downstream mechanism is responsible for the large-scale low-frequency shock motion. This is also aligned with Grilli et al. (2012) and Clemens and Narayanaswamy (2014) in the sense that STBLI with a large separation bubble is mainly driven by a downstream mechanism. Priebe et al. (2016) and Pasquariello et al. (2017) argue that Görtler-like vortices may play a key role in driving the low-frequency variation of the separation bubble size. Laguarda et al. (2024b) also reported the presence of large-scale streaky structures, characterized by alternating low- and high-speed streamwise velocity streaks, originating near the separation shock foot and convecting downstream. In line with these findings, we observe the footprint of large-scale vortical structures downstream of the fragmented reattachment line, as shown in Figure 5.22. Animations corresponding to this figure are available in our data repository (Wu et al., 2025a). These structures have a characteristic width on the order of the boundary layer thickness, exhibit vigorous swirling motion and lateral oscillations, and evolve into alternating streaks of high and low skin-friction.

To better investigate the dynamics of these vortices, a modal analysis was carried out using Sparsity Promoting Dynamic Mode Decomposition (SPDMD) based on 4101 two-dimensional snapshot slices of the flow field extracted from the $(x - x_{imp})/\delta_0 = 8$ plane, spanning a time interval of $tu_\infty/\delta_0 \approx 4000$ and sampled at a non-dimensional frequency of $f_s\delta_0/u_\infty \approx 1.0$. The resulting frequency resolution spans the range of $2.5\times10^{-4} < St_{\delta_0} < 0.5$. SPDMD enhances the interpretability of DMD by promoting sparsity in the mode selection process, automatically identifying the dynamically most relevant modes from the full DMD spectrum. By tuning the regularization parameter of the SPDMD algorithm, 35 modes are retained for each case.

Similar modes structures were also observed in the low-Reynolds-number cases, with qualitatively consistent behavior. Therefore, for brevity, only the results for the high-Reynolds-number cases are presented. The modal amplitudes ψ_i, which are normalized by the mean mode amplitude, are shown in Figure 5.23. Considering the symmetric distribution of DMD modes, only the positive-frequency components are presented. A first observation for cases $\mathcal{HS}$ and $\mathcal{HR}2$ is that SPDMD selects modes in a frequency range starting at approximately $St_{L_{sep}} = 0.06$, which is a bit higher than the typical low-frequency unsteadiness range. In contrast, modes at lower frequencies are selected by SPDMD for case $\mathcal{HR}1$. Note that several very-low-frequency modes (e.g. the mode at

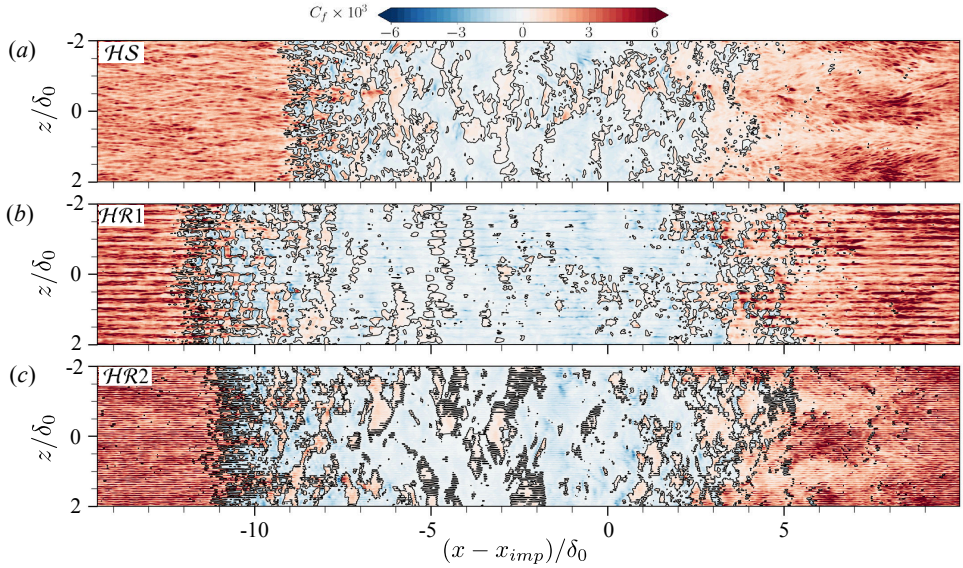

Figure 5.22: Instantaneous skin friction distribution of case (a) $\mathcal{HS}$; (b) $\mathcal{HR}1$; (c) $\mathcal{HR}2$. Black lines denote the region of reverse flow.

$St_{L_{sep}} \approx 0.003$) appear in the SPDMD results. However, because their frequencies lie near the resolution limit of SPDMD and may not be statistically robust, we refrain from assigning physical significance to these very-low-frequency features.

Figure 5.24 shows representative modes shapes for cases $\mathcal{HS}$, $\mathcal{HR}1$ and $\mathcal{HR}2$, corresponding to frequencies of $St_{L_{sep}} = 0.079, 0.023, 0.056$, respectively. Visualized as contours of the three velocity components, the modes reveal the presence of coherent streamwise vortices. For example, the first column of Figure 5.24 shows the mode structure of case $\mathcal{HS}$, where the streamwise velocity fluctuation u exhibits alternating low- and high-speed streaks, consistent with the upwash and downwash patterns in the wall-normal velocity v. Taking into account the spanwise velocity w, two pairs of counter-rotating vortices can be easily identified in the modes of $\mathcal{HS}$ and $\mathcal{HR}2$. In contrast, the selected low-frequency

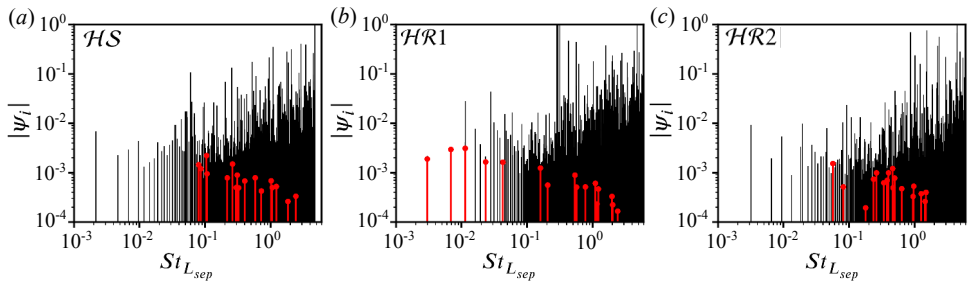

Figure 5.23: Normalized amplitudes (black lines) of all the positive DMD modes at $(x - x_{imp})/\delta_0 = 8$ from (a) $\mathcal{HS}$, (b) $\mathcal{HR}1$, and (c) $\mathcal{HR}2$. Red lines indicate an SPDMD subset of 17 positive modes.

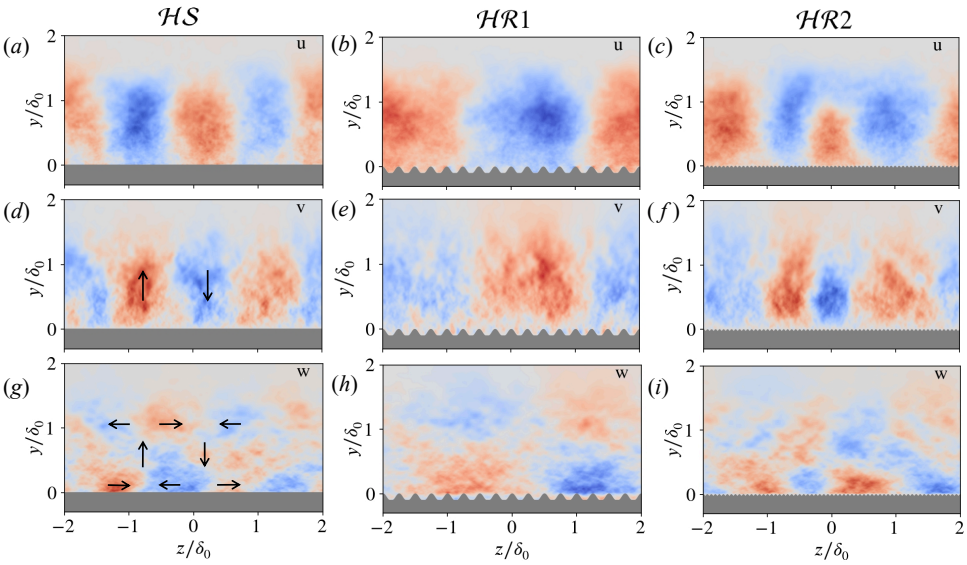

Figure 5.24: Real part of a representative low-frequency mode from $\mathcal{HS}$ ($St_{L_{sep}} = 0.079$), $\mathcal{HR}1$ ($St_{L_{sep}} = 0.023$), and $\mathcal{HR}2$ ($St_{L_{sep}} = 0.056$): (a, b, c) streamwise velocity; (d, e, f) vertical velocity; (g, h, i) spanwise velocity, at $(x - x_{imp})/\delta_0 = 8$. The contours are plotted in arbitrary units (normalized by the maximum mode amplitude). The arrows superimposed in (d,g) indicate the orientation of the velocity fluctuations from the selected mode.

mode of $\mathcal{HR}1$ only exhibits one pair of such vortices. However, several higher-frequency modes, e.g., at $St_{L_{sep}} = 0.156$, recover the two-pair structure. Despite these differences, the consistent presence of these vortices across all cases suggests that their formation is largely unaffected by the investigated roughness geometries.

These structures align with the Görtler-like vortices previously reported by, e.g., Priebe et al. (2016), Pasquariello et al. (2017), and Laguarda et al. (2024b). In our DMD of our present simulations, they are observed over a broad frequency range that extends well above the typical low-frequency unsteadiness of STBLI. Therefore, our results neither confirm nor rule out a causal relationship between the two phenomena, as stated in a previous work (Laguarda et al., 2024b).

5.3. CONCLUSION

This chapter has explored the effects of spanwise heterogeneous streamwise-aligned ridge-type roughness on STBLI at both low and high Reynolds numbers systematically. Two classes of rough surfaces were considered, designed to maintain consistent geometric characteristics under either inner or outer scaling, and their effects were compared to smooth-wall baselines under identical flow conditions.

The results demonstrate that ridge-type roughness substantially alters both the mean and unsteady flow characteristics of STBLI. Roughness-induced secondary flow in the form of streamwise vortices is observed in the upstream boundary layer. These structures do not appear to directly influence wall-pressure fluctuations near the separation-shock

foot. Instead, the secondary flow modulates the upstream momentum transport and the roughness increases the thickness of the subsonic region, thereby influencing the onset and extent of separation. The rough surfaces also incur a moderate drag penalty, with mean skin-friction coefficients increased by approximately 20% relative to the smooth-wall baselines, consistent with the downward shift of the van Driest–transformed velocity profile.

The comparison between the low-Reynolds-number rough-wall case and the two high-Reynolds-number rough-wall configurations provides guidance for scaling ridge-type roughness with Reynolds number. The inner-scaled high-Reynolds-number configuration, $\mathcal{HR}2$, preserves the roughness dimensions in viscous units and therefore maintains a flow organisation more closely resembling that of the low-Reynolds-number rough-wall case, $\mathcal{LR}$. In particular, both cases exhibit similar near-wall modulation, a relatively weak secondary flow compared with $\mathcal{HR}1$, and comparable overall control effects on the separation-shock-foot pressure fluctuations. By contrast, the outer-scaled configuration, $\mathcal{HR}1$, preserves the roughness dimensions relative to the boundary-layer thickness, but this corresponds to substantially larger roughness dimensions in viscous units at high Reynolds number. As a result, $\mathcal{HR}1$ produces stronger secondary motions, a more pronounced spanwise distortion of the incoming boundary layer, a larger drag penalty and a more strongly modified separation topology. These differences indicate that, for the present ridge-type roughness, maintaining inner-scaled geometric similarity is more effective than maintaining outer-scaled geometric similarity in preserving the low-Reynolds-number control behaviour when Reynolds number is increased.

We also identified that wall-pressure fluctuations near the separation shock foot consist of a low-frequency component associated with shock motion and a high-frequency component associated with shear-layer turbulence, and their relative contributions vary with Reynolds number: at low Reynolds number, the high-frequency component prevails, whereas at higher Reynolds number, the low-frequency component becomes dominant. Our spectral analysis showed that roughness effectively suppresses both low- and high-frequency components of wall-pressure fluctuations, with the suppression of low-frequency dynamics being more pronounced at higher Reynolds numbers.

This enhanced attenuation is linked to a more diffused shock foot produced by the less-full incoming turbulent boundary layer and the subsonic flow region within the valleys. As a result, the streamwise pressure gradient at the wall is weakened in regions of strong shock unsteadiness, thereby reducing the amplitude of the associated low-frequency fluctuations. At the moderately high Reynolds number, rough walls lead to a notable reduction of up to 27% in peak wall-pressure fluctuations.

The cross-correlation analyses established a clear temporal sequence in the low-frequency dynamics: expansion of the reverse-flow bubble precedes wall-pressure build-up, which in turn drives the motion of the separation shock. This temporal ordering supports a downstream-influence mechanism for low-frequency unsteadiness. Moreover, dynamic mode decomposition confirmed the presence of large-scale, Görtler-like vortices at reattachment in all cases. These vortices are observed over a wide range of modal frequencies, and they appear largely insensitive to variations in the roughness geometry.

Overall, the findings suggest that spanwise heterogeneous roughness — if properly designed — can serve as a robust and passive method to mitigate wall-pressure unsteadiness

over a broad range of frequencies in high-speed flows, albeit at the cost of a moderate drag increase. The results provide new physical insight into the interplay between roughness, Reynolds number effects, and low-frequency STBLI dynamics, and highlight the potential of roughness-based flow control for supersonic vehicles.

6

CONCLUSIONS AND OUTLOOK

形而上者谓之道，形而下者谓之器。

That which lies above form is called the Dao; that which lies within form is called a vessel.

《周易》/ *Book of Changes*

6.1. CONCLUSIONS

This thesis has investigated the passive control of a Mach 2.0 impinging STBLI using spanwise-heterogeneous roughness. High-fidelity wall-resolved large-eddy simulations were employed to examine how different roughness configurations, including ridge-type roughness and convergent–divergent riblets, modify the mean flow organization and the unsteady characteristics of the interaction. Particular emphasis was placed on the role of roughness-induced secondary flows in reshaping the incoming turbulent boundary layer and on the resulting attenuation of wall-pressure fluctuations in the vicinity of the separation shock foot.

Convergent–divergent (C–D) riblets act as a vortex generator with limited protrusion into the high-speed flow and are capable of inducing counter-rotating vortices within the turbulent boundary layer upstream of the interaction region. These vortical structures are expected to locally energize the incoming boundary layer and thereby mitigate shock-induced separation. However, the energization of the boundary layer is highly non-uniform in the spanwise direction. While the boundary layer is locally energized at the divergent lines (DLs), low-momentum fluid is lifted away from the wall at the convergent lines (CLs), resulting in a less full spanwise-averaged mean streamwise velocity profile and an enlarged subsonic region upstream of the interaction. As a consequence, the separation topology is significantly reshaped by the induced secondary flow, with separation being suppressed near the DLs and promoted near the CLs. The modified spanwise-averaged incoming boundary layer exhibits a reduced momentum near the wall, which leads to a smeared shock foot and an attenuation of the low-frequency unsteadiness. The spanwise heterogeneity of the wall-pressure fluctuations is primarily attributed to the lifting of the shear layer away from the wall at the CLs by the secondary flow.

Nevertheless, by analogy with MVGs, the performance of C–D riblets may depend on the installation location, and a pressure drag penalty is unavoidable with this geometry. Motivated by these considerations, ridge-type roughness is explored as an alternative strategy, as its streamwise-homogeneous geometry permits large-area deployment while potentially mitigating the location sensitivity associated with localized riblet patches.

Ridge-type roughness can also induce Prandtl's secondary flows of the second kind, which arise from the imbalance between the local production and viscous dissipation of turbulent kinetic energy, and are characterized by upwash over the ridges and downwash within the valleys. When the ridge spacing is relatively large, the induced secondary flow is sufficiently strong to energize the incoming boundary layer and suppress separation in a manner similar to that observed near the DLs of the C–D riblets. In this case, the subsonic region is not significantly enlarged near the ridge crests, leading to a reduced separation extent but relatively higher wall-pressure fluctuations due to the locally energized boundary layer. When the ridge spacing is reduced, for example to $D/\delta_0 = 0.25$, the secondary flow becomes weaker due to spatial constraints and the above effects caused by the induced secondary flow diminish. However, the presence of deeper valleys increases the subsonic region in the incoming turbulent boundary layer, analogous to the effect of the upwash induced by the C–D riblets. As a result, the boundary layer becomes less full, the separation shock foot is smeared, and the wall-pressure fluctuations are attenuated, partly due to a reduction in the streamwise wall-pressure gradient. Increasing the ridge

height, or equivalently the valley depth, produces a similar attenuation of wall-pressure fluctuations by further enlarging the subsonic region and reducing the fullness of the incoming turbulent boundary layer.

The control effectiveness of ridge-type roughness was further validated at higher Reynolds numbers, where an even stronger attenuation of wall-pressure fluctuations was observed. Reynolds number governs the relative contribution of low-frequency components to wall-pressure fluctuations near the separation shock foot in STBLI. At higher Reynolds numbers, the low-frequency component associated with separation-shock unsteadiness becomes dominant, and the roughness-induced modification of the incoming boundary layer remains effective in smearing the shock foot and reducing the wall-pressure gradient, resulting in the attenuation of wall-pressure fluctuation at the separation shock foot. In addition, a clear correlation between the separation bubble size, the wall-pressure fluctuations near the shock foot, and the shock motion was established, providing support for the downstream influence mechanism of low-frequency STBLI unsteadiness in flows with large separation bubbles. Large-scale, low-frequency Görtler-like vortices were identified downstream of the interaction region using sparsity-promoting dynamic mode decomposition. While these structures are likely related to the low-frequency unsteadiness of the separation bubble, no causal relationship could be established within the scope of the present study.

Based on the common feature observed in both the C–D riblets and ridge-type roughness cases, namely their ability to modify the subsonic region of the incoming turbulent boundary layer, it can be inferred that the extent of the subsonic region plays a key role in modulating the low-frequency dynamics of STBLI. A larger subsonic region enhances upstream–downstream communication across the shock, thereby weakening the shock strength and reducing the associated low-frequency loads. Although both roughness configurations can also locally energize the boundary layer, the present results indicate that energization of the incoming turbulent boundary layer is neither necessary nor sufficient to suppress low-frequency unsteadiness when large-scale separation occurs. Instead, such energization tends to produce a fuller boundary layer and a sharper shock, which in turn intensify the low-frequency unsteadiness. These findings suggest that no passive control strategy is universally optimal with respect to all SWBLI metrics simultaneously. Depending on the roughness configuration, separation extent and shock-induced pressure fluctuations may exhibit competing trends. Therefore, the effectiveness of passive control should be evaluated relative to specific engineering objectives rather than a single indicator such as separation size alone.

Overall, this thesis has systematically investigated the control effects of spanwise-heterogeneous roughness on impinging shock-wave/turbulent boundary-layer interactions. The results reveal the central role of roughness-induced secondary flows in modifying the incoming turbulent boundary layer and, in turn, the mean and unsteady characteristics of STBLI. It is demonstrated that spanwise-heterogeneous roughness, if properly designed, can serve as a robust and purely passive approach to mitigating wall-pressure unsteadiness over a broad range of frequencies in high-speed flows, albeit at the cost of a moderate increase in drag.

6.2. OUTLOOK

The present study has demonstrated the effectiveness of ridge-type roughness in mitigating wall-pressure unsteadiness in impinging STBLI over adiabatic walls. While these results provide a clear indication of the control potential of ridge-type roughness, several related aspects remain worthy of further investigation in order to broaden the understanding and assess their applicability under more general conditions.

One key open question concerns the impact of ridge-type roughness on wall heat transfer. STBLI is well known to generate severe unsteady thermal loads in the interaction region (Bernardini et al., 2016; Fu et al., 2021), and both the magnitude and location of the peak heating are difficult to predict (Dolling, 2001). This often represent a primary design constraint for high-speed vehicles. In canonical turbulent boundary layers, the Reynolds analogy suggests a close correspondence between skin friction and heat transfer, as both are governed predominantly by near-wall turbulent transport. Under such shear-dominated conditions, modifications of the incoming boundary layer by aligned ridge-type roughness may therefore be expected to induce comparable changes in wall heat flux, as suggested by the DNS study from Stroh et al. (2020). However, in the STBLI interaction region the flow is strongly non-equilibrium and characterized by intense adverse pressure gradients and pressure-drag contributions, which may weaken this correspondence. While the present results indicate a clear attenuation of pressure fluctuations, it remains unclear whether the associated modification of the incoming boundary layer and shock structure would alleviate or exacerbate the local and unsteady heat-transfer rates. A systematic investigation of both mean and fluctuating wall heat fluxes is therefore necessary to assess whether ridge-type roughness can provide a net benefit from a thermo-structural perspective. Within the current research framework, such an investigation can be readily performed by imposing an isothermal wall boundary condition. A complementary avenue worthy of exploration is the conjugate heat transfer approach, wherein solid-phase thermal conduction may redistribute spatially localised heat loads imposed by ridge-type roughness, thereby modifying the effective thermo-structural response of the surface.

Another important direction for future research is the extension of the present findings to more realistic internal-flow configurations, such as high-speed inlets, where the flow is confined by multiple walls (Bermejo-Moreno et al., 2014). In such environments, the thickening of a less full boundary layer induced by ridge-type roughness may influence the effective flow area, the mass flow rate, and the overall inlet performance. In particular, the net effect on total pressure recovery remains unclear, as the increase in wall friction due to surface roughness may compete with the reduction of shock-induced losses associated with a smeared shock system (Smith et al., 2002; Wu et al., 2025b). Quantifying this trade-off requires integrated assessments that consider boundary-layer development, shock dynamics, and global performance metrics in channel or duct flows.

Experimental studies would provide valuable complementary insight into the effects of ridge-type roughness on STBLI. Ridge-type roughness features a simple geometry that can be readily manufactured using conventional machining or additive manufacturing techniques, making it well-suited for wind-tunnel experiments. While Deyn et al. (2022a) quantified the effect of ridge-type roughness on skin friction in wind-tunnel experiments, and Wen et al. (2024) examined herringbone riblets in a Mach 2 STBLI, experimental

evidence regarding the influence of ridge-type roughness on STBLI remains lacking. Carefully designed experiments could provide additional confirmation of the predicted mean and unsteady flow features, while also enabling the exploration of higher Reynolds numbers and more complex flow conditions that remain challenging for wall-resolved simulations. Such combined numerical and experimental efforts would represent an important step toward assessing the feasibility of ridge-type roughness as a robust passive control strategy for STBLI.

Finally, the effectiveness of spanwise heterogeneous roughness may depend on the Mach number, as compressibility effects, shock strength, and boundary-layer structure vary substantially across subsonic, transonic, supersonic and hypersonic regimes. A systematic assessment of Mach-number dependence would therefore be valuable in clarifying the robustness of the control mechanism.

A

GRID INDEPENDENCE STUDY

A grid-independence study was conducted to examine the sensitivity of the results to spatial resolution. The assessment was performed separately in the streamwise and spanwise directions: the streamwise refinement is based on case $\mathcal{HS}$, while the spanwise refinement is based on case $\mathcal{HR}2$. A summary of the grid parameters and key outcomes is provided in Table A.1.

For the streamwise refinement, case $\mathcal{HS}_{x2}$ doubles the number of cells in $\mathcal{HS}$ in the streamwise direction, reducing Δx^+_{min} from 39 to 19.5. This refinement confirms that the streamwise resolution is adequate for the present LES. The velocity and Reynolds stresses profiles of the upstream turbulent boundary layer at $(x - x_{imp})/\delta_0$ are compared in Figure A.1. The LES results from $\mathcal{HS}$ and $\mathcal{HS}_{x2}$ both agree well with the reference DNS data, except slight deviation of streamwise Reynolds stress in the log region, where $\mathcal{HS}_{x2}$ slightly improves the agreement. This small deviation may result from the grid sensitivity of wall-resolved LES in the log region. Since the peak location and magnitude of $u'u'$ largely remain unaffected, this observed discrepancy does not compromise the reliability of the present conclusions. The influence of streamwise grid resolution on the STBLI is illustrated in Figure A.2. The mean skin-friction coefficient, wall-pressure, and wall-pressure-gradient distributions are largely unaffected, except for a slightly earlier onset of the interaction region. A small discrepancy in pressure fluctuations is observed in the interaction region, which is attributed to the highly aperiodic nature of the STBLI and limited statistical sampling time. Overall, these results indicate that the streamwise resolution used in the baseline grid is adequate for capturing both the mean and unsteady features of the interaction.

For the spanwise refinement, case $\mathcal{HR}2_{z2}$ doubles the number of cells in $\mathcal{HR}2$ in the spanwise direction, reducing Δz^+_{min} from 4.9 to 2.45—well below the typical requirement for LES—and increasing the number of cells per ridge from 12 to 24. This ensures that the rough-wall geometry is very well resolved. The upstream turbulent boundary layer profiles are compared in Figure A.1, where the mean velocity and Reynolds-stress components exhibit excellent agreement. Figure A.4 further shows that the mean skin-friction coefficient, wall-pressure, and wall-pressure-gradient distributions are virtually

A

Case	$\mathcal{HS}$	$\mathcal{HS}_{x2}$	$\mathcal{HR}2$	$\mathcal{HR}2_{z2}$
Grid resolution				
Δx^+_{min}	39	19.5	39	39
Δy^+_{min}	0.94	0.94	0.94	0.94
Δz^+_{min}	9.8	9.8	4.9	2.45
Grid number				
N_x^{max}	1088	2176	1088	1088
N_y	240	240	312	312
N_z^{max}	384	384	768	1536
run-time(δ_0/u_∞)	3997	3997	3997	1333
TBL statistics				
max($\langle u\rangle^+_{vd}$)	24.78	25.04 (+1.0%)	22.53	22.58 (+0.2%)
max($\langle\rho\rangle\langle u'u'\rangle/\tau_w$)	8.34	8.16 (-2.2%)	5.72	5.79 (+1.2%)
$C_f \times 10^3$	2.22	2.18 (-1.8%)	2.69	2.59 (-3.7%)
STBLI statistics				
L_{sep}/δ_0	9.22	9.18 (-0.4%)	12.92	12.96 (+0.3%)
max($\sqrt{\langle p'p'\rangle}/p_\infty$)	0.0857	0.0809 (-5.6%)	0.0623	0.0625 (+0.3%)
max($\frac{d\langle p_w\rangle}{dx}/\frac{p_\infty}{\delta_0}$)	0.537	0.526 (-2.0%)	0.382	0.396 (+3.7%)

Table A.1: Numerical parameters and results of the grid independence study. Baseline cases are $\mathcal{HS}$ and $\mathcal{HR}2$, respectively. Percentage deviations from the baseline cases are reported in brackets.

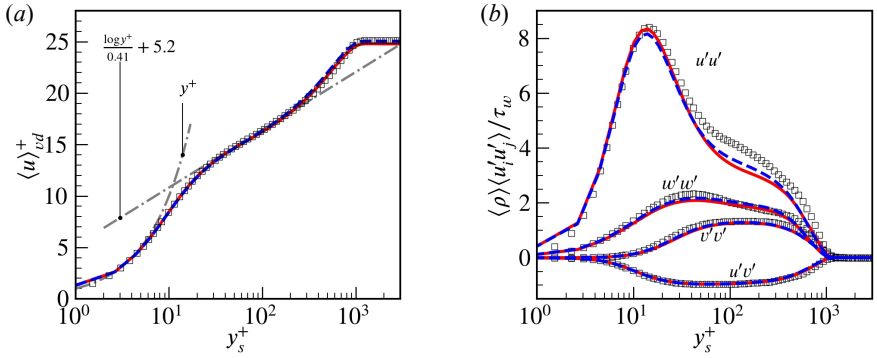

Figure A.1: Streamwise grid sensitivity study of the upstream turbulent boundary layer: (*a*) van Driest-transformed mean velocity profiles and (*b*) density-scaled Reynolds stress components. The baseline case $\mathcal{HS}$ is shown as a solid red line, and the refined case $\mathcal{HS}_{x2}$ as a blue dashed line. Reference DNS data from Pirozzoli and Bernardini, 2011 are shown as squares.

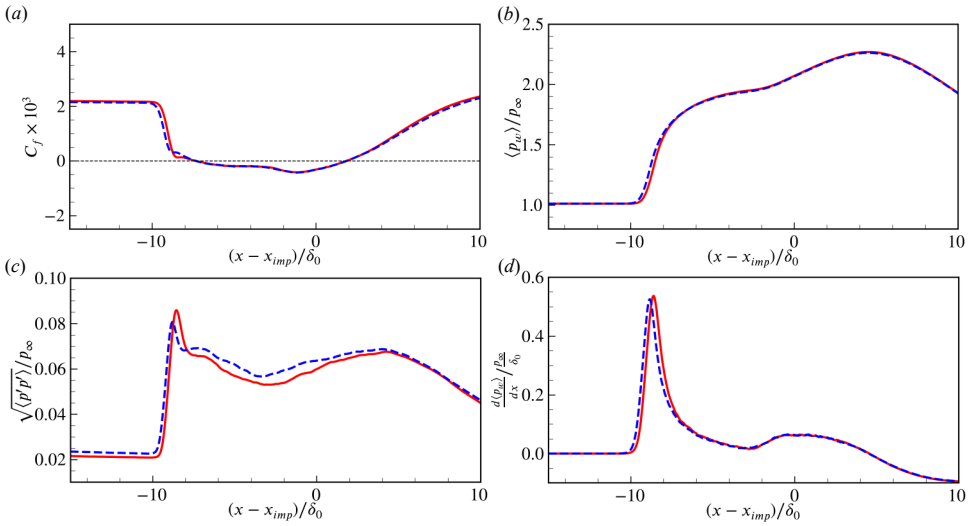

Figure A.2: Streamwise grid sensitivity study of the interaction region: streamwise distributions of (*a*) skin friction coefficient, (*b*) wall-pressure, (*c*) wall-pressure fluctuation, and (*d*) wall-pressure gradient. The baseline case $\mathcal{HS}$ is shown as a solid red line, and the refined case $\mathcal{HS}_{x2}$ as a blue dashed line.

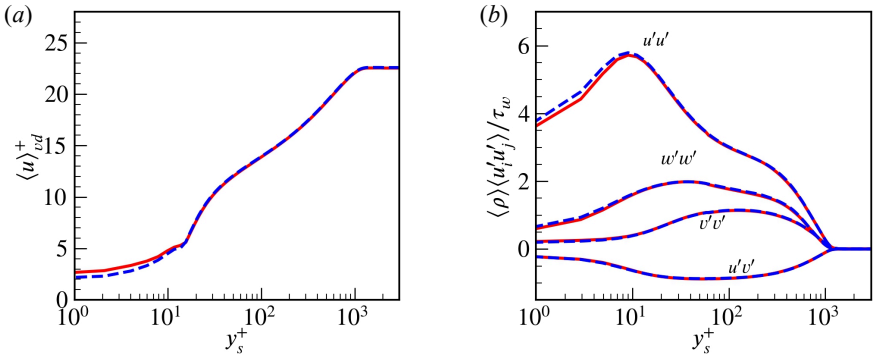

Figure A.3: Spanwise grid sensitivity study of the upstream turbulent boundary layer: (*a*) van Driest-transformed mean velocity profiles and (*b*) density-scaled Reynolds stress components. The baseline case $\mathcal{HR}2$ is shown as a solid red line, and the refined case $\mathcal{HR}2_{z2}$ as a blue dashed line.

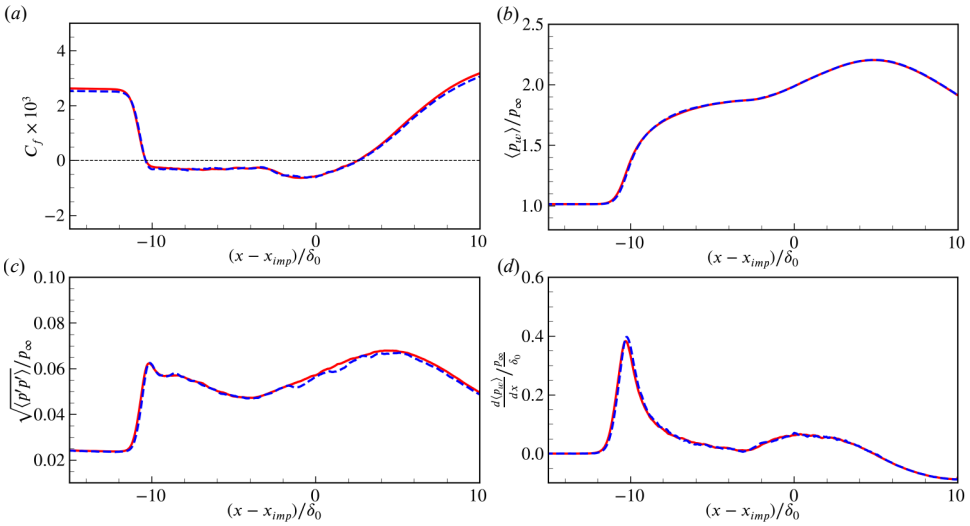

Figure A.4: Spanwise grid sensitivity study of the interaction region: streamwise distributions of (*a*) skin friction coefficient, (*b*) wall-pressure, (*c*) wall-pressure fluctuation, and (*d*) wall-pressure gradient. The baseline case $\mathcal{HR}2$ is shown as a solid red line, and the refined case $\mathcal{HR}2_{z2}$ as a blue dashed line.

unchanged. A slight discrepancy in wall-pressure fluctuations is observed upstream of the reattachment point, which is expected due to the unsteady nature of the interaction. Overall, the results confirm that the spanwise resolution used in the baseline simulation is sufficient.

BIBLIOGRAPHY

Amitay, M., D. R. Smith, V. Kibens, D. E. Parekh, and A. Glezer (2001). "Aerodynamic flow control over an unconventional airfoil using synthetic jet actuators". *AIAA J.* 39.3, pp. 361–370.

Anderson, J. D. (2003). *Modern Compressible Flow: With Historical Perspective*. Aeronautical and Aerospace Engineering Series. McGraw-Hill Education.

Anderson, J. D. (2017). *Fundamentals of Aerodynamics*. McGraw-Hill series in aeronautical and aerospace engineering. McGraw-Hill Education.

Andreopoulos, J. and K. C. Muck (1987). "Some new aspects of the shock-wave/boundary-layer interaction in compression-ramp flows". *J. Fluid Mech.* 180, pp. 405–428.

Babinsky, H., Y. Li, and C. W. P. Ford (2009). "Microramp control of supersonic oblique shock-wave/boundary-layer interactions". *AIAA J.* 47.3, pp. 668–675.

Babinsky, H., N. Makinson, and C. Morgan (2007). "Micro-vortex generator flow control for supersonic engine inlets". *45th AIAA aerospace sciences meeting and exhibit*, p. 521.

Babinsky, H. and H. Ogawa (2008). "SBLI control for wings and inlets". en. *Shock Waves* 18.2, pp. 89–96.

Başkaya, A. O., M. Capriati, A. Turchi, T. Magin, and S. Hickel (2024). "Assessment of immersed boundary methods for hypersonic flows with gas–surface interactions". *Comput. & Fluids* 270, p. 106134.

Ben-Dor, G., O. Igra, and T. Elperin (2000). *Handbook of Shock Waves, Three Volume Set*. Elsevier Science.

Beresh, S. J., N. T. Clemens, and D. S. Dolling (2002). "Relationship between upstream turbulent boundary-layer velocity fluctuations and separation shock unsteadiness". *AIAA J.* 40.12, pp. 2412–2422.

Bermejo-Moreno, I., L. Campo, J. Larsson, J. Bodart, D. Helmer, and J. K. Eaton (2014). "Confinement effects in shock wave/turbulent boundary layer interactions through wall-modelled large-eddy simulations". *J. Fluid Mech.* 758, pp. 5–62.

Bernardini, M., I. Asproulias, J. Larsson, S. Pirozzoli, and F. Grasso (2016). "Heat transfer and wall temperature effects in shock wave turbulent boundary layer interactions". *Phys. Rev. Fluids* 1.8, p. 084403.

Brusniak, L. and D. S. Dolling (1994). "Physics of unsteady blunt-fin-induced shock wave/turbulent boundary layer interactions". *J. Fluid Mech.* 273, pp. 375–409.

Budich, B., V. Pasquariello, M. Grilli, and S. Hickel (2013). "Passive flow control of shock wave/turbulent boundary layer interactions using micro-vortex generators". *International Symposium on Turbulence and Shear Flow Phenomena*, pp. 1–6.

Burbank, P. (1962). *Heat-transfer and Pressure Measurements on a Flat-plate Surface and Heat-transfer Measurements on Attached Protuberances in a Supersonic Turbulent Boundary Layer at Mach Numbers of 2.65, 3.51, and 4.44: Paige B. Burbank, Robert A. Newlander and Ida K. Collins*. National Aeronautics and Space Administration.

Carl, M., V. Hannemann, and G. Eitelberg (1998). “Shock/shock interaction experiments in the high enthalpy shock tunnel Göttingen”. *36th AIAA Aerospace Sciences Meeting and Exhibit*, p. 775.

Choi, H., P. Moin, and J. Kim (1993). “Direct numerical simulation of turbulent flow over riblets”. *J. Fluid Mech.* 255, pp. 503–539.

Chung, D., N. Hutchins, M. P. Schultz, and K. A. Flack (2021). “Predicting the Drag of Rough Surfaces”. en. *Annu. Rev. Fluid Mech.* 53.1, pp. 439–471.

Clemens, N. T. and V. Narayanaswamy (2014). “Low-Frequency Unsteadiness of Shock Wave / Turbulent Boundary Layer Interactions”. en. *Annu. Rev. Fluid Mech.* 46.1, pp. 469–492.

Clemens, N. (2022). *Unsteadiness of Shock Wave/Turbulent Boundary Layer Interactions*. YouTube video, Cambridge University Press. https://www.youtube.com/watch?v=4AeR-1xTNr0&list=PLSuwApv72EvgWzgAtMa1-aTpJMjObu0Th.

Delery, J. M. (1985). “Shock wave/turbulent boundary layer interaction and its control”. en. *Prog. Aero. Sci.* 22.4, pp. 209–280.

Délery, J. and R. Bur (2000). “The physics of shock wave/boundary layer interaction control: last lessons learned”. *Office National d Etudes ET DE Recherches Aerospatiales Onera-Publications-Tp* 181.

Délery, J. and J. P. Dussauge (2009). “Some physical aspects of shock wave/boundary layer interactions”. *Shock Waves* 19.6, pp. 453–468.

Délery, J., J. G. Marvin, and E. Reshotko (1986). *Shock-wave boundary layer interactions*. Tech. rep. Neuilly-sur-Seine, France.

Della Posta, G., M. Blandino, D. Modesti, F. Salvadore, and M. Bernardini (2023). “Direct numerical simulation of supersonic boundary layers over a microramp: effect of the Reynolds number”. *J. Fluid Mech.* 974, A44.

Della Posta, G., E. Martelli, F. Salvadore, and M. Bernardini (Feb. 2024). *High-fidelity simulations of microramp-controlled shock wave/boundary layer interaction*. en. arXiv:2402.18971 [physics].

Deyn, L. H., D. Gatti, and B. Frohnapfel (2022a). “From drag-reducing riblets to drag-increasing ridges”. en. *J. Fluid Mech.* 951, A16.

Deyn, L. H., M. Schmidt, R. Örlü, A. Stroh, J. Kriegseis, B. Böhm, and B. Frohnapfel (Jan. 2022b). “Ridge-type roughness: from turbulent channel flow to internal combustion engine”. *Exp. Fluids* 63.1, p. 18.

Dolling, D. S. (Aug. 2001). “Fifty Years of Shock-Wave/Boundary-Layer Interaction Research: What Next?” *AIAA J.* 39.8, pp. 1517–1531.

Dolling, D. S. and M. T. Murphy (1983). “Unsteadiness of the separation shock wave structure in a supersonic compression ramp flowfield”. *AIAA J.* 21.12, pp. 1628–1634.

Ducros, F., V. Ferrand, F. Nicoud, C. Weber, D. Darracq, C. Gacherieu, and T. Poinsot (1999). “Large-eddy simulation of the shock/turbulence interaction”. *J. Comput. Phys.* 152.2, pp. 517–549.

Dupont, P., C. Haddad, and J. F. Debiève (2006). “Space and time organization in a shock-induced separated boundary layer”. *J. Fluid Mech.* 559, p. 255.

Edney, B. (1967). *Anomalous heat transfer and pressure distributions on blunt bodies at hypersonic speeds in the presence of an impinging shock*. Tech. rep. Flygtekniska Forsoksanstalten, Stockholm (Sweden).

Erengil, M. E. (1993). *Physical causes of separation shock unsteadiness in shock wave/turbulent boundary layer interactions*. The University of Texas at Austin.

Erengil, M. E. and D. S. Dolling (1991). "Unsteady wave structure near separation in a Mach 5 compression ramp interaction". *AIAA J.* 29.5, pp. 728–735.

Frohnapfel, B., L. von Deyn, J. Yang, J. Neuhauser, A. Stroh, R. Örlü, and D. Gatti (2024). "Flow resistance over heterogeneous roughness made of spanwise-alternating sandpaper strips". *J. Fluid Mech.* 980, A31.

Fu, L., M. Karp, S. T. Bose, P. Moin, and J. Urzay (2021). "Shock-induced heating and transition to turbulence in a hypersonic boundary layer". *J. Fluid Mech.* 909, A8.

Gaitonde, D. V. (Jan. 2015). "Progress in shock wave/boundary layer interactions". *Prog. Aerosp. Sci.* 72, pp. 80–99.

Gaitonde, D. V. and M. C. Adler (Jan. 19, 2023). "Dynamics of Three-Dimensional Shock-Wave/Boundary-Layer Interactions". *Annu. Rev. Fluid Mech.* 55.1, pp. 291–321.

Ganapathisubramani, B., N. T. Clemens, and D. S. Dolling (2006). "Large-scale motions in a supersonic turbulent boundary layer". *J. Fluid Mech.* 556, pp. 271–282.

Ganapathisubramani, B., N. T. Clemens, and D. S. Dolling (2007). "Effects of upstream boundary layer on the unsteadiness of shock-induced separation". *J. Fluid Mech.* 585, pp. 369–394.

Ganapathisubramani, B., N. T. Clemens, and D. S. Dolling (2009). "Low-frequency dynamics of shock-induced separation in a compression ramp interaction". *J. Fluid Mech.* 636, pp. 397–425.

Ghosal, S. (1996). "An analysis of numerical errors in large-eddy simulations of turbulence". *J. Comput. Phys.* 125.1, pp. 187–206.

Gonsalez, J. and D. S. Dolling (1993). "Correlation of interaction sweepback effects on unsteady shock-induced turbulent separation". *31st Aerospace Sciences Meeting*, p. 776.

Griffith, B. E. and N. A. Patankar (2020). "Immersed methods for fluid–structure interaction". *Annu. Rev. Fluid Mech.* 52.1, pp. 421–448.

Grilli, M., P. J. Schmid, S. Hickel, and N. A. Adams (2012). "Analysis of unsteady behaviour in shockwave turbulent boundary layer interaction". *J. Fluid Mech.* 700, pp. 16–28.

Grinstein, F. F., L. G. Margolin, and W. J. Rider (2007). *Implicit large eddy simulation: Computing Turbulent Flow Dynamics*. Vol. 10. Cambridge university press Cambridge.

Guo, T., J. Fang, J. Zhang, and X. Li (2022a). "Direct numerical simulation of shock-wave/boundary layer interaction controlled with convergent–divergent riblets". *Phys. Fluids* 34.8, p. 086101.

Guo, T., J. Fang, J. Zhang, and X. Li (2022b). "Investigation of the secondary flow by convergent–divergent riblets in a supersonic turbulent boundary layer over a compression ramp". *Phys. Fluids* 34.10.

Guo, T., J. Fang, S. Zhong, and C. Moulinec (2022c). "Direct numerical simulations of a turbulent channel flow developing over convergent–divergent riblets". en. *Int. J. Heat Fluid Flow* 98, p. 109069.

Guo, T., J. Fang, S. Zhong, and C. Moulinec (2022d). "Energy-based drag decomposition analyses for a turbulent channel flow developing over convergent–divergent riblets". *Phys. Fluids* 34.2.

Guo, T., S. Zhong, and T. Craft (2020). "Secondary flow in a laminar boundary layer developing over convergent-divergent riblets". *Int. J. Heat Fluid Flow* 84, p. 108598.

Hickel, S., N. A. Adams, and J. A. Domaradzki (2006). “An adaptive local deconvolution method for implicit LES”. *J. Comput. Phys.* 213.1, pp. 413–436.

Hickel, S., C. P. Egerer, and J. Larsson (2014). “Subgrid-scale modeling for implicit large eddy simulation of compressible flows and shock-turbulence interaction”. en. *Phys. Fluids* 26.10, p. 106101.

Holden, H. and H. Babinsky (2007). “Effect of microvortex generators on seperated normal shock/boundary layer interactions”. *J. Aircraft* 44.1, pp. 170–174.

Hou, Y. (2003). “Particle image velocimetry study of shock-induced turbulent boundary layer separation”. PhD thesis. Austin: The University of Texas at Austin.

Hu, W. (2020). “Dynamics of a supersonic flow over a backward/forward-facing step”. PhD thesis. Delft: Delft University of Technology.

Hu, W., S. Hickel, and B. W. van Oudheusden (2022). “Unsteady mechanisms in shock wave and boundary layer interactions over a forward-facing step”. *J. Fluid Mech.* 949, A2.

Hu, W., S. Hickel, and B. W. Van Oudheusden (2021). “Low-frequency unsteadiness mechanisms in shock wave/turbulent boundary layer interactions over a backward-facing step”. *J. Fluid Mech.* 915, A107.

Humble, R. A., G. E. Elsinga, F. Scarano, and B. W. Van Oudheusden (2009). “Three-dimensional instantaneous structure of a shock wave/turbulent boundary layer interaction”. *J. Fluid Mech.* 622, pp. 33–62.

Hwang, H. G. and J. H. Lee (Jan. 2018). “Secondary flows in turbulent boundary layers over longitudinal surface roughness”. *Phys. Rev. Fluids* 3 (1), p. 014608.

Jenkins, D. R. (2007). *X-15: extending the frontiers of flight*. Vol. 562. NASA.

Jovanović, M. R., P. J. Schmid, and J. W. Nichols (2014). “Sparsity-promoting dynamic mode decomposition”. *Phys. Fluids* 26.2, p. 024103.

Kadivar, M., D. Tormey, and G. McGranaghan (2021). “A review on turbulent flow over rough surfaces: Fundamentals and theories”. en. *Int. J. Thermofluids* 10, p. 100077.

Kirkpatrick, M. P., S. W. Armfield, and J. H. Kent (2003). “A representation of curved boundaries for the solution of the Navier–Stokes equations on a staggered three-dimensional Cartesian grid”. *J. Comput. Phys.* 184.1, pp. 1–36.

Kistler, A. L. (1964). “Fluctuating wall pressure under a separated supersonic flow”. *J. Acoust. Soc. Am.* 36.3, pp. 543–550.

Klein, M., A. Sadiki, and J. Janicka (2003). “A digital filter based generation of inflow data for spatially developing direct numerical or large eddy simulations”. en. *J. Comput. Physi.* 186.2, pp. 652–665.

Kravchenko, A. G. and P. Moin (1997). “On the effect of numerical errors in large eddy simulations of turbulent flows”. *J. Comput. Phys.* 131.2, pp. 310–322.

Laguarda, L. (2024). “Shock interaction phenomena”. English. Dissertation (TU Delft). Delft University of Technology.

Laguarda, L. and S. Hickel (2024a). “Analysis of improved digital filter inflow generation methods for compressible turbulent boundary layers”. *Comput. Fluids* 268, p. 106105.

Laguarda, L. and S. Hickel (2024b). “Low-frequency dynamics of turbulent recirculation bubbles”. *Phys. Fluids* 36.8.

Laguarda, L., S. Hickel, F. F. J. Schrijer, and B. W. van Oudheusden (2024a). "Shock-wave/turbulent boundary-layer interaction with a flexible panel". *Phys. Fluids* 36, p. 016120.

Laguarda, L., S. Hickel, F. F. J. Schrijer, and B. W. Van Oudheusden (June 25, 2024b). "Reynolds number effects in shock-wave/turbulent boundary-layer interactions". *J. Fluid Mech.* 989, A20.

Li, W. and H. Liu (2019). "Large-eddy simulation of shock-wave/boundary-layer interaction control using a backward facing step". *Aerosp. Sci. Technol.* 84, pp. 1011–1019.

Lin, J. C. (2002). "Review of research on low-profile vortex generators to control boundary-layer separation". *Prog. Aerosp. Sci.* 38.4-5, pp. 389–420.

Liu, Y., W. Zhao, Q. Zhao, Q. Zhou, and J. Xu (2022). "Passage shock wave/boundary layer interaction control for transonic compressors using bumps". *Chin. J. Aeronaut.* 35.2, pp. 82–97.

Lund, T. S., X. H. Wu, and K. D. Squires (1998). "Generation of Turbulent Inflow Data for Spatially-Developing Boundary Layer Simulations". *J. Comput. Phys.* 140.2, pp. 233–258.

Meyer, M., A. Devesa, S. Hickel, X. Y. Hu, and N. A. Adams (2010). "A conservative immersed interface method for Large-Eddy Simulation of incompressible flows". en. *J. Comput. Phys.* 229.18, pp. 6300–6317.

Mittal, R. and G. Iaccarino (2005). "Immersed boundary methods". *Annu. Rev. Fluid Mech.* 37.1, pp. 239–261.

Mohammadikarachi, A., M. Z. Yousif, B. Nugroho, and H. C. Lim (2024). "An exhaustive review of studies on bio-inspired convergent–divergent riblets". *Ocean Eng.* 295, p. 116965.

Morgan, B., K. Duraisamy, N. Nguyen, S. Kawai, and S. Lele (2013). "Flow physics and RANS modelling of oblique shock/turbulent boundary layer interaction". *J. Fluid Mech.* 729, pp. 231–284.

Morgan, B., J. Larsson, S. Kawai, and S. K. Lele (Mar. 2011). "Improving Low-Frequency Characteristics of Recycling/Rescaling Inflow Turbulence Generation". *AIAA J.* 49.3, pp. 582–597.

Nagamatsu, H. and R. Ficarra (1985). "Supercritical airfoil drag reduction by passive shock wave/boundary layer control in the Mach number range. 75 to. 90". *23rd Aerospace Sciences Meeting*, p. 207.

Nikitin, N. V., N. V. Popelenskaya, and A. Stroh (2021). "Prandtl's Secondary Flows of the Second Kind. Problems of Description, Prediction, and Simulation". en. *Fluid Dyn.* 56.4, pp. 513–538.

Nikuradse, J. (1926). "Untersuchungen Uber die Geschwindigkeits-verteilung in turbulenten Stromungen VDI". *Forschungsheft* 291.

Nugroho, B., N. Hutchins, and J. P. Monty (June 2013). "Large-scale spanwise periodicity in a turbulent boundary layer induced by highly ordered and directional surface roughness". *Int. J. Heat Fluid Flow* 41, pp. 90–102.

O'Rourke, J. (1998). *Computational geometry in C*. Cambridge university press.

Ogawa, H., H. Babinsky, M. Pätzold, and T. Lutz (2008). "Shock-Wave/Boundary-Layer Interaction Control Using Three-Dimensional Bumps for Transonic Wings". *AIAA J.* 46.6, pp. 1442–1452.

Örley, F., V. Pasquariello, S. Hickel, and N. A. Adams (2015). "Cut-element based immersed boundary method for moving geometries in compressible liquid flows with cavitation". *J. Comput. Phys.* 283, pp. 1–22.

Panaras, A. G. and F. K. Lu (2015). "Micro-vortex generators for shock wave/boundary layer interactions". en. *Prog. Aero. Sci.* 74, pp. 16–47.

Pasquariello, V. (2018). "Analysis and Control of Shock-Wave/Turbulent Boundary-Layer Interactions on Rigid and Flexible Walls". PhD thesis. Technische Universität München.

Pasquariello, V., M. Grilli, S. Hickel, and N. A. Adams (2014). "Large-eddy simulation of passive shock-wave/boundary-layer interaction control". en. *Int. J. Heat Fluid Flow* 49, pp. 116–127.

Pasquariello, V., G. Hammerl, F. Örley, S. Hickel, C. Danowski, A. Popp, W. A. Wall, and N. A. Adams (2016). "A cut-cell finite volume–finite element coupling approach for fluid–structure interaction in compressible flow". *J. Comput. Phys.* 307, pp. 670–695.

Pasquariello, V., S. Hickel, and N. A. Adams (2017). "Unsteady effects of strong shock-wave/boundary-layer interaction at high Reynolds number". *J. Fluid Mech.* 823, pp. 617–657.

Pearcey, H. H. (1961). "Shock induced separation and its prevention". *Bound. Layer Flow Control* 2, pp. 1170–1344.

Peskin, C. S. (1972). "Flow patterns around heart valves: a numerical method". *J. Comput. Phys.* 10.2, pp. 252–271.

Piponniau, S., J. P. Dussauge, J. F. Debieve, and P. Dupont (2009). "A simple model for low-frequency unsteadiness in shock-induced separation". *J. Fluid Mech.* 629, pp. 87–108.

Pirozzoli, S. and M. Bernardini (Dec. 10, 2011). "Turbulence in supersonic boundary layers at moderate Reynolds number". *J. Fluid Mech.* 688, pp. 120–168.

Pirozzoli, S. and M. Bernardini (2013). "Probing high-Reynolds-number effects in numerical boundary layers". *Phys. Fluids* 25.2.

Pirozzoli, S. and F. Grasso (2006). "Direct numerical simulation of impinging shock wave/turbulent boundary layer interaction at M= 2.25". *Phys. Fluids* 18.6.

Pirozzoli, S., F. Grasso, and T. B. Gatski (2004). "Direct numerical simulation and analysis of a spatially evolving supersonic turbulent boundary layer at M= 2.25". *Phys. Fluids* 16.3, pp. 530–545.

Pisano, D. A., F. R. van der Linden, and F. H. Winter (2006). *Chuck Yeager and the Bell X-1:Breaking the Sound Barrier*. Harry N. Abrams, Inc.

Plotkin, K. J. (1975). "Shock wave oscillation driven by turbulent boundary-layer fluctuations". *AIAA J.* 13.8, pp. 1036–1040.

Poinsot, T. J. and S. K. Lele (1992). "Boundary conditions for direct simulations of compressible viscous flows". *J. Comput. Phys.* 101.1, pp. 104–129.

Prandtl, L. (1931). *Einführung in die Grundbegriffe der Strömungslehre*. German. Akademische Verlagsgesellschaft.

Priebe, S., J. H. Tu, C. W. Rowley, and M. P. Martín (Nov. 2016). "Low-frequency dynamics in a shock-induced separated flow". en. *J. Fluid Mech* 807, pp. 441–477.

Raghunathan, S. (1988). "Passive control of shock-boundary layer interaction". *Prog. Aerosp. Sci.* 25.3, pp. 271–296.

Roy, S., J. P. S. Sandhu, and S. Ghosh (2021). "Drag reduction in transonic shock-wave/boundary-layer interaction using porous medium: a computational study". *Shock Waves* 31.2, pp. 117–132.

Rybalko, M., H. Babinsky, and E. Loth (2012). "Vortex Generators for a Normal Shock/Boundary Layer Interaction with a Downstream Diffuser". en. *J. Prop. Power* 28.1, pp. 71–82.

Sabnis, K. and H. Babinsky (2023). "A review of three-dimensional shock wave–boundary-layer interactions". *Prog. Aerosp. Sci.* 143, p. 100953.

Schlichting, H. and K. Gersten (2016). *Boundary-Layer Theory*. Engineering. Springer Berlin Heidelberg.

Schmid, P. J. (2010). "Dynamic mode decomposition of numerical and experimental data". *J. Fluid Mech.* 656, pp. 5–28.

Schmid, P. J. (2022). "Dynamic Mode Decomposition and Its Variants". *Annu. Rev. Fluid Mech.* 54.1, pp. 225–254.

Schülein, E. (2006). "Skin friction and heat flux measurements in shock/boundary layer interaction flows". *AIAA J.* 44.8, pp. 1732–1741.

Seo, J. H. and R. Mittal (2011). "A sharp-interface immersed boundary method with improved mass conservation and reduced spurious pressure oscillations". *J. Comput. Phys.* 230.19, pp. 7347–7363.

Shu, C. W. (2006). "Essentially non-oscillatory and weighted essentially non-oscillatory schemes for hyperbolic conservation laws". *Advanced Numerical Approximation of Nonlinear Hyperbolic Equations: Lectures given at the 2nd Session of the Centro Internazionale Matematico Estivo (CIME) held in Cetraro, Italy, June 23–28, 1997*. Springer, pp. 325–432.

Smagorinsky, J. (1963). "General circulation experiments with the primitive equations: I. The basic experiment". *Mon. Weath. Rev.* 91.3, pp. 99–164.

Smith, A., H. Babinsky, C. Dhanasekaran, M. Savill, and B. Dawes (2003). "Computational investigation of groove controlled shock wave/boundary layer interaction". *41st Aerospace Sciences Meeting and Exhibit*, p. 446.

Smith, A., H. Holden, H. Babinsky, J. Fulker, and P. Ashill (2002). "Control of normal shock wave/turbulent boundary layer interactions using streamwise grooves". *40th AIAA Aerospace Sciences Meeting & Exhibit*, p. 978.

Souverein, L., P. Dupont, J. Debieve, J. Dussauge, B. W. Van Oudheusden, and F. Scarano (2010). "Effect of interaction strength on unsteadiness in shock-wave-induced separations". *AIAA journal* 48.7, pp. 1480–1493.

Stroh, A., K. Schäfer, P. Forooghi, and B. Frohnapfel (2020). "Secondary flow and heat transfer in turbulent flow over streamwise ridges". *Int. J. Heat Fluid Flow* 81, p. 108518.

Sun, D., Q. Guo, C. Li, and P. Liu (2019). "Direct numerical simulation of effects of a micro-ramp on a hypersonic shock wave/boundary layer interaction". *Phys. Fluids* 31.12.

Tam, C. J., D. Eklund, R. Behdadnia, and T. Jackson (2005). "Investigation of boundary layer bleed for improving scramjet isolator performance". *AIAA/CIRA 13th International Space Planes and Hypersonics Systems and Technologies Conference*, p. 3286.

Thomas, F. O., C. M. Putnam, and H. C. Chu (1994). "On the mechanism of unsteady shock oscillation in shock wave/turbulent boundary layer interactions". *Exp. Fluids* 18.1, pp. 69–81.

Titchener, N. and H. Babinsky (May 2013). "Shock Wave/Boundary-Layer Interaction Control Using a Combination of Vortex Generators and Bleed". *AIAA J.* 51.5, pp. 1221–1233.

Touber, E. and N. D. Sandham (2009). "Large-eddy simulation of low-frequency unsteadiness in a turbulent shock-induced separation bubble". *Theor. Comput. Fluid Dyn.* 23.2, pp. 79–107.

Touber, E. and N. D. Sandham (2011). "Low-order stochastic modelling of low-frequency motions in reflected shock-wave/boundary-layer interactions". *J. Fluid Mech.* 671, pp. 417–465.

Uenalmis, O. and D. S. Dolling (1994). "Decay of wall pressure field and structure of a Mach 5 adiabatic turbulent boundary layer". *Fluid Dynamics Conference*, p. 2363.

Vadillo, J. L., R. K. Agarwal, and A. A. Hassan (2006). "Active control of shock/boundary layer interaction in transonic flow over airfoils". *Computational Fluid Dynamics 2004: Proceedings of the Third International Conference on Computational Fluid Dynamics, ICCFD3, Toronto, 12–16 July 2004*. Springer, pp. 361–366.

Vanderwel, C., A. Stroh, J. Kriegseis, B. Frohnapfel, and B. Ganapathisubramani (Mar. 10, 2019). "The instantaneous structure of secondary flows in turbulent boundary layers". *J. Fluid Mech.* 862, pp. 845–870.

Verma, S. B. and C. Manisankar (2019). "Control of compression-ramp-induced interaction with steady microjets". *AIAA J.* 57.7, pp. 2892–2904.

Verzicco, R. (2023). "Immersed boundary methods: Historical perspective and future outlook". *Annu. Rev. Fluid Mech.* 55.1, pp. 129–155.

Verzicco, R., M. D. de Tullio, and F. Viola (2025). *An Introduction to Immersed Boundary Methods*. Cambridge Monographs on Applied and Computational Mathematics. Cambridge University Press.

Vreman, B., B. Geurts, and H. Kuerten (1994). "Discretization error dominance over subgrid terms in large eddy simulation of compressible shear layers in 2D". *Commun. Numer. Methods Eng.* 10.10, pp. 785–790.

Wang, Z. and N. Cheng (2006). "Time-mean structure of secondary flows in open channel with longitudinal bedforms". *Adv. Water Resour.* 29.11, pp. 1634–1649.

Wangsawijaya, D. D., R. Baidya, D. Chung, I. Marusic, and N. Hutchins (July 10, 2020). "The effect of spanwise wavelength of surface heterogeneity on turbulent secondary flows". *J. Fluid Mech.* 894, A7.

Watts, J. (1968). "Flight experience with shock impingement and interference heating on the X-15-2 research airplane". *NASA TM X-1669* 1.

Webb, N., C. Clifford, and M. Samimy (2013). "Control of oblique shock wave/boundary layer interactions using plasma actuators". *Exp. Fluids* 54.6, p. 1545.

Welch, P. (1967). "The use of fast Fourier transform for the estimation of power spectra: A method based on time averaging over short, modified periodograms". *IEEE Transactions on Audio and Electroacoustics* 15.2, pp. 70–73.

Wen, B., S. Zhong, G. Wang, and L. Li (2024). "Effects of herringbone riblets on shock-wave/turbulent boundary-layer interactions". *Aerosp. Sci. Technol.* 146, p. 108914.

Wu, H., W. Huang, L. Yan, and Z. Du (2022). "Control mechanism of micro vortex generator and secondary recirculation jet combination in the shock wave/boundary layer interaction". en. *Acta Astron.* 200, pp. 56–76.

Wu, M. and M. P. Martin (2008). "Analysis of shock motion in shockwave and turbulent boundary layer interaction using direct numerical simulation data". *J. Fluid Mech.* 594, pp. 71–83.

Wu, W., L. Laguarda, S. Hickel, and D. Modesti (2025a). *Supplementary material to the publication 'Passive control of shock-wave/turbulent boundary-layer interaction via ridge-type roughness'*. Version 1. Animations available at https://doi.org/10.4121/857d1096-7901-4cb8-868b-3e73fadecf5f.

Wu, W., L. Laguarda, D. Modesti, and S. Hickel (June 1, 2025b). "Passive Control of Shock-Wave/Turbulent Boundary-Layer Interaction Using Spanwise Heterogeneous Roughness". *Flow Turbul. Combust.* 115, pp. 29–49.

Wu, W., L. Laguarda, D. Modesti, and S. Hickel (2026). "Passive control of shock-wave/turbulent boundary-layer interaction via ridge-type roughness". *J. Fluid Mech.* 1029, A51.

Wu, Y. and K. T. Christensen (2007). "Outer-layer similarity in the presence of a practical rough-wall topography". *Phys. Fluids* 19.8.

Xie, Z. and I. P. Castro (Oct. 2008). "Efficient Generation of Inflow Conditions for Large Eddy Simulation of Street-Scale Flows". *Flow Turbul. Combust.* 81.3, pp. 449–470.

Xu, F., S. Zhong, and S. Zhang (2018). "Vortical structures and development of laminar flow over convergent-divergent riblets". *Phys. Fluids* 30.5.

Ye, T., R. Mittal, H. S. Udaykumar, and W. Shyy (1999). "An accurate Cartesian grid method for viscous incompressible flows with complex immersed boundaries". *J. Comput. Phys.* 156.2, pp. 209–240.

Ye, Z., X. Xu, S. Yi, J. Liu, Z. Zhang, and R. Zeng (2025). "Influences of herringbone riblets on shock-wave/turbulent boundary layer interactions in supersonic compression-ramp flow". *Phys. Fluids* 37.8.

Yeager, C. and L. Janos (1985). *Yeager: An Autobiography*. Bantam Books. Bantam Books.

Zampiron, A., S. Cameron, and V. Nikora (Mar. 25, 2020). "Secondary currents and very-large-scale motions in open-channel flow over streamwise ridges". *J. Fluid Mech.* 887, A17.

Zhang, Q., Y. Liu, and S. Wang (2014). "The identification of coherent structures using proper orthogonal decomposition and dynamic mode decomposition". *J. Fluids Struct.* 49, pp. 53–72.

Zhdanov, O., T. O. Jelly, and A. Busse (Jan. 2024). "Influence of Ridge Spacing, Ridge Width, and Reynolds Number on Secondary Currents in Turbulent Channel Flow Over Triangular Ridges". *Flow Turbul. Combust.* 112.1, pp. 105–128.

Zhu, X. K., C. P. Yu, F. L. Tong, and X. L. Li (2017). "Numerical study on wall temperature effects on shock wave/turbulent boundary-layer interaction". *AIAA J.* 55.1, pp. 131–140.

ACKNOWLEDGEMENTS

"The water flows on thus, never ceasing" — so said Confucius, standing by a river. Almost five years have flowed forward without pause. Standing at this point in time and looking back at who I was, I once had countless imaginations about what might happen during the time as a PhD student. Now all of those possibilities have collapsed into the experiences I actually lived through. It may not have been the most ideal script, but it is the most precious experience that is uniquely mine. A PhD is a long journey, and the cycles of positive feedback are so infrequent. Without the people who accompanied me along the way, I do not think I could have persisted through this journey. So I want to record and express my gratitude to the wonderful people who have been with me.

The first people I want to thank are my two supervisors, Stefan and Davide. As my promoter, Stefan has been my guide in the field of CFD, and this goes back nine years to when I came to TUD as an undergraduate exchange student and took the CFD1 course. I am very grateful that, years later after completing my master's degree, we were able to continue working together in Delft. In our weekly Tuesday meetings, you could always quickly understand what I was presenting, and point out problems and solutions honestly and directly, explaining them in a way that was clear and easy for me to follow. You also cared deeply about my research progress and invested his time without reservation. One thing that has stayed with me is that not long after I started my PhD, INCA kept diverging on my test cases and my work was stalled. You sent an email at three in the morning saying you had just resolved the issue. Beyond research, You have also set an example for me in life, showing me what it truly means to love what you do. You tirelessly and enthusiastically keeps improving INCA, and even leave Easter eggs in it so that every simulation feels like embarking on a new space exploration.

I also want to thank my daily supervisor, Davide. In terms of research, you always gave me the most direct guidance and never minded the gaps in my foundational knowledge when I started my PhD — you would even carefully write out equations and formulas during our meetings, guiding me step by step. I am also grateful for your expertise in rough-wall flows, which ultimately led me to shift my research from porous media to rough-wall turbulence, and without that, the gradually clarifying topic of my dissertation would not have come about. Beyond research, Davide, you have been more like a friend — always responding promptly on WhatsApp and openly sharing your valuable experiences in academia. Over the past few years, I have encountered many discouraging moments, and completing this PhD has genuinely not been a simple thing. But both Stefan and Davide always gave me the most sincere encouragement and support. Your encouragement was never empty or formulaic, but rather honest sharing of your own understanding and reasoned thinking, accompanied by Stefan's warm, squinting smile and Davide's reserved and slightly shy one — after every meeting I came away with renewed confidence.

I also want to thank Luis. Because our research topics are closely related, you provided me with a great deal of help throughout the research process, and we had many

discussions about data processing and analysis. You are the person who, outside of my supervisors, helped me the most in my research. Special thanks also go to Colette, the secretary of our department — thank you for always being so responsive and helpful.

I also want to thank my lab colleagues, who have been so friendly and warm. The time spent with you in the lab has been full of good moments. Thank you, Xiaodong, for the countless instances of help and guidance you gave me at the beginning of my PhD — without your support, my first year would have been much harder. Haris, our shared supervisor team gave us a lot of common ground, and you have always offered your support without hesitation whenever I needed it. Thank you also for making a point to greet me every time you came into or left the office back when I was sitting in the most out-of-the-way corner, and for always inviting me to coffee breaks. Jane, you were the first colleague I met when I joined the lab. You are so kind and genuinely care about everyone, and thank you for letting me visit the supersonic wind tunnel in operation — that was incredibly cool. Tyler, you showed me that an American could have such a deep love for Chinese food and such a genuine interest in and affection for China. Thank you also for your hard work every year at Thanksgiving, which always gave us a truly wonderful meal. Renzhi, we are the closest pair in the office. You are the perfect travel companion — our trip to Belgrade in particular remains a fond memory, and your cooking skills in the spacious shared kitchen at your place are something I will always remember. Mengjie, you are the quietest person in the office but also the most dedicated, and your research has progressed the fastest. Every conversation with you has been a pleasure, and thank you for introducing me to many good friends from Civil Engineering. Yifu, the sense of humor that comes with being from Tianjin means that every outing and every conversation with you is filled with laughter. Kaisheng, I really love your vivid travel stories and your optimistic attitude of embracing experience above all else. Ata, we have been the best INCA teammates and conference partners — in the story of the daring rescue in Berlin, you will always be the true hero (wink). Kherlen, you are the most approachable person in the office. Your curiosity and your cultural background — similar to mine yet distinctly different — always give us plenty to talk about. Luuk, I really enjoy talking tennis with you; you are the person in the office who understands me best when it comes to the sport. But I have to say, you're missing out by not eating meat on the bone — there is so much great Chinese food you'll never get to experience! Thomas, talking with you is like having access to a walking encyclopedia, and I very much appreciate your slightly proud French manner — and I mean that as a compliment. Adrian, your consistently positive and optimistic attitude is something I will always aspire to. When we took an afternoon walk during the symposium in Lunteren and you said your dream was to go back to your hometown and run a farm, I saw something light up in your eyes. Max, you are also such a kind person — thank you for offering me your desk when I had to move out of HSL. Aneek, whenever we have lunch together, you always keep the conversation going and find interesting things to talk about. Andrea, thank you for introducing me to bouldering — it really is a great sport (second only to tennis). Suyash, thank you for being my nicest and longest-lasting neighbour at HSL. Sara, thank you for sharing photos of your cat — it is truly adorable. Thank you to Abdoo and Kevin for providing delicious hand-brewed coffee at lunch. As for the newer generation of INCAers, Joel and Edino — it is always a pleasure to talk with you. Though you are younger PhD candidates, you are both highly capable and thoughtful.

And thank you to all the other colleagues as well: Marco, Marina, Brian, Vinicius, Babak, Sajad, Parisa, Ali, Abbas, Antonios, Nikos, Péter, Zhen, Michele and those who had already graduated — Constantin, Edo, Beto, Alessandro, Christoph, Varun, Gabriel, Kushal, Giulia, Giulio, Mohamad, Jordi, Sven and others. Whether through discussions in the office, coffee breaks, lunches, conference trips, or simply sharing the ups and downs of research life, all of you helped create a warm and welcoming environment. Looking back, sharing this chapter of life with such an international and diverse group of people has been one of the most rewarding parts of my PhD journey.

Thank you also to friends from Wind Energy — Xiaoming, Jingna & Dong, Yanan, Sen, Guanqun & Adhyanth, Jiaxin, Clem, Haoyuan, Xin, Kaj, and others — as well as friends from C&O and ASM: Liming, Hang, Yifei, Yiyuan, Xiang, Wenjie, Xiaopeng, Zhiyuan, Lubin, Chi, and Nan. The time spent with you both inside and outside the faculty has been enriching.

There are also friends outside the faculty I would like to thank especially. First, to my fellow card-game crew: Shihao & Bing, Mengjie & Hang, Jianxin, Guofeng, and Lifei — the times we spent together eating hot pot and playing cards have been such fun. Thank you to the friends I have played tennis with: Cheng & Shiwen, Ya, Kun, Wen, Fenghuan, Qiaochu, Fengyan, Zhaojiang, Jingsen & Yuqing, Jinlun, and Xiaohan — the hours spent on the court and talking about tennis with you have been truly happy ones. And thank you to the other friends who have supported and encouraged me in daily life: Zichao, Kai, Xiaoxia, Yizhao, Ting, Tianqi, Mengyu, Ruipeng, Daiqi, Asif and many others. During my years in Delft, Ruipeng and Shenghao — we have run and sweated together on the tennis court in X, and together with Xinyue, Qianye, Yu, Zhuyu & Yuhe, we have travelled together, watched the French Open, and explored Chinese restaurants across Europe. You are my family in the Netherlands, and the time spent with you has been the happiest and most comforting. Special thanks also go to Renjing and Zhang — getting to know you through aviation photography in Schiphol was a wonderful coincidence, and thank you for sending me postcards from all over the world, bringing me glimpses of places far away. Thank you to Moyan & Shiqiang — from being desk neighbours in high school to doing our PhDs together in the Netherlands, that too is a special kind of fate. Thank you for inviting me to visit you in Amsterdam and for your warm hospitality every time.

Thank you also to friends back home in China. Weibo and Geng have shared in the setbacks of research with me. Thank you to Chenjing, Kun, Zihao & Tingting, Congrui, Xinyu and Xianchao for sharing the joys and frustrations of everyday life with each other. Thank you to Guangyao, Haidong, and Shikang for welcoming me back with the same warm and genuine hospitality as always every time I return to our hometown.

Last of all, I want to express my deepest gratitude to my parents, Xuexi and Yulan. In an ordinary small city in Shandong, you have worked on ordinary jobs, without grand ambitions — only the wish that your son would grow up healthy and happy, and become someone useful to society. To that end, you have given him unconditional love and support, day after day, for thirty years.

Wencan Wu
Delft, The Netherlands

CURRICULUM VITÆ

Wencan WU

28-04-1996 Born in Heze, Shandong Province, China.

EDUCATION

2021 – 2026 **PhD.**
Aerodynamics
Faculty of Aerospace Engineering
Delft University of Technology, Delft, the Netherlands
Thesis: Passive Control of Shock-Wave/Turbulent Boundary-Layer Interaction
Promotor: Prof. Dr. -Ing. habil S. Hickel
Co-promoter: Dr. D. Modesti

2018 – 2021 **M.Eng.**
Aeronautical Engineering
School of Energy and Power Engineering
Beihang University, Beijing, China

2017 – 2018 Exchange Programme
Aerodynamics
Faculty of Aerospace Engineering
Delft University of Technology, Delft, the Netherlands

2014 – 2018 **B.Eng.**
Flying Vehicle Power Engineering
School of Energy and Power Engineering
Beihang University, Beijing, China

SCIENTIFIC CONTRIBUTIONS

JOURNAL ARTICLES

3. **W. Wu**, D. Modesti and S. Hickel. Passive control of shock-wave/turbulent boundary-layer with convergent-divergent riblet. Submitted to *Int. J. Heat Fluid Flow*.

2. **W. Wu**, L. Laguarda, D. Modesti and S. Hickel. Passive control of shock-wave/turbulent boundary-layer interaction via ridge-type roughness. *J. Fluid Mech.*, (2026). doi: https://doi.org/10.1017/jfm.2026.11204

1. **W. Wu**, L. Laguarda, D. Modesti and S. Hickel. Passive control of shock-wave/turbulent boundary-layer interaction using spanwise heterogeneous roughness. *Flow Turbul. Combust.*, **115**, 29–49 (2025). doi: https://doi.org/10.1007/s10494-024-00580-0

CONFERENCE PROCEEDINGS

4. **W. Wu**, L. Laguarda, D. Modesti, S. Hickel. Reynolds number effects on shock-wave/turbulent boundary-layer interactions over ridge-type roughness. In 15^{th} *International ERCOFTAC Symposium on Engineering Turbulence Modelling and Measurements*, Dubrovnik, Croatia (2025).

3. **W. Wu**, L. Laguarda, D. Modesti, S. Hickel. Effects of ridge-type spanwise-heterogeneous roughness on shock-wave/turbulent boundary layer interactions. In 25^{th} *Shock Interaction Symposium*, Delft, the Netherlands (2024).

2. **W. Wu**, L. Laguarda, D. Modesti, S. Hickel. Effects of spanwise heterogeneous roughness on shock-wave/turbulent boundary layer interactions. In *ERCOFTAC Workshop Direct & Large Eddy Simulation 14*, Erlangen, Germany (2024).

1. **W. Wu**, L. Laguarda, D. Modesti, S. Hickel. Passive control of shock-wave/turbulent boundary layer interaction using spanwise heterogeneous roughness. In 57^{th} *3AF International Conference on Applied Aerodynamics*, Bordeaux, France (2023).

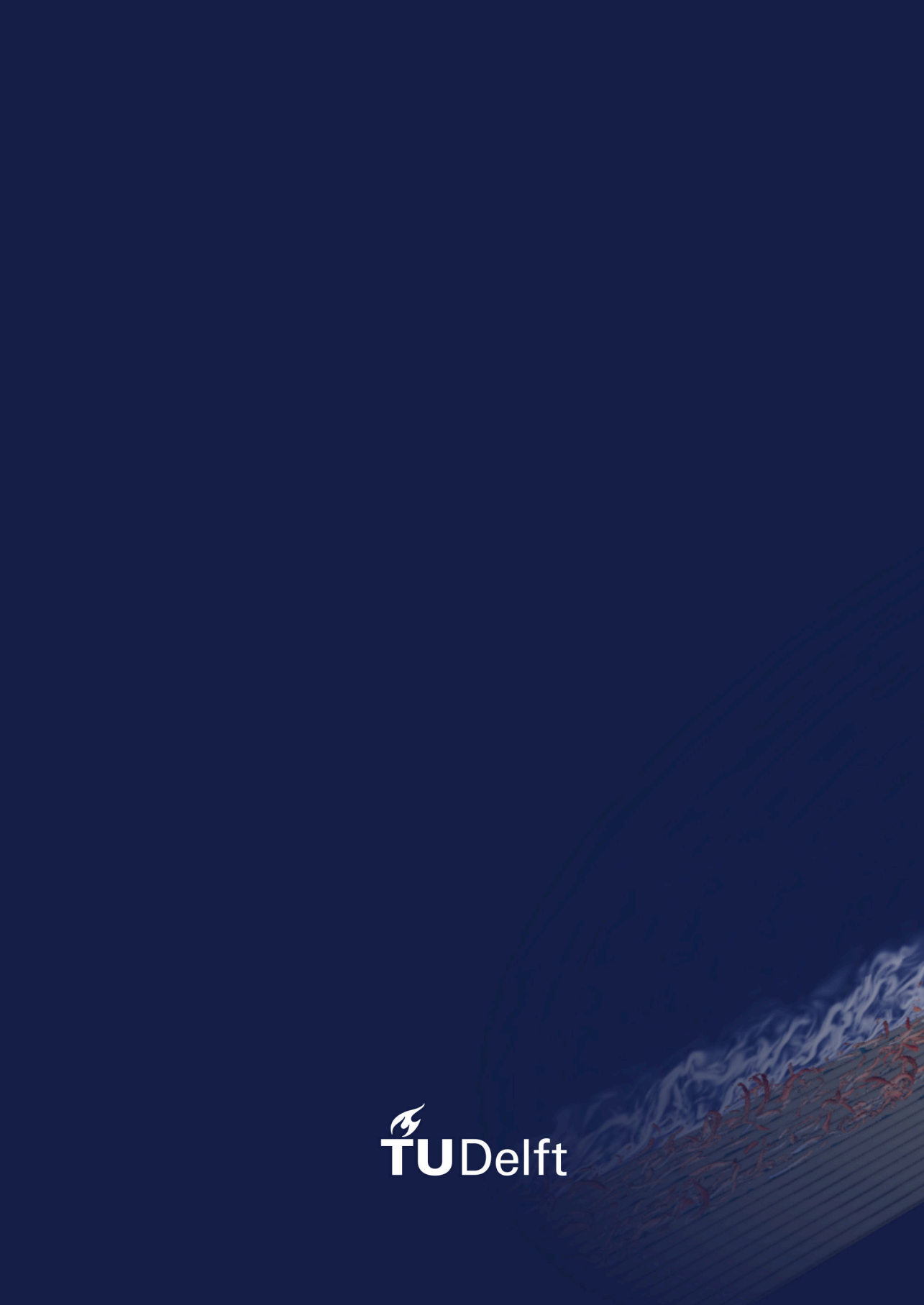
TU Delft